Department of Chemistry
Cumulative Examinations
December 6, 2013

You may choose to answer any exam from any area covered in the examination booklet. Each exam may contain multiple parts. You may answer more than one exam but each exam is scored separately and is treated as an individual examination result. Thus, answering parts of two exams with a score of 50% *would not* yield a 100% grade for this cumulative exam. Instead you would receive 50% on each examination attempted.

This booklet contains ***five*** examinations.

1) Analytical Cumulative Examination, Page 1
2) Biochemistry Cumulative Examination, Pages 2-13
3) Inorganic Cumulative Examination, Pages 14-15
4) Organic Cumulative Examination, Page 16
5) Physical Cumulative Examination, Pages 17-18

On your examination booklet:

1) Print your student ID number.
2) Print the Exam Booklet number.
3) Print the question number you are answering.
4) Print the Exam Date.

Do not write your name anywhere on the examination booklet. Each exam will be scored anonymously. If you attempt more than one exam, *you must use a separate examination booklet for each examination*.

When you complete the examination, return the examination and your answer booklet to the proctor. Exam results will be posted on bulletin board #2B on the north side of the hall near BRWN 2124.

PURDUE
UNIVERSITY

Analytical Chemistry Cumulative Exam, Dec. 7, 2013

[30pts]1.a. Define analytical precision.

b. The authors of the Dorn et al. (2013) paper evaluate the measurement precision for each method involved in this study by examining the distribution of measured [NO_3], for "zero" NO_3 samples. The precision is reported in each case as an absolute concentration value (e.g. 0.2 - 0.5 ppt, for the NOAA instrument). Discuss the extent to which you think this applies for all concentrations for measurements with NO_3 present. You can discuss the NOAA method and Figure 3, as an example.

c. Why might the NO_3 removal method be a better way to evaluate <u>accuracy</u> of the methods?

d. The paper discusses measurement issues that might lead to larger values of the precision than those reported for the cavity ringdown absorption spectroscopy (CRDS) methods. Discuss experimental reasons why the precision might not be a fixed absolute value for the CRDS methods, and why these reasons might/might not impact the "in-situ" absorption methods.

e. What component(s) of the measurement precision does their "zero" NO_3 method evaluate? Suggest a better way to express the measurement precision.

[10]2. Explain why λ=662nm is an optimum choice of analytical wavelength for the DOAS instrument.

[10]3. Was this intercomparison experiment able to evaluate the accuracy of the seven instruments? Explain how, or explain why not.

[10]4. Describe a laboratory experiment that could be done to improve the accuracy of all of the seven instruments involved in the intercomparison.

[10]5. What exactly is the statistical significance of the confidence interval listed in Table 2?

[10]6. Describe a way with an improved hardware component that would improve the <u>sensitivity</u> for all seven methods.

[10]7. The Brown et al. Appl. Phys. B (2002) paper describing their cavity ringdown instrument states in the Abstract "detection of the nitrate radical, NO_3, has been demonstrated with a sensitivity of 0.25 ppt (1σ)". Comment on whether you think that a reported value of 0.25ppt is an appropriate value for the sensitivity, and why.

[10]8. The reported precision values for the cavity ringdown spectrometers (CRDS) was on average much better than for the absorption spectroscopy-based methods. Describe a fundamental characteristic of the CRDS method that theoretically makes it a superior extinction-based method, in terms of precision.

Atmos. Meas. Tech., 6, 1111–1140, 2013
www.atmos-meas-tech.net/6/1111/2013/
doi:10.5194/amt-6-1111-2013
© Author(s) 2013. CC Attribution 3.0 License.

Atmospheric Measurement Techniques
Open Access

Intercomparison of NO_3 radical detection instruments in the atmosphere simulation chamber SAPHIR

H.-P. Dorn[1], R. L. Apodaca[2], S. M. Ball[3], T. Brauers[1], S. S. Brown[4], J. N. Crowley[5], W. P. Dubé[4], H. Fuchs[4,1], R. Häseler[1], U. Heitmann[6], R. L. Jones[7], A. Kiendler-Scharr[1], I. Labazan[5], J. M. Langridge[7,*], J. Meinen[8], T. F. Mentel[1], U. Platt[9], D. Pöhler[9], F. Rohrer[1], A. A. Ruth[6], E. Schlosser[1,**], G. Schuster[5], A. J. L. Shillings[7], W. R. Simpson[2], J. Thieser[9,***], R. Tillmann[1], R. Varma[6,****], D. S. Venables[10], and A. Wahner[1]

[1]Institute of Energy and Climate Research, IEK-8: Troposphere, Forschungszentrum Jülich, Julich, Germany
[2]Department of Chemistry and Biochemistry and Geophysical Institute, University of Alaska, Fairbanks, AK, USA
[3]Department of Chemistry, University of Leicester, Leicester, UK
[4]Barth System Research Laboratory, National Oceanic and Atmospheric Administration, Boulder, CO, USA
[5]Max Planck Institute for Chemistry, Mainz, Germany
[6]Physics Department & Environmental Research Institute, University College Cork, Cork, Ireland
[7]Department of Chemistry, University of Cambridge, Cambridge, UK
[8]Institute for Meteorology and Climate Research – Atmospheric Aerosol Research, Karlsruhe Institute of Technology, Karlsruhe, Germany
[9]Institute of Environmental Physics, University of Heidelberg, Heidelberg, Germany
[10]Chemistry Department and Environmental Research Institute, University College Cork, Cork, Ireland
*now at: Barth System Research Laboratory, NOAA, Boulder, CO, USA
**now at: Institute for Meteorology and Climate Research, IMK-AAF, Karlsruhe Institute of Technology, Karlsruhe, Germany
***now at: Max Planck Institute for Chemistry, Mainz, Germany
****now at: Physics Department, National Institute of Technology Calicut, Calicut, India

Correspondence to: H.-P. Dorn (h.p.dorn@fz-juelich.de)

Received: 5 December 2012 – Published in Atmos. Meas. Tech. Discuss.: 9 January 2013
Revised: 3 April 2013 – Accepted: 6 April 2013 – Published: 2 May 2013

Abstract. The detection of atmospheric NO_3 radicals is still challenging owing to its low mixing ratios (≈ 1 to 300 pptv) in the troposphere. While long-path differential optical absorption spectroscopy (DOAS) has been a well-established NO_3 detection approach for over 25 yr, newly sensitive techniques have been developed in the past decade. This publication outlines the results of the first comprehensive intercomparison of seven instruments developed for the spectroscopic detection of tropospheric NO_3. Four instruments were based on cavity ring-down spectroscopy (CRDS), two utilised open-path cavity-enhanced absorption spectroscopy (CEAS), and one applied "classical" long-path DOAS. The intercomparison campaign "NO3Comp" was held at the atmosphere simulation chamber SAPHIR in Jülich (Germany) in June 2007. Twelve experiments were performed in the well-mixed chamber for variable concentrations of NO_3, N_2O_5, NO_2, hydrocarbons, and water vapour, in the absence and in the presence of inorganic or organic aerosol. The overall precision of the cavity instruments varied between 0.5 and 5 pptv for integration times of 1 s to 5 min; that of the DOAS instrument was 9 pptv for an acquisition time of 1 min. The NO_3 data of all instruments correlated excellently with the NOAA-CRDS instrument, which was selected as the common reference because of its superb sensitivity, high time resolution, and most comprehensive data coverage. The median of the coefficient of determination (r^2) over all experiments of the campaign (60 correlations) is $r^2 = 0.981$ (quartile 1 (Q1): 0.949; quartile 3 (Q3): 0.994; min/max: 0.540/0.999). The linear regression analysis of the campaign data set yielded very small intercepts (median: 1.1 pptv; Q1/Q3: −1.1/2.6 pptv; min/max: −14.1/28.0 pptv), and the slopes of the regression lines were close to unity (median: 1.01; Q1/Q3: 0.92/1.10; min/max: 0.72/1.36). The deviation of individual regression slopes from unity was always within the combined accuracies of each instrument pair. The very good correspondence between the NO_3 measurements by all instruments for aerosol-free experiments indicates that the losses of NO_3 in the inlet of the instruments were determined reliably by the participants for the corresponding conditions. In the presence of inorganic or organic aerosol, however, differences in the measured NO_3 mixing ratios were detectable among the instruments. In individual experiments the discrepancies increased with time, pointing to additional NO_3 radical losses by aerosol deposited onto the filters or on the inlet walls of the instruments. Instruments using DOAS analyses showed no significant effect of aerosol on the detection of NO_3. No hint of a cross interference of NO_2 was found. The effect of non-Lambert–Beer behaviour of water vapour absorption lines on the accuracy of the NO_3 detection by broadband techniques was small and well controlled. The NO3Comp campaign demonstrated the high quality, reliability and robustness of performance of current state-of-the-art instrumentation for NO_3 detection.

Published by Copernicus Publications on behalf of the European Geosciences Union.

1 Introduction

Radical chemistry in the polluted nighttime troposphere is governed by the abundance of NO_3 radicals. They are very reactive and effectively oxidise alkenes, aldehydes, and biogenic volatile organic compounds (VOCs). Although their role as atmospheric oxidant during the day is negligible due to their fast photolytic decomposition, their importance in atmospheric nighttime chemistry is comparable to that of OH radicals during daytime. Fundamental reviews on the physics and chemistry of NO_3 radicals were published by Wayne et al. (1991) and recently by Brown and Stutz (2012).

The key reactions controlling the nighttime formation and destruction of oxidised nitrogen are summarised in the following. In the troposphere NO_3 radicals are formed through the reaction of nitrogen dioxide with ozone:

$$NO_2 + O_3 \rightarrow NO_3 + O_2. \quad (R1)$$

During daytime NO_3 radicals do not build up to relevant levels (< 1 pptv) because they efficiently absorb light in the visible region of the solar spectrum, leading to photolysis into a radical channel,

$$NO_3 + h\nu \rightarrow NO_2 + O, \quad (R2)$$

and a molecular channel,

$$NO_3 + h\nu \rightarrow NO + O_2. \quad (R3)$$

Based on these photolysis reactions the lifetime of NO_3 under typical daylight conditions is approximately 5 s. In addition NO_3 radicals react very rapidly with NO:

$$NO_3 + NO \rightarrow NO_2 + NO_2. \quad (R4)$$

This reaction is important during the day, when its rate often exceeds that of photolysis, and in cases of fresh emissions of NO. At night the NO reaction often limits the lifetime of NO_3 when no excess O_3 is present to convert NO into NO_2.

NO_3 itself reacts with NO_2 to form N_2O_5 (the anhydride of nitric acid, HNO_3):

$$NO_3 + NO_2 + M \rightleftharpoons N_2O_5 + M. \quad (R5)$$

N_2O_5 is thermally unstable and can decompose into its precursors, thereby establishing an equilibrium between NO_3 and N_2O_5. The back-reaction of (R5) is strongly temperature dependent, with N_2O_5 being dominant at low temperatures. Recently Osthoff et al. (2007) remeasured the equilibrium constant of Reaction (R5) to $K_{eq}(T) = (5.1 \pm 0.8) \times 10^{-27} \exp((10871 \pm 46)/T)\,\mathrm{cm^3\,molecule^{-1}}$. N_2O_5 can efficiently be hydrolysed to HNO_3 on the surface of aerosol particles:

$$N_2O_5 + H_2O(\mathrm{het}) \rightarrow 2HNO_3. \quad (R6)$$

The wet and dry deposition of the HNO_3 formed by hydrolysis of N_2O_5 is one of the most important loss reactions of oxidised nitrogen compounds in the atmosphere (Brown et al., 2006).

Owing to the high reactivity, the mixing ratio of NO_3 radicals in the troposphere is typically in the lower pptv range, and their spatial and temporal variability can be high. This places high demands on the selectivity, sensitivity, and time resolution of measurement techniques used for NO_3 detection. High-quality, accurate, and precise in situ measurements of NO_3 and N_2O_5 are a prerequisite to understand the chemical processes controlling the chemistry of nocturnal nitrogen oxides and the significance of these species for the oxidising capacity of the nighttime troposphere. In the late 1970s the detection of NO_3 radicals in the troposphere was pioneered by Platt and Perner (Platt and Perner, 1980; Platt et al., 1980). They used long-path differential optical absorption spectroscopy (DOAS), which has evolved into a standard technique for the detection of atmospheric NO_3. DOAS has been widely used in different configurations in field experiments (e.g. Platt et al., 1981; Allan et al., 2000; Geyer et al., 2001, 2003; Stutz et al., 2004; McLaren et al., 2004; Sommariva et al., 2007; Vrekoussis et al., 2004, 2007) and chamber studies (e.g. Wängberg et al., 1997; Bossmeyer et al., 2006).

In the 1980s the matrix isolation electron spin resonance (MI-ESR) technique was developed, enabling absolute, calibration-free detection of NO_3 radicals (Mihelcic et al., 1993). In a field intercomparison on NO_3 detection between DOAS and MI-ESR (Geyer et al., 1999), the latter worked very successfully. It, however, suffered from its inferior time resolution (sampling time ≥ 30 min) and substantial handling difficulties which only allowed a limited number of samples to be taken per day.

In the past 15 yr new spectroscopic instruments for sensitive tropospheric NO_3 detection have been developed. Their

detection principle either makes use of the specific fluorescence properties of the NO_3 molecule, as applied in laser-induced fluorescence (LIF) spectroscopy (Matsumoto et al., 2005; Wood et al., 2003), or takes advantage of its well-resolved strong visible absorption band arising from the $\tilde{B}^2E' \leftarrow \tilde{X}^2A_2'$ electronic transition on which the new cavity-enhanced absorption techniques are based (cf. Ball and Jones, 2003; Brown, 2003, and references therein). Since the first laboratory detection of NO_3 radicals by cavity ring-down spectroscopy (CRDS) by King et al. (2000), many cavity-based approaches have been developed (see, for instance, Ayers et al., 2005; Bitter et al., 2005; Brown et al., 2001, 2002a,b; Dubé et al., 2006; Fiedler et al., 2003, 2007; Simpson, 2003; Venables et al., 2006). Some of these instruments are also capable of measuring N_2O_5 concentrations indirectly by quantitative thermal conversion into NO_3 in a heated detection cell, and the N_2O_5 concentration is obtained after subtraction of the (generally much smaller) NO_3 concentration. In this way, simultaneous measurements of NO_3 and its equilibrium partner N_2O_5 in the troposphere became feasible for the first time (Chang et al., 2011).

This publication presents the results of an intercomparison of instruments for the detection of tropospheric NO_3 radicals that are all based on various absorption spectroscopic principles. The large atmosphere simulation chamber SAPHIR on the campus of Forschungszentrum Jülich was chosen for the "NO3Comp" campaign where the instruments were able to be operated concurrently under controlled atmosphere-like conditions. Chamber experiments are more appropriate for intercomparison exercises than field trials in the open atmosphere because natural spatial and temporal fluctuations of the air mass introduce additional variability and hence uncertainty to the measurement conditions, which in turn causes the comparison data to be less reliable. The chamber, however, allows for controlled production of NO_3 and N_2O_5 from Reactions (R1) and (R5), and provides the opportunity for multiple instruments to sample from the same well-mixed volume of gas.

Each of the participating instruments adhered to different calibration schemes of the radical transmission efficiency through filters and inlets and of the effective absorption path length in the cavity and was likely to exhibit different sensitivity to potential artefacts such as reactive trace gases or aerosol. Hence the instruments were exposed to various representative atmospheric scenarios during twelve measurement days in June 2007. This activity was the first comprehensive multi-instrument intercomparison of NO_3 detection instruments. Five instruments participating in NO3Comp were also capable of detecting N_2O_5, and four instruments detected NO_2 concurrently with NO_3. The results of the NO_2 and N_2O_5 measurements are reported in separate articles (Fuchs et al., 2010a, 2012). The ability of three broadband instruments to quantify the extinction coefficient of aerosols during the campaign is described by Varma et al. (2013). All experiments during NO3Comp were conducted as an open instrument intercomparison where discussions between the participants were generally allowed.

2 Instrumental

2.1 Absorption cross section of NO_3

In the following sections the experimental setups of the seven NO_3 detection instruments, as they were used at the SAPHIR chamber, are described in detail. A summary of their main properties is presented in the supplement to this publication.

Since all instruments made use of absorption spectroscopy the participants of NO3Comp agreed before the campaign to apply the absorption cross section published by Yokelson et al. (1994) for the retrieval of the NO_3 mixing ratio. Yokelson et al. measured the temperature dependence of the NO_3 absorption cross section between 440 and 720 nm within the temperature range 200–298 K in laboratory experiments. The NO_3 peak absorption cross section at 662 nm was reported to be $(2.23 \pm 0.22) \times 10^{-17}\,\mathrm{cm^2}$ at 298 K (2σ error limits). With decreasing temperature this value was found to increase by 36 % at 200 K. Orphal et al. (2003) re-measured the visible NO_3 spectrum using high-resolution Fourier transform spectroscopy ($\Delta\lambda = 0.026$ nm) and derived a parametrisation of the temperature dependence (200–330 K) of the peak cross section, which has been accepted into the current NASA/JPL recommendations (Sander et al., 2011). Excellent agreement exists between the Orphal model and the empirical relationships from Yokelson et al. (1994) and Osthoff et al. (2007). All groups participating in NO3Comp used this parameterisation to calculate the respective NO_3 cross section valid for the specific temperature of their NO_3 detection channel.

2.1.1 Pulsed cavity ring-down spectrometer, NOAA-CRDS

The most mature cavity-enhanced instrument employed in this campaign was the NOAA (Boulder, CO, USA) pulsed cavity ring-down spectrometer measuring NO_2, NO_3, and N_2O_5 simultaneously in separate channels. At the time of the intercomparison, this instrument and its predecessors (Brown et al., 2001, 2002a,b) had already been deployed in a number of atmospheric field measurement campaigns on the ground (Brown et al., 2003, 2007), aboard an aircraft (Brown et al., 2005) and aboard ships (Brown et al., 2004, 2005; Aldener et al., 2006).

The setup and performance of this instrument has been described in detail in the publication by Dubé et al. (2006). Inlet transmission and conversion efficiencies have been thoroughly studied by Fuchs et al. (2008). The NOAA-CRDS instrument consisted of 4 optical cavities used for the detection of NO_3 and N_2O_5 at 662 nm, and two cavities (at 532 nm) were taken for calibration purposes and measurement of NO_2 (Fuchs et al., 2010a). The temperature in the NO_3 detection channel was actively controlled to match the outside

temperature. A pulsed Nd:YAG-pumped dye laser (repetition rate 50 Hz) provided light at 662 nm (FWHM ≤ 1.5 pm) to detect NO_3. In addition, about 5 % of the light from the pump laser at 532 nm was used for the detection of NO_2 (Fuchs et al., 2012). The 662 nm cavity mirrors were separated by 0.91 m and had a reflectivity of 99.999 %. The light transmitted through the end mirror of the cavities was detected by photomultiplier tubes. The mixing ratio of the NO_3 radicals was calculated from the difference between the ring-down times with (τ) and without (τ_0) NO_3 in the cavity and the NO_3 absorption cross section (σ_{NO_3}):

$$[NO_3] = \frac{R_L}{c\sigma_{NO_3}} \left(\frac{1}{\tau} - \frac{1}{\tau_0}\right), \quad (1)$$

where c is the speed of the light and R_L is the ratio of the physical cavity length to the length over which the absorber is present in the cavity. The latter was reduced because the volumes adjacent to the mirrors were purged with zero air in order to avoid contamination of the mirror surfaces. The value of R_L had been determined previously in laboratory experiments to be 1.15 ± 0.03 (Fuchs et al., 2008). The zero ring-down time (τ_0) of the NO_3 cavity was measured every 3 to 5 min by adding 40 mL of a mixture of 100 ppmv NO in nitrogen to the cavity for 5 s. This yielded an NO mixing ratio of 0,5 ppmv in the sampled air, which was enough to quantitatively titrate NO_3 via Reaction (R4) before the gas entered the detection cavity. This method of determining the baseline signal allows for the selective separation of the NO_3 signal from the contributions of other atmospheric absorbers such as NO_2, O_3, and H_2O, and it is superior to, e.g., flushing the cavity with zero air because it leaves the O_3 and water absorptions unchanged.

During NO3Comp air was sampled from the chamber at a flow rate of 8 slm (standard litre per minute) through a Teflon FEP line (i.d. 4 mm, total length about 0.4 m) extending about 0.2 m into the chamber. In order to minimise wall losses in the system, the instrument operated at reduced pressure (∼ 350 hPa). A Teflon filter (25 µm thickness, 47 mm diameter, 2 µm pore size) was placed downstream of the inlet to remove aerosol particles which scatter light efficiently and would therefore constitute a large interference to a gas phase optical extinction measurement. Automated, regular filter changes (0.5–3 h) ensured constant NO_3 loss on the filter, which was well characterised when clean (Dubé et al., 2006; Fuchs et al., 2008).

The dye laser (tuning uncertainty ±0.02 nm) was fine tuned to a point on the broad maximum of the NO_3 absorption spectrum (≈ 661.94 nm) that is not resonant with any of the discrete water vapour absorption transitions in this region. The laser wavelength was not actively controlled but checked regularly by scanning across the water absorption lines around the NO_3 absorption peak.

Ring-down times of all channels were determined every second from the sum of 50 ring-down transients. Mixing ratios were corrected for possible changes in the $NO_2/NO_3/N_2O_5$ equilibrium (R5) due to temperature differences between the chamber and the ring-down detection cells. A model simulated the changes assuming a linear temperature profile between the measured SAPHIR temperature and the constant temperature in the cavity. The correction was typically < 0.5 %, with maximal differences during the campaign of ca. 5 % at high NO_2 mixing ratios. Extinction corrections (typically < 2 %) were made for varying Rayleigh scattering losses as well as for NO_2 and O_3 absorption (at 662 nm).

The accuracy of cavity ring-down data was dominated by the uncertainty of the absorption cross section (±5 %, 1σ), the error of the effective cavity length (±3 %), and the NO_3 transmission efficiencies of the cavity and the inlet/filter assembly. Calibrations based on standard additions to the inlet were unreliable and were made infrequently during the campaign due to a contamination in the N_2O_5 source used to generate NO_3. Therefore, laboratory measurements of the NO_3 transmission reported by Fuchs et al. (2008) of 92 ± 3 % were used for evaluation of all data during the campaign. An additional 10 % error was estimated in order to account for a possible systematic uncertainty of the NO_3 transmission during the campaign. The overall accuracy for NO3Comp was therefore +17 %/−5 %. The precision was determined from repeated measurements of τ_0 in zero air at 1 s data acquisition (Dubé et al., 2006). Under field measurement conditions values between 0.2 pptv and 0.5 pptv were obtained.

2.1.2 Off-axis cavity ring-down spectrometer, UAF-CRDS

A prototype diode-laser-pumped cavity ring-down instrument using off-axis excitation of the cavity (Paul et al., 2001; Kasyutich et al., 2002) was used by the group of the University of Alaska, Fairbanks (USA). The setup was mainly based on the same technical principles as described by Ayers et al. (2005). The emission intensity of a temperature-stabilised diode laser (662 nm) was square-wave modulated (100 % modulation depth) at a rate of 500 Hz and directed into an optical cavity consisting of two highly reflective mirrors (> 99.995 % at 662 nm) that were separated by 0.66 m. A purge flow (0.2 slm) of synthetic air protected the mirrors. Light transmitted through the second mirror was collected by an off-axis parabolic mirror and directed into a photomultiplier tube whose signal was digitised at a rate of $5\,\mathrm{MS\,s^{-1}}$ by a 12-bit ADC. Air was sampled from the chamber at 8 slm through a Teflon inlet line (length 0.4 m, i.d. 6.3 mm). To remove particulate matter the sample gas flowed through a Teflon filter (Pall Teflo, 2 µm pore size) which was changed daily at the beginning of each experiment. The residence time of the sample gas in the measurement cell was 2 s. The cell consisted entirely of PFA teflon tubing (i.d. 16 mm).

During NO3Comp it was noticed that the laser occasionally oscillated on two longitudinal modes, leading to multi-exponential ring-down decay. These events were diagnosed

and the corresponding data was excluded from the analysis. All data were corrected for the effective length of the cavity. The transmission efficiency of NO_3 was determined for each filter several times a day from measurements at different sample flow rates (i.e. for different residence times). An initial transmission of 76 % was found and a typical decay rate of −0.4 %h^{-1} was inferred from the plot of transmission versus filter use time. Both values were applied for all measurements during NO3Comp. Possible re-equilibration between NO_3 and N_2O_5 due to different temperatures between the SAPHIR chamber air and gas sample inside the detection cell was analysed using a simple equilibrium model. At low NO_2 mixing ratios (< 20 ppbv) the correction factor was small and reached maximal values around 13 % per degree of temperature difference (ΔT was always < 2 K) at high NO_2 mixing ratios. The zero ring-down time, τ_0, was determined regularly by addition of nitric oxide to the sample air, resulting in an NO mixing ratio of 50 ppbv in the measurement cell. The NO also reacts with O_3-forming NO_2. At 662 nm the NO_2 absorption is 1.39 times stronger than that of O_3, resulting in an offset of a few pptv NO_3 equivalent at 100 ppbv O_3. Moreover it was noted that the NO titrant cylinder used for the UAF instrument was contaminated with traces of NO_2, so adding NO also resulted in addition of some NO_2 (< 1 pptv NO_3 equivalent). The NO_3 mixing ratios were corrected for both interfering processes.

The instrument as operated during NO3Comp had a noise-equivalent 1σ detection limit of 0.5 pptv in 1 s. The total accuracy of the UAF-CRDS instrument was 20 % (1σ) taking into account an uncertainty of 17 % in the transmission efficiency of the inlet and measurement cell, 5 % uncertainty in the peak cross section for NO_3, and 10 % uncertainty of the effective cavity length.

2.1.3 Cavity ring-down spectrometer, MPI-CRDS

During the intercomparison campaign the cavity ring-down instrument from the Max Planck Institute for Chemistry (Mainz, Germany) was employed for the first time outside the laboratory. The instrument could be operated either in cavity ring-down (CRDS) or in cavity-enhanced absorption mode (CEAS) (Schuster et al., 2009). Although the CEAS mode had lower noise levels (~0.2 pptv in 1 s), baseline drifts limited the accuracy of this device, and all data reported here were measured exclusively based on the CRDS principle. The emission of a pulsed laser diode close to 662 nm (100 % square-wave power modulated at 200 Hz) entered the cavity off-axis (mirror reflectivity ≈ 99.998 %). The light exiting the cavity was detected by a photomultiplier (PMT) through a 590 nm cut-off filter and a 662 nm interference filter. The photomultiplier signal was digitised with a 100 MHz, 9-bit oscilloscope and averaged resulting in a time resolution of 5 s. The mirror distance was 0.7 m; sheath flows of filtered zero air (0.15 slm) protected the mirrors. The cavity enclosure was made from Pyrex glass (i.d. 15 mm), coated with a film of Teflon (DuPont FEP 121a).

Typical ring-down times were measured to be 86–100 µs. τ_0 was recorded by adding NO upstream of the Teflon filter, and complete titration of NO_3 was established within 0.1 s. Usually one minute of NO_3 measurement was followed by one minute of background measurement. The effect of adding NO to air samples containing O_3 on the total absorption at 662 nm was taken into account in the final analysis. Air was sampled from the SAPHIR chamber at a flow rate of 8 slm through a 0.68 m-long PFA tubing (9.5 mm i.d.), protruding 0.39 m into the chamber. A 22 mm-diameter Teflon membrane filter (pore size 2 µm) eliminated particles from the air stream. The average residence time within the optical cavity was ≈ 1 s.

Random fluctuations in the ring-down times resulted in an NO_3 precision (1σ detection limit) of 3 pptv for a 10 s acquisition time. The accuracy of the measurement was governed by systematic errors in the absorption cross section of NO_3, errors in the inlet gas transmission, correction for filter loss, and effective absorption path length. The NO_3 inlet losses were measured during four experiments at times of constant NO_3 in the chamber by variation of the flow rate through the instrument. An averaged correction factor of 1.13 ± 0.1 was determined. Filter losses were measured later in the lab, resulting in a correction factor of 1.18 ± 0.1. Both factors were taken constant for the campaign and were applied to correct the measured mixing ratios. The overall 1σ accuracy of the NO_3 measurement by MPI-CRDS of 14 % is given by the uncertainties of the determination of filter loss (8.5 %), inlet/cavity loss (8.9 %), cavity length (2.9 %), and absorption cross section (5 %).

2.1.4 Broadband cavity ring-down spectrometer, ULEIC-BBCRDS

The operating principles of the broadband cavity ring-down spectrometer of the University of Leicester (UK) have been discussed in Ball and Jones (2003, 2009), and an example of applying this instrument to measure ambient NO_3 during the NAMBLEX field campaign has been described by Bitter et al. (2005). The instrument's dye laser and CCD camera detector were upgraded following the NAMBLEX campaign; further details of the new hardware deployed for the SAPHIR intercomparison are given by Shillings et al. (2011).

A free-running dye laser, pumped by a Q-switched Nd:YAG laser at 20 Hz repetition rate, was employed as the broadband light source. A mixture of DCM and LDS698 dyes dissolved in methanol/DMSO was used to obtain laser emission with an approximately Gaussian spectrum (16 nm FWHM centred at 662 nm). The ring-down cavity was mounted 0.3 m below the SAPHIR chamber, supported from the same optical table as the laser. The cavity mirrors (diameter 20 mm, separation 1.83 m, peak reflectivity 99.996 % at 680 nm) were held in adjustable bellows mounts attached to

a thermally insulated Teflon tube (i.d. 19 mm) that formed the main body of the cavity. To reduce contamination of the mirror surfaces, the mirrors were purged with 0.5 slm of dry synthetic air. Hence the absorption measured over the full cavity length was multiplied by an experimentally determined length factor of $R_L = 1.05$ to correct for the gas sample being excluded from regions immediately in front of the mirrors. Air was drawn from the SAPHIR chamber through four parallel Teflon tubes (i.d. 3 mm, length 0.4 m, tubes protected from sunlight outside the chamber); the tubes projected 15 cm above the chamber's floor to sample gas uncompromised by wall effects. The sample flow rate of 10.1 slm corresponded to a mean residence time of 2.7 s inside the cavity. Light exiting the ring-down cavity was collected by a lens and focused into a 200 µm-diameter optical fibre attached to an imaging Czerny–Turner type spectrograph ($f = 250$ mm, $f/4$ optics, spectral resolution 0.36 nm FWHM). Time resolved spectra of light exiting the cavity were measured using a clocked CCD camera with an image sector of 512 pixels along the frame transfer axis (i.e. time) and 512 pixels along the wavelength dispersed axis (spectral coverage 645–683 nm, although in practice only the central 652–673 nm contributed usefully to the BBCRDS spectra recorded here). A slit mask bonded to the CCD chip resulted in the cavity output illuminating only 5 pixel rows on the frame transfer axis. Thus the CCD's clocking rate of 0.65 µs per pixel produced a minimum time resolution of 3.3 µs.

Owing to its broadband detection approach, BBCRDS is sensitive to all molecules that contribute structured features to the measured absorption spectrum (Ball and Jones, 2003, 2009). The absolute concentrations of the relevant absorbers, n_i, (NO_3, NO_2, and H_2O) were obtained by fitting the measured absorption spectrum, $\alpha(\lambda)$, with a linear combination of reference cross sections of the trace gases, $\sigma_i(\lambda)$, convoluted with the spectral response function of the BBCRDS instrument. The sample's absorption spectrum was calculated from wavelength-resolved ring-down times measured when the cavity contained the sample, $\tau(\lambda)$, and when the cavity was purged with dry synthetic air, $\tau_0(\lambda)$:

$$\alpha(\lambda) = \alpha_{bb}(\lambda) + \sum_i \sigma_i(\lambda) \cdot n_i = \frac{R_L}{c} \cdot \left[\frac{1}{\tau(\lambda)} - \frac{1}{\tau_0(\lambda)}\right]. \quad (2)$$

Because air drawn from the chamber was not filtered for aerosol, the broadband absorption background due to aerosol scattering, $\alpha_{bb}(\lambda)$, was accounted for by a polynomial function of second or third degree. Ozone has a weak, but detectable, broadly structured absorption at the wavelengths employed here; ozone was not included in the spectral fitting routine; instead its absorption was subtracted from the fitted $\alpha_{bb}(\lambda)$ background using ozone concentrations measured by SAPHIR's core instruments.

Water vapour is the largest contributor to the differential structure in atmospheric spectra around 662 nm, with line widths substantially narrower than the spectral resolution of the BBCRDS instrument, leading to non-Lambert–Beer absorption behaviour. Slight errors in fitting the water absorption features have been shown to mask the NO_3 absorption features and lead to spurious NO_3 retrievals. The approach to quantitatively evaluate the water vapour concentrations from the measured multi-exponential decay of the cavity output has been described by Ball and Jones (2003, 2009), Bitter et al. (2005), Langridge et al. (2008), and Shillings et al. (2011), and these methods were again applied to the present data set.

BBCRDS spectra were analysed assuming that the gas temperature inside the thermally insulated cavity was the same as inside SAPHIR. Consequently no corrections were made to the submitted data for NO_3/N_2O_5 re-equilibration (R5). In fact, temperature measurements taken infrequently during the campaign showed the gas inside the cavity to be marginally cooler than inside SAPHIR. Box modelling performed post-campaign indicated that the mean NO_3 mixing ratio inside the cavity was 95.8 % of that in the SAPHIR chamber itself, assuming a representative 1.5 K temperature drop on entering the cavity and a 2.7 s residence time. Thus the BBCRDS data are subject to a small, systematic undermeasurement of the NO_3 mixing ratio by typically around 4 % due to NO_3 re-partitioning to N_2O_5. The model showed the worst under-measurement to be 9 % when gas inside SAPHIR was at its warmest.

A small amount of ambient air (< 6 % of the total flow) was found to be leaking into the BBCRDS cavity during the campaign. The leak rate into the cavity was quantified for each experiment by comparing the measured water vapour mixing ratio in the cavity with data from a dew point hygrometer in the SAPHIR chamber. NO_3 mixing ratios reported were corrected for the dilution caused by this leak, and an overall uncertainty of 5 % for this effect was estimated. The leak was assumed not to contribute any additional chemical loss of NO_3. The NO_3 loss rate on the walls and inlet of the instrument was measured during the campaign by varying the flow rate (i.e. residence time) of the sample through the BBCRDS system. For the standard flow conditions (10.1 slm), the loss rate was $k_w = 0.045\ s^{-1}$ corresponding to a NO_3 transmission efficiency of 0.75, and this value was applied to correct the whole BBCRDS NO_3 data set. Whilst the uncertainty on this one measurement of k_w was relatively small (±3 %), it is likely that the NO_3 transmission losses varied somewhat throughout the campaign. In line with other instruments, conservatively, a ±10 % error was assigned on the 0.75 efficiency used to correct for the instrument's inlet/wall losses.

The overall accuracy of the BBCRDS NO_3 measurements is +15 %/−12 %, inferred from adding the individual sources of measurement error (length factor ±5 %; NO_3/N_2O_5 re-equilibration 0 to −9 %; air leak ±5 %; NO_3 wall loss ±10 %). The BBCRDS accuracy becomes +16 %/−13 %, including the 5 % uncertainty in the NO_3 absorption cross section. The precision of the retrieval of the NO_3 mixing ratio

(and other absorbers) was determined from the error of a linear fit to the absorber's absorption coefficients as a function of the corresponding absorption cross section. This method has been shown to produce robust estimates of the measurement precision and detection limits in other broadband cavity systems, e.g. Langridge et al. (2008). The precision for the present NO_3 data set was typically 2 pptv (1σ) for the 61 s averaging time.

2.1.5 Incoherent-broadband cavity-enhanced absorption spectrometer, UCC-IBBCEAS

The IBB-CEAS instrument of University College Cork (Cork, Ireland) is a broadband multi-component absorption technique using an optical cavity to measure the total extinction of an air sample (Fiedler et al., 2003). Instead of observing the temporal decay of the light intensity inside the cavity as in CRDS, the steady state intensity, I, of light leaking out of the cavity is measured and spectrally resolved. Setup and characteristics of the UCC-IBBCEAS instrument used during the campaign and details of the data evaluation procedure have been published by Varma et al. (2009). The underlying theory of cavity-enhanced absorption spectroscopy has been described in Fiedler et al. (2003, 2005, 2007); Venables et al. (2006); Gherman et al. (2008); and Triki et al. (2008).

The instrument consisted of a transmitter unit and a receiver unit, each housing one of the cavity mirrors (radius of curvature 21 m, diameter 4 cm, nominal reflectivity 99.87 % at 660 nm). The units were installed at the north and south ends of the SAPHIR chamber, resulting in a geometrical mirror distance of the open-path CEAS cavity of 20.13 ± 0.05 m. Considering the length of the cavity the setup was very stable. The cavity mirrors needed only marginal realignment during the campaign. The transmitter unit housed a 300 W "hot-spot" Xe lamp. The light was imaged onto an iris using two off-axis parabolic mirrors. Between the mirrors the wavelength range was selected with a dielectric band-pass filter (610–720 nm). Because the light spot tended to wander on the cathode, a fraction of the light was focused onto a quadrant detector which triggered a feedback loop to correct for changes in spot position. A telescope imaged the iris aperture approximately into the centre of the open-path cavity. Light transmitted by the cavity was further filtered in the receiver unit with a long-pass cut-off filter (630 nm, Schott RG630) and a 700 nm short-pass interference filter to ensure that light outside the mirror reflectivity range was eliminated. The light was focused into a fibre bundle (1 mm diameter) and connected to the 100 µm entrance slit of a spectrometer ($f = 0.33$ m, spectral resolution 0.6 nm). A spectral interval from 620 to 720 nm was detected by a CCD detector, and an acquisition time of 5 s was used for all NO_3 measurements.

The transmitter and receiver units were each equipped with a 1 m stainless steel pipe (diameter 57 mm) pointing from the cavity mirrors along the optical axis of the cavity. A seal was made between the pipes and the adjustable mirror mounts of the cavity mirrors using flexible Teflon foil in each unit. The pipes served three purposes: firstly, they allowed the mirrors to be purged with pure nitrogen with a flow rate of 10 slm which caused the effective cavity length to be $L_{eff} = 18.27 \pm 0.20$ m. Secondly, on the receiver side of the setup the pipe reduced stray light entering the detection system. Thirdly, the pipes were necessary to install the instrument to the outside of the SAPHIR chamber and to make a seal with its teflon wall.

The total extinction, $\alpha(\lambda)$, of the air sample is calculated by

$$\alpha(\lambda) = \frac{1 - R(\lambda)}{L_{eff}} \left(\frac{I_0(\lambda)}{I(\lambda)} - 1\right), \quad (3)$$

where $I_0(\lambda)$ and $I(\lambda)$ are the intensities transmitted by the cavity in zero air and with a sample gas, respectively, $R(\lambda)$ is the average mirror reflectivity, and L_{eff} is the effective cavity length (Fiedler et al., 2003). The UCC-IBBCEAS instrument used an open cavity; hence, the background intensity, $I_0(\lambda)$, in zero air could only be determined once a day in the morning after the chamber was flushed over night and before trace gases were introduced into the chamber.

To provide absolute absorption measurements using the IBB-CEAS principle, the reflectivity of the cavity mirrors, $R(\lambda)$, has to be known across the bandwidth of the measurement. During NO3Comp, $R(\lambda)$ was measured daily by moving an antireflection-coated window of well-known loss into the cavity in zero air (Varma et al., 2009). The total loss (reflection plus transmission) of the window was determined in the lab with a pulsed cavity ring-down instrument as a function of wavelength, ranging from 0.55 % around 630 nm to 0.3 % at 690 nm. An average reflectivity function, $R_{avg}(\lambda)$, peaking at $R_{avg}(620\ nm) = 0.9987 \pm 1.5 \times 10^{-4}$ was calculated from all individual measurements during NO3Comp and applied for the retrieval of the NO_3 mixing ratios.

A singular value decomposition algorithm was used for the retrieval of the absorber mixing ratios from a linear combination of the reference spectra (convoluted for 0.6 nm spectral resolution), and a second-order polynomial represented broadband spectral structures, $\alpha_{bb}(\lambda) = n_0 + n_1\lambda + n_2\lambda^2$, resulting mainly from aerosol extinction:

$$\alpha(\lambda) = \alpha_{bb}(\lambda) + \sum_i \sigma_i(\lambda) \cdot \int_0^{L_{eff}} n_i(x)\,dx$$
$$= \frac{1}{L_{eff}} \left[\frac{I_0(\lambda)}{I(\lambda)} - 1\right](1 - R(\lambda)). \quad (4)$$

The fitting algorithm did not include O_3 because its absorption spectrum in the region of interest (655–670 nm) is weak and free of spectral fine structures; hence the broadband O_3 absorption was accounted for by the polynomial. To properly describe the complex absorption spectrum of water vapour, a concentration-corrected absorption cross section, $\sigma'_{H_2O}(\lambda)$,

was calculated for each water concentration that occurred in experiments as described by Varma et al. (2009).

The overall accuracy of UCC-IBBCEAS was estimated to be ±16 %. This estimate took into account the standard deviation of the reflectivity measurements, the uncertainty of the NO_3 cross section and the effective cavity length, the fluctuations of I_0 and a 10 % uncertainty of various analysis approaches (choice of fit range and weighting). The measurement precision was given as percentage error of the NO_3 mixing ratio determined from the 1σ standard deviation of the fit residuals. The 1σ detection limit is estimated to be 1 pptv for a 5 s averaging time.

2.1.6 Cavity-enhanced DOAS, UHD-CEDOAS

The University of Heidelberg (Germany) CEAS-based DOAS instrument used a short open-path setup and was installed inside the SAPHIR chamber mounted on a steel frame 60 cm above the floor in front of the fan. Except for the cavity mirrors all parts of the instrument were enclosed with Teflon foil to avoid surface reactions or out-gasing close to the optical absorption path. The optical setup and the specifics of the data evaluation of CEDOAS measurements are described in the publications by Meinen et al. (2010) and Platt et al. (2009), respectively.

The cavity consisted of two highly reflective mirrors (25.4 mm diameter and 1 m radius of curvature) with a nominal peak reflectivity of 99.9985 % at 655 nm. The separation of the mirrors was 0.62 m, and the effective optical path length was reduced to 0.5 ± 0.01 m by a purge flow of 5 slm of synthetic air. An LED (peak wavelength 665 nm, FWHM 23 nm), housed in a temperature-stabilised box (300 ± 2 K), was mounted to one of the mirrors, and the light was guided into the cavity by a 40 mm plano convex lens and a 610 nm long-pass filter (Schott RG610). Light leaking through the exit mirror was focused into a 400 µm quartz fibre (NA = 0.22, 5 m length). The fibre was attached alternatively to a photomultiplier tube (PMT) or to a temperature-stabilised mini-spectrograph (273 ± 0.1 K, $f = 42$ mm, spectral resolution 1.06 nm), both placed outside the chamber, for time-resolved (CRD) or wavelength-dispersed measurements (CEAS), respectively. Typical signal averaging times were 300 s.

Data evaluation was based on the classical DOAS approach (Platt and Stutz, 2008). In DOAS applications the length of the absorption light path is well known and constant. In combination with an optical cavity (CEDOAS), however, the effective path length that photons travel in the optical cavity, X_{eff}, can be highly variable because X_{eff} depends not only on the wavelength-dependent reflectivity finesse of the cavity, $F = \pi\sqrt{R(\lambda)}/(1 - R(\lambda))$ (Triki et al., 2008), but also on broadband losses by Mie and Rayleigh scattering, as well as on the mixing ratios of all absorbing constituents contributing to the total extinction in the cavity (cf. Platt et al., 2009).

The effective mirror reflectivity, $R_{eff}(\lambda)$, was determined daily from measurements of the cavity ring-down decay in pure synthetic air, using the LED in pulsed mode. The multi-exponential time-dependent decay of the cavity intensity was modelled after Meinen et al. (2010, Eq. 4b) using the cavity transmission spectrum measured in CEAS mode (which reflects the LED emission spectrum folded by the unknown "true" mirror reflectivity function) and the wavelength-dependent mirror reflectivity, $R_M(\lambda)$, provided by the mirror manufacturer. A single scaling factor, a, and an offset, b, were fitted to the modelled decay function in order to reproduce the measured time decay. The effective ("true") mirror reflectivity, R_{eff}, was obtained by $R_{eff}(\lambda) = a \times R_M(\lambda) + b$ assuming the shape of the mirror reflectivity $R_M(\lambda)$ to be invariant. The effective path length in the cavity at the NO_3 absorption maximum in zero air, required for the DOAS evaluation process, was calculated according to (L = mirror separation)

$$X_0(662\ nm) = \frac{L}{1 - R_{eff}(662\ nm)}. \quad (5)$$

Typical values during NO3Comp were 8400 m ± 100 m (9…18 June) and 8700 m ± 300 m (on 20 and 21 June).

The CEDOAS NO_3 data retrieval required several steps. (1) Zero air spectra, $I_0(\lambda)$, were recorded in the morning of each day of the campaign in the clean, flushed SAPHIR chamber containing only dry synthetic air (dew point < 220 K). (2) During the running experiment, the time series of measurement spectra, $I_m(\lambda, t)$, with absorbers (and aerosol extinction, in case of their presence) were recorded and the resulting optical density, $D_{CE}(t)$, was determined:

$$D_{CE}(t) = \ln\left(\frac{I_0(\lambda)}{I_m(\lambda, t)}\right) \quad (6)$$

Literature reference spectra of the present trace gases convoluted to the spectral resolution of the instrument and a second-order polynomial accounting for all broadband absorption effects were fitted to the differential structures of the spectra according to the classical "DOAS procedure" (Platt and Stutz, 2008). The trace gas concentrations, C_0, were obtained from the retrieved column densities using the actual path length, X_0 (662 nm), of the respective day. In the case of small trace gas absorption and aerosol-free conditions the mixing ratios are properly accounted for. (3) If, however, light losses due to broadband and/or narrowband extinction processes were larger, i.e. during the aerosol experiments, then the effective path length in the cavity was reduced and consequently the mixing ratios C_0 had to be corrected according to the procedure described by Platt et al. (2009, Eq. 41):

$$C_{true} = C_0 \frac{e^{D_{CE}} - 1}{D_{CE}}. \quad (7)$$

As this correction relays on the absolute optical density, the long-term stability of the light source becomes of

importance. A scatter plot of the intensities of all zero air spectra $I_0(\lambda)$ acquired during the intercomparison, normalised to 1 ms integration time, showed a linear decrease with time (correlation coefficient $r = -0.991$). The corresponding zero intensity $I_0(\lambda, t)$ for each NO_3 measurement at time t during the campaign (to be used in Eq. 6) was calculated using the linear regression line through these data.

The typical precision of the CEDOAS technique varied between 3 and 6 pptv (1σ) for a data acquisition time of 5 min with the larger value for experiments with high water vapour concentrations or in the presence of high aerosol load. The total measurement accuracy was 8 % and takes into account a 3 % error of the light path length, X_0, calculation, 5 % uncertainty of the cross section, 5 % error of the effective cavity length, and the correction of the reduced path length of 3 %.

2.1.7 Differential Optical Absorption Spectroscopy, FZJ-DOAS

Forschungszentrum Jülich used broadband DOAS for in situ NO_3 measurements in SAPHIR. DOAS allowed for the separation of overlapping narrowband spectral structures of different atmospheric constituents with high selectivity (fingerprint detection). DOAS is "immune" against continuous (broadband) extinction processes caused by mirror coatings and Rayleigh and aerosol scattering (Platt and Stutz, 2008). The setup of the FZJ-DOAS instrument at SAPHIR has been described in Bossmeyer et al. (2006) and Brauers et al. (2007).

A Xenon short arc lamp (OSRAM, XBO75W/2, arc size $0.3 \times 0.5\,mm^2$) housed outside the chamber served as a light source. The light was collected in a fibre (400 µm, 2 m length) and transferred to the chamber via a telescope. The light entered and left the chamber through a quartz window. Inside the chamber the light travelled 48 times within a modified version of a White type multiple reflection system of 20 m base length (Doussin et al., 1999) equipped with enhanced aluminium-coated mirrors (average reflectivity ≈94 % between 600 and 700 nm). The optical components of the White cell were setup at the north and south sides of the chamber. After leaving the White cell, the light passed through a long-pass colour filter (Schott, OG530) to block excess light from entering the spectrograph. The light was guided via an optical fibre assembly into a temperature-stabilised (±0.25 K) Czerny–Turner type spectrograph ($f = 0.46$ m, spectral resolution 0.4 nm) equipped with a linear photo diode array (1024 pixels, 25 µm width, 2.5 mm length) detecting a spectral range from 601 to 690 nm. The spectra recording, handling and fitting was controlled by the DOASIS software package (Kraus, 2006).

The 1σ precision of the measurements was approximately 10 pptv for 1 min data acquisition time. The accuracy depended mainly on the uncertainty of the NO_3 cross section (5 %, 1σ). During the campaign an additional systematic variability by ±20 pptv was observed in the retrieved NO_3 mixing ratios which was taken additionally into the accuracy. We explain this effect by intermittent shifts of the arc emission point on the surface of the electrodes of the Xe lamps used during NO3Comp. As a result of the geometrical displacement of the arc, the light transmission of the White cell was different and also the spectral emission of the lamp changed slightly, which led to a different spectral baseline compared with the zero-intensity spectrum measured at the beginning of the experiment. A systematic bias of the retrieved NO3 mixing ratios was the consequence.

2.2 Atmosphere simulation chamber SAPHIR

The SAPHIR chamber has been primarily designed for the controlled investigation of atmospheric chemical reaction systems under conditions similar to those in the ambient atmosphere, by using typical mixing ratios of trace gas constituents. SAPHIR is also optimally suited for the comparison of sensitive instruments for atmospheric trace gas and radical measurements. Unknown interferences do not affect the measurements as the composition of the air is known and the well-mixed air in the chamber allows for comparable measurements of all participating instruments (e.g. Schlosser et al., 2007, 2009; Fuchs et al., 2010b,a; Rohrer et al., 2005; Bossmeyer et al., 2006; Brauers et al., 2007; Wegener et al., 2007).

The SAPHIR chamber consists of a double-walled Teflon FEP (DuPont) bag of cylindrical shape (length 18 m, diameter 5 m, effective volume 270 m^3, surface/volume ≈ 1 m^{-1}) that is held by a steel frame. The space between the inner and the outer tube (15 cm) is permanently flushed with ultra-clean nitrogen (purity > 99.9999 %) to prevent diffusion of gases from outside. The inner volume is always held 40 Pa over ambient pressure in order to avoid contamination with outside air and to keep the FEP film under tension. Losses by gas extraction by the instruments and small leaks are compensated for by a replenishment flow rate of 10 to 15 $m^3\,h^{-1}$ which dilutes all constituents in the chamber at a rate of 3.5 to 5.5 $\%\,h^{-1}$. The actual dilution is monitored by a flow controller and additionally by a gas-chromatographic measurement of an inert tracer (ethane) added to the chamber air. The chamber is housed within completely retractible metal blinds that keep the chamber in darkness as required for the detection of NO_3 radicals. The blinds can be opened if daylight exposure is needed (i.e. in NO_3 photolysis experiments). In order to minimise potential photolysis of NO_3 during daylight measurements, all flanges and other light leaks were carefully covered by black foil, resulting in a reduction of the NO_3 photolysis frequency in the chamber to $\ll 10^{-4}$ of the outside value.

The SAPHIR chamber is equipped with a comprehensive set of sensitive instruments comprising measurements of temperature, pressure, and humidity. NO and NO_2 are measured by chemiluminescence; O_3 is measured by UV absorption (Ansyco) and by chemiluminescence (modified

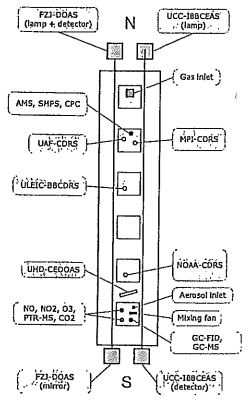

Fig. 1. Schematic top view onto the floor of SAPHIR with the positions of the individual instruments and inlet lines. The red lines indicate the open light paths of the FZJ-DOAS and UCC-IBBCEAS instruments, respectively. The UHD-CEDOAS open-path instrument was assembled on the floor of the chamber. All other NO_3 instruments drew air from flanges in the chamber floor at the designated positions.

ECO Physics CLD AL 700). Volatile organic compounds (VOC) are measured by gas chromatography using a flame ionisation detector (Chrompack) (Wegener et al., 2007) and by proton transfer reaction mass spectrometry (PTR-MS, IONICON, Austria) (Lindinger et al., 1998). An ultrasonic anemometer (USA) measures the gas temperature inside the chamber with an accuracy of ±0.2 K.

Aerosol number densities and size distributions were measured with a water condensation particle counter (TSI WCPC model 3785) and a scanning mobility particle sizer (TSI SMPS 3936, consisting of a differential mobility analyser (DMA 3081) and a WCPC 3785). The time resolution was 20 s for the CPC measurements and 7 min for the SMPS. A time-of-flight aerosol mass spectrometer (Aerodyne TOF-AMS) was operated to measure the aerosol chemical composition (Canagaratna et al., 2007). The AMS was connected to the SAPHIR chamber via a stainless steel tube designed to minimise losses in the sampling line (Fry et al., 2009).

Before each experiment, the chamber was purged with dry synthetic air overnight (from liquid N_2 and O_2, purity > 99.9999 %, flow rate up to 500 $m^3\,h^{-1}$) to parts per trillion (pptv) levels of nitrogen oxides, ozone, and hydrocarbons. If required, high-purity water (Milli-Q Gradient A10, Millipore Corp.) was evaporated in a steam generator and added to the purge flow at the end of the flushing of the chamber until the required humidity was reached. The trace gases (O_3, NO_2, and hydrocarbons) were added to the replenishment flow. The inlet port was located at the northern end of SAPHIR at the main inlet which is also used to flush the chamber (Fig. 1). Ozone was produced by silent discharge in pure oxygen. Ammonium sulphate, $(NH_4)_2SO_4$, aerosol was added directly by spraying an aqueous solution into the chamber using a nebuliser. The resulting size distribution had a count mean diameter of 70 nm, and the geometrical standard deviation was 1.56. For some experiments 500 ppmv of CO was added to the chamber before the reaction started in order to scavenge any OH radicals formed.

The homogeneity of the trace gas distribution in the chamber was established by a powerful fan which was mounted near the southern end of the chamber 1 m above the chamber floor. It was operated during all experiments. Measurements with the fan switched off showed noticeable mixing ratio differences between instruments which disappeared when the fan was running. Test measurements demonstrated that the inlet lines inside the chamber (lengths varied between 12 and 40 cm) sampled air from the well-mixed volume so that potential surface gradients were negligible when the fan was running. The absence of concentration gradients under well-mixed conditions was already demonstrated during the intercomparison of OH/HO_2 detection instruments (Schlosser et al., 2009) where different OH. instruments sampled air from 2 to 170 cm above the chamber floor.

Figure 1 shows the positions of the NO_3 instruments at SAPHIR. FZJ-DOAS, UCC-IBBCEAS, and UHD-CEDOAS detected NO_3 in situ inside the chamber. While the UHD-CEDOAS open-path instrument was set up 60 cm above ground, the absorption light paths of FZJ-DOAS and UCC-IBBCEAS extended along the central axis, about 1.7 m above the floor of SAPHIR. All other instruments were located beneath the chamber and sampled the chamber air through individual ports in the floor.

2.3 Intercomparison experiments

Chamber measurements were carried out in simple reaction mixtures to assess accuracy, precision, detection limits, and time response of the participating instruments. The experiments were performed in order of increasing chemical complexity. They were also designed to study the influence of species that potentially affect the measurement principles or retrieval approaches of the various instruments. Starting with water vapour and NO_2 (9 to 13 June), followed by organic molecules and their oxidation products (14 to 21 June), the influence of inorganic aerosol (15 and 18 June), and secondary organic aerosol (SOA) formed during in situ

Table 1. List of experiments performed during NO3Comp. The mixing ratios of key constituents are maximum values measured during the experiments. Ambient and dew point temperature ranges are given as well as the experiments' scopes.

Date	NO_2 ppbv	O_3 ppbv	NO_3 pptv	N_2O_5 pptv	HNO_3 ppbv	T_{amb} °C	T_{dew} °C	Experiment
9 Jun	4	120	130	350	[a]	20.2–22.6	−43.6…−38.5	Stepwise change of NO_2
10 Jun	4	230	170	300	0.7	18.2–28.5	−42.3…+9.2	Stepwise change of humidity
11 Jun	17	100	150	750	1.2	23.9–31.5	+8.7…+15.3	Measurements in ambient air including aerosol
12 Jun	8	200	400	1600	[a]	17.3–20.2	−57.2…−48.7	Short photolysis events
13 Jun	18	200	700	2200	4	18.2–29.5	−45.5…−43.7	Short photolysis events
14 Jun	12	135	180	850	6	19.3–28.1	−61.1…−47.7	Oxidation of butanal (max. 4 ppbv)
15 Jun	10	180	120	550	2	18.7–24.2	−58.9…+15.1	Addition of inorganic aerosol ($(NH_4)_2SO_4$)
16 Jun	38	60	55	1300	1.3	16.2–23.2	−50.4…−44.6	Oxidation of limonene[1] (max. 10 ppbv) + CO (500 ppmv)
17 Jun	11	19	40	770	[a]	13.2–22.9	−44.5…−47.6	Experiment of 16 Jun continued
18 Jun	33	60	150	1400	4.5	18.3–27.7	−1.2…+9.2	Oxidation of isoprene[2] (max. 10 ppbv) + $(NH_4)_2SO_4$ seed aerosol + CO (500 ppmv)
20 Jun	75	100	400	5300	8	20.8–28.7	−56.0…−46.3	Oxidation of β-pinene[3] (max. 20 ppbv)
21 Jun	70	165	110	6000	3	18.3–20.4	−61.5…+10.9	Oxidation of β-pinene[3] (max. 20 ppbv)

[a] no valid measurements; [1] Fry et al. (2011); [2] Rollins et al. (2009), [3] Fry et al. (2009).

experiments (16, 20, 21 June) was investigated (see Table 1). In order to allow for a full investigation of possible interferences with other unknown atmospheric components, ambient air was pumped into the chamber on 11 June. All simulation studies were performed under virtually ambient pressure and temperature so that the performance of the instruments was investigated under realistic, near-atmosphere conditions.

Experiments usually started by adding NO_2 and O_3 into the either dry or humidified synthetic air of the chamber. Maximum NO_3 mixing ratios established typically after an hour. In many experiments the chemical system was "refuelled" after some time by a second addition of NO_2, O_3 or both. Fast modulations of the NO_3 mixing ratio were initiated by the injection of reactive hydrocarbons (16, 18, 20 and 21 June) or by photolysis with ambient sunlight after opening the shutters of the SAPHIR chamber (12 and 13 June and at the end of most experiments in the afternoon).

3 Observations and results

3.1 Precision of the instruments

The instrumental precision was a key parameter required for a statistically sound regression analysis. The precision of the instruments was investigated under conditions of vanishingly small NO_3 mixing ratios. All measurements in the clean chamber after flushing with synthetic air over night ("zero air" data) were included, but also NO_3 data during the preparation phase of the experiments were selected, i.e. times were chosen when the chamber air already contained hydrocarbons, ozone *or* NO_2 (aerosol excluded), but, in any case, before the formation of NO_3 was initiated.

In Fig. 2 the frequency distributions of zero-NO_3 measurements are shown. The optimal bin size to be used for the histograms depends on the sample size and the spread of the data range and was selected after Freedman and Diaconis (1981). A Gaussian distribution of the same area as the measured data was fitted to the histograms to visualise the mean of the zero measurements and their standard deviation, which is a measure of the actual instrumental precision. The histogram of the MPI-CRDS instrument is not included because the number of available zero air data ($n = 7$) was too small for a meaningful statistic. The calculated values of Skewness and Kurtosis for the histograms of UCC-IBBCEAS and UAF-CRDS (1.36/3.43 and 0.92/3.46, respectively) show significant differences from zero which indicate that these two data sets are most likely not normally distributed.

NOAA-CRDS (time resolution $\Delta t = 1$ s), UAF-CRDS ($\Delta t = 1$ s), ULEIC-BBCRDS ($\Delta t = 1$ min), and UCC-IBBCEAS ($\Delta t = 5$ s) show excellent precision in the range of 0.5 to 2 pptv, and the calculated mean NO_3 mixing ratios deviate no more than ±0.2 pptv from zero. The precision of UHD-CEDOAS ($\Delta t = 5$ min) and FZJ-DOAS ($\Delta t = 1$ min) is in the range 5 to 10 pptv, and the mean of the frequency distributions is biased to marginally higher values (≈2 and 4 pptv, respectively). The precision of the MPI-CRDS instrument ($\Delta t = 10$ s), as estimated from visual comparison of measurements at NO_3 mixing ratios < 35 pptv on 16 June (Fig. 4), is comparable to the other CRDS instruments.

In part (a) of Table 2 the mean NO_3 mixing ratio is compared with the corresponding confidence interval $2\sigma/\sqrt{n}$. Given the high precision of the measurements and the large number of data points n, the observed deviation from zero is extremely small but statistically significant for all instruments except ULEIC-BBCRDS whose observed

Table 2. (a) Mean NO_3 mixing ratio (centre of the frequency distribution, Fig. 2) and the corresponding confidence interval, $\frac{2\sigma}{\sqrt{n}}$. (b) Comparison of the mean of the errors of zero-NO_3 measurements ($\langle\sigma\rangle$) with the precision calculated from the frequency distribution of zero data (1σ width of the Gaussian distribution). All values are in pptv.

		FZJ DOAS	NOAA CRDS	UAF CRDS	ULEIC BBCRDS	UCC IBBCEAS	UHD CEDOAS
(a)	Mean NO_3	2.1	0.2	−0.2	0.1	0.2	3.4
	$\frac{2\sigma}{\sqrt{n}}$	0.70	0.01	0.05	0.38	0.03	1.38
(b)	$\langle\sigma\rangle$	9.4 ± 7.4	0.4 ± 0.2	1.3 ± 1.0	0.9 ± 0.7	0.9 ± 0.6	3.7 ± 1.9
	1σ	8.5	0.5	1.9	1.7	0.9	5.6

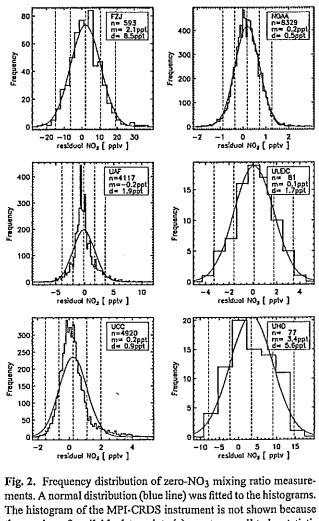

Fig. 2. Frequency distribution of zero-NO_3 mixing ratio measurements. A normal distribution (blue line) was fitted to the histograms. The histogram of the MPI-CRDS instrument is not shown because the number of available data points (n) was too small to be statistically meaningful. The 1σ standard deviation, d, is a measure for the instrumental precision during NO3Comp; m denotes the mean NO_3 mixing ratio.

deviation at zero is within the uncertainty interval. The lower part (b) of the table compares the mean of the errors of zero-NO_3 measurements ($\langle\sigma\rangle$) with the precision calculated from the frequency distribution of zero data (1σ width of the Gaussian distribution in Fig. 2). Within the calculated uncertainty no significant difference can be found, meaning that the a priori estimation of the measurement errors by the operators of each instrument correctly describes the statistical variation of the instruments.

3.2 Time series of NO_3 measurements

Time series of NO_3 mixing ratios and key constituents (NO_2, O_3, and hydrocarbons), as well as water vapour partial pressure, and the total aerosol surface concentration for each day are presented in Figs. 3 and 4. The NO_3 data are plotted with the original time resolution that each instrument's data reported, without any further averaging or filtering. Error bars are omitted for clarity.

NO_3 mixing ratios throughout the campaign were below 250 pptv with three exceptions on the "photolysis days" (12 and 13 June, 350 and 700 pptv) and on the "SOA day" (20 June, 400 pptv). Exceptionally low NO_3 mixing ratios occurred on 16 June (≤ 40 pptv) and especially on 18 June when NO_3 mixing ratios remained between 2 pptv after the first isoprene injection and 12 pptv after a second addition (see Fig. 4). Prior to the discussion of the individual NO_3 time series of each experiment of the campaign, some discernible features in the figures merit discussion.

1. NO_3 mixing ratios measured by UCC-IBBCEAS on 10, 11, 13, 15, and 20 June significantly differed from the values of all other instruments (Figs. 3 and 4). A similar observation for the UCC instrument was described by Fuchs et al. (2010a) for the comparison of NO_2 measurements performed during NO3Comp. The systematic difference of the NO_3 mixing ratios can be explained by the fact that on those days no measurements of zero air background spectra ($I_0(\lambda)$, Eq. 3) could be taken in the morning before the experiments for the following reasons. On 10, 15, and 20 June, NO_3 was already produced in the chamber before the

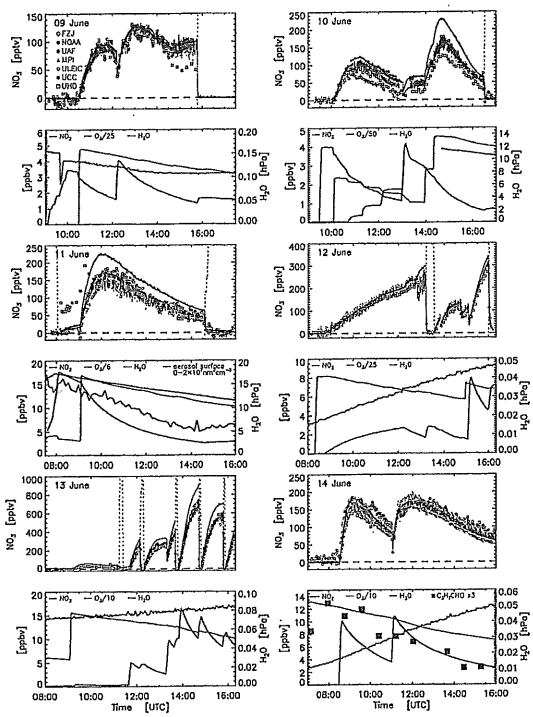

Fig. 3. Comparison of temporal profiles of NO_3 mixing ratios and supporting measurements of other relevant species (as indicated in the panels) for all days of the intercomparison campaign. The respective upper panels show NO_3 data measured with the original time resolution of the instruments (NOAA-CRDS 1 s, UAF-CRDS 1 s, UCC-IBBCEAS 5 s, MPI-CRDS 10 s, FZJ-DOAS 60 s, ULEIC-BBCRDS 61 s, and UHD-CEDOAS 300 s). Vertical, dashed grey lines indicate times when the roof of the chamber was opened or closed to initiate photolysis or enable the build-up of NO_3, respectively. The associated lower panels present the mixing ratios of NO_2, O_3, hydrocarbons (ppbv, left axis), and the water vapour partial pressure (hPa, right axis). For experiments containing aerosol, the aerosol surface area concentration is indicated by a black line (in units of $nm^2\,cm^{-3}$, no separate axis associated, full data span specified in the legend).

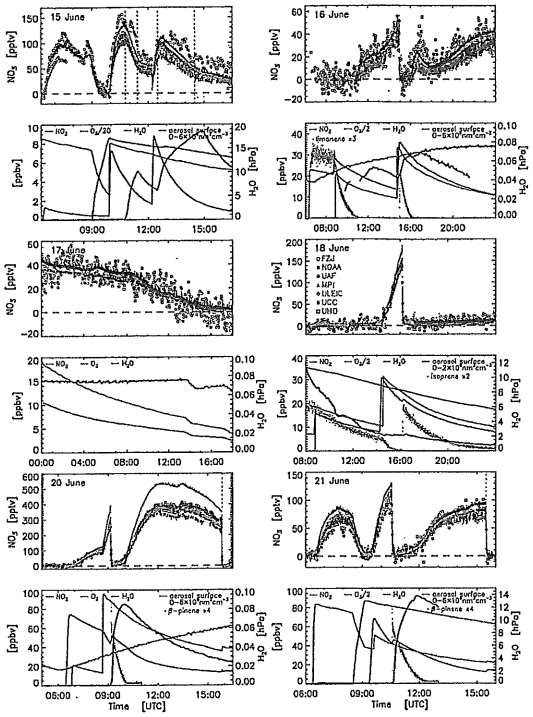

Fig. 4. Continued from Fig. 3. This figure comprises the chemically more complex experiments of the second part of the campaign. Dotted black lines on 15 June denote two time intervals during which inorganic aerosol was added to the chamber.

intensity variation of the lamp was a limiting factor for the UCC-IBBCEAS instrument during some experiments of NO3Comp.

2. Mixing ratios taken with the ULEIC-BBCRDS instrument on 10 June were exceptionally low (orange diamonds in Fig. 3). At the end of the experiment it was noticed that the sampling line had collapsed. Therefore it had to be assumed that during the experiment the flow rate was potentially already much smaller than expected, resulting in enhanced losses of NO_3 in the instrument.

3. On 11 June the ULEIC-BBCRDS data exhibited the strongest fluctuations during NO3Comp. The amount of ambient air that was found to be leaking into the BBCRDS cavity (see Sect. 2.1.4) was highly variable, ranging between 0 and 30 %. Quantitative correction of the dilution effect was difficult to achieve under these conditions, resulting in less-precise measurements on that day.

4. Also the performance of the UHD-CEDOAS instrument was degraded on 11 June in the morning. The chamber was flushed with open roof, leading to an overheating of the LED light source by solar radiation. The induced drift of the LED output made the spectral retrieval unreliable as demonstrated by the large positive offset of the NO_3 data before 09:45 UTC (Fig. 3).

5. On 9 June (14:38 UTC) and on 12 June (12:46 UTC) the fan inside the chamber was switched off some time before the roof was opened. In stagnant air, the mixing time in the dark chamber is on the order of an hour. This is considerably longer than the NO_3 lifetime of 30 min (Fry et al., 2009) in the dry chamber, making wall reactions of NO_3 a significant loss process and enabling measurable concentration gradients to build up. Consequently, these episodes of inhomogeneous sampling conditions were excluded from further data analysis.

In order to get a representative picture of the instrument performance throughout the campaign, the data on these occasions where specific instrument issues have been identified are still included in calculating the full-campaign correlations (except 5). The following paragraphs describe the time series of the NO_3 mixing ratios recorded during NO3Comp. A brief summary of the typical mixing ratios of key constituents observed during the experiments is given in Table 1.

9 June, 10 June: during the first part of the campaign (9–14 June) the majority of measurements were carried out in simple reaction mixtures. On 9 and 10 June a potential cross interference of NO_2 and water vapour was investigated, respectively. With the exception of the scenarios discussed above the NO_3 mixing ratios of all instruments agree well and mostly overlap within their errors. On 10 June the data of the UHD-CEDOAS instrument tend to lower values at higher water vapour mixing ratios.

11 June: an experiment with ambient aerosol was performed on 11 June. The chamber was flushed with ambient air while the roof was open in order to avoid NO_3 formation during the flushing period. A filter (cut-off size unknown) removed coarse-mode particles. The resulting aerosol surface concentration was very low and did not vary much ($(1.3\ldots0.5)\times10^7\,nm^2\,cm^{-3}$) during the experiment (Fig. 3). The aerosol mass spectrometer could not measure due to the low particle concentration; therefore chemical properties of the aerosol are unknown. Peak mixing ratios of NO_2, O_3, and water after closing the roof at 08:01 UTC were 23 ppbv, 25 ppbv, and 1.7 %, respectively. At 09:04 UTC formation of NO_3 was stimulated by addition of 70 ppbv O_3 into the dark chamber. Technical problems affected UHD-CEDOAS, ULEIC-BBCRDS, and UCC-IBBCEAS (see above), but NOAA-CRDS, FZJ-DOAS, and UAF-CRDS data were very similar throughout the day.

12 and 13 June: on these "photolysis days" the NO_3 production rate was high and the chemical losses were low, leading to the largest NO_3 mixing ratios of the campaign (700 pptv on 13 June). NO_3 was frequently photolysed on both days by opening and closing the roof system of the SAPHIR chamber. The photolytic lifetime of NO_3 was approximately 5 s when the roof was open; however the observed NO_3 lifetime was approximately 1 min because the fast thermal dissociation of N_2O_5 (present at $\approx$ 2 ppbv; Fuchs et al. (2012)) acted to partially buffer the NO_3 lost to photolysis. Figure 3 clearly demonstrates the very good time resolution of the "faster" instruments, NOAA-CRDS, UAF-CRDS, UCC-IBBCEAS, and MPI-CRDS, which were able to detect the quick changes of NO_3 very accurately.

14 June: in this experiment the oxidation of butanal by NO_3 was studied. The measurements revealed very good agreement between the instruments. However, the sensitivity of the UHD-CEDOAS instrument seemed to have changed after 10:00 UTC probably due to a temperature change of the LED.

15 June: during this experiment ammonium sulphate aerosol was generated and added twice during 10:45–11:25 and 12:30–14:55 UTC (black dotted lines in Fig. 4) by spraying an aqueous solution into the clean humidified (60 % RH) chamber using a nebuliser. Peak aerosol surface concentrations of 3×10^8 and $5.8\times10^8\,nm^2\,cm^{-3}$, corresponding to 5 and 12 $\mu g\,m^{-3}$, respectively, were reached at the end of the injection periods. During the humidification of the aerosol-free chamber air (starting at 09:00 UTC) the mixing ratio of NO_3 dropped to zero. The addition of O_3 and NO_2 at 09:56 UTC brought the NO_3 mixing ratio back up to about 110 pptv (Fig. 4). The first aerosol generation began at the maximum of the NO_3 mixing ratio which then decreased to about 50 pptv due to the enhanced dilution of the chamber air by the high air flow through the aerosol generator. At the start of the aerosol addition the

UCC-IBBCEAS instrument was operational, on 11 June ambient air was pumped into the chamber, and on 13 June the previous experiment was continued over night without flushing in the morning. Zero air spectra from the day after or before were used for the retrieval of the NO_3 mixing ratios in these cases. Notably, differences in the NO_3 mixing ratio measured by UCC-IBBCEAS and other instruments are expected to be largest on days when the background spectrum could not be measured. This indicates that the long-term readings of UHD-CEDOAS, ULEIC-BBCRDS, and UAF-CRDS corresponded well (115 pptv at 10:45 UTC), while UCC-IBBCEAS and FZJ-DOAS measured 135 pptv and NOAA-CRDS was lowest at 100 pptv. After the first aerosol addition was finished (11:25 UTC), the NO_3 mixing ratios reported by ULEIC-BBCRDS, UHD-CEDOAS, and particularly by UAF-CRDS had dropped significantly below the NOAA-CRDS readings. During the subsequent second particle injection, the aerosol surface concentration nearly doubled, but no further significant change of the relation between NOAA-CRDS and the other instruments was observed except for the ULEIC-BBCRDS instrument. NO_3 data measured after 13:45 UTC until the end of the experiment agreed well with the NOAA reference instrument but were lower by about 16 pptv prior to this. Most likely the pronounced underestimation of the NO_3 mixing ratio before 13:45 UTC was caused by an intermittent problem with a leak as a comparison of the ULEIC water vapour data with a dew point hygrometer inside SAPHIR suggested. The FZJ-DOAS instrument showed excessive fluctuations caused by the unsteady arc of the Xe high-pressure lamp, making the NO_3 measurements unreliable on 15 June.

16 and 17 June: during this two-day experiment the limonene–NO_3 reaction and the formation of products, both in the gas and in the particulate phase, were studied (Fry et al., 2011). Limonene (10 ppbv) was already injected before NO_3 was generated, so that the NO_3 mixing ratio remained suppressed below the detection limit of all instruments. After limonene was fully consumed, the ongoing reaction between NO_2 and O_3 caused NO_3 mixing ratios to rise to about 35 pptv. About 10 $\mu g\,m^{-3}$ of aerosol was formed, resulting in an aerosol surface concentration of $3\times10^8\,nm^2\,cm^{-3}$. Data from all instruments compare well under these conditions except for FZJ-DOAS and UCC-IBBCEAS, which showed a trend to slightly higher NO_3 mixing ratios (difference remained <5 pptv). The FZJ-DOAS instrument was close to the detection limit ($S/N \approx 1$ to 3) on that day. The second limonene injection at 15:00 UTC on 16 June occurred almost simultaneously with the addition of NO_2 and O_3. During the second oxidation step further aerosol was formed, peaking at 24 $\mu g\,m^{-3}$ ($4\times10^8\,nm^2\,cm^{-3}$). As expected, NO_3 started to rise again quickly after limonene was consumed. The observed unexpected decrease of the NO_3 mixing ratio reaching a minimum at 18:00 UTC (Fig. 4) was due to complex coupling of the chemistry in the gas phase with that of the organic particle phase and has not been fully understood yet (Fry et al., 2011). ULEIC, MPI, and UHD finished measurements at 13:30, 15:50, and 16:40 UTC, respectively, before the NO_3 mixing ratios again began to rise up until midnight. During the last six hours of the 16 June data the differences between the readings of the remaining instruments increased.

NOAA-CRDS, UCC-IBBCEAS and FZJ-DOAS continued their measurements until 17 June, 19:00 UTC. No aerosol measurements were available for that day. UAF-CRDS commenced measurements again at 08:00 UTC after the replacement of an aerosol filter. With a new filter in the inlet, the instrument detected slightly larger NO_3 mixing ratios than NOAA-CRDS, while the opposite was the case on 16 June, indicating a potential loss of NO_3 by aerosol particles deposited on the UAF-CRDS instrument's filter surface.

18 June: the oxidation of isoprene by NO_3 in the presence of ammonium sulphate seed aerosol was studied on 18 June (Rollins et al., 2009). The first isoprene injection (10 ppbv at 07:40 UTC) was made before any NO_3 was generated (the NO_3 production started after ozone injection at 08:48 UTC), and the second isoprene injection (10 ppbv at 16:11 UTC) occurred two hours after the system was refuelled by NO_2 and O_3 addition. In the first part of the experiment the NO_3 mixing ratio reached peak values of only 2 pptv; at the end of the experiment at midnight NO_3 was less than 12 pptv, still close to the detection limit of FZJ-DOAS and UHD-CEDOAS. The aerosol surface concentration in the morning reached $1.3\times10^8\,nm^2\,cm^{-3}$, about 20 % of the maximum value on 15 June, and gradually decreased to $0.2\times10^8\,nm^2\,cm^{-3}$. The fast increase of NO_3 after mid-afternoon refuelling additions of NO_2 and O_3 was very well captured by all instruments. NO_3 mixing ratios detected by UCC-IBBCEAS appear to be 5–10 % higher before isoprene was injected.

20 and 21 June: on the last two days of the campaign the oxidation of β-pinene in dry air and at 60 % RH, respectively, was investigated. After the injection of β-pinene the NO_3 mixing ratio dropped to 20 pptv and 5 pptv, respectively, and remained suppressed until the hydrocarbon had reacted completely. Prompt SOA formation was observed reaching a maximum concentration of 40 $\mu g\,m^{-3}$, corresponding to an aerosol surface concentration of $5.6\times10^8\,nm^2\,cm^{-3}$, about 45 min and 90 min, respectively, after injection of the hydrocarbon (Fry et al., 2009). After the consumption of β-pinene, the NO_3 mixing ratio increased again to a maximum of 400 and 80 pptv, respectively. During this period the high precision of the instruments allowed the investigators to visualise an increasing difference in the NO_3 mixing ratios as measured by the instruments over time. A detailed discussion will follow in Sects. 3.3.3 and 4.4.2.

3.3 Correlation and regression analysis

3.3.1 Correlation procedure

In order to assess the performance of the individual instruments, all NO_3 data sets were compared to one selected instrument. We chose the NOAA-CRDS NO_3 measurements as the reference for the correlation analysis for three reasons. (1) The NOAA-CRDS instrument was the technically most advanced one (see Sect. 2.1.1). Its properties were comprehensively studied and characterised in detail before and after the campaign (Dubé et al., 2006; Osthoff et al., 2006; Fuchs et al., 2008). (2) The NOAA instrument measured on all days of the campaign and produced the most complete data set. (3) The instrumental precision and consequently the

detection sensitivity and time resolution are excellent, so potential features in the correlation plots can be clearly identified. Especially the latter property favoured NOAA-CRDS over FZJ-DOAS, which would normally have been our preferred choice, because the DOAS instrument has no inlet – one of the major uncertainties of the other instruments. In addition, DOAS is known to be "immune" against broadband light losses caused by Mie scattering of particles, Rayleigh scattering, or by other broadband absorbers in the atmosphere (Platt and Stutz, 2008). Unfortunately, the FZJ-DOAS measurements turned out to be unusually noisy and showed sudden systematic variations during many days. The latter were most likely due to instabilities of the Xe arc lamps used during NO3Comp. If DOAS had been chosen as reference, then excessive noise would have been added to all regressions. A comparison of the results of a regression analysis with FZJ-DOAS or NOAA-CRDS as reference instrument showed that the major conclusions drawn from the correlations did not depend on the choice of the reference. We would like to emphasise that our selection shall not imply that the NOAA-CRDS data are inherently correct.

The correlation and regression analysis presented in the following sections are based on data sets averaged to a 3 min time grid which allows for the comparison of fast and slower instruments within common time intervals. It was verified that the choice of the averaging interval does not significantly affect the results. In order to minimise potential errors by imperfect mixing in the chamber, all NO_3 mixing ratios measured within a time interval of 5 min after injection of reactive trace gases (NO_2, O_3, and hydrocarbons) were removed from the analysis.

In the case of multiple NO_3 data points within one averaging interval, the mean value was calculated and assigned to the centre of the time interval. Data of "slower" instruments were assigned to the centre of the interval where they appeared. Whenever the observed variability of the NO_3 mixing ratios within the averaging interval was comparable with the individual measurement errors, the standard deviation of the error bars was taken as 1σ error of the mean. If the data variability was larger, the standard deviation of the mixing ratios was taken as the error bar of the mean value (Schlosser et al., 2009; Fuchs et al., 2010a).

A weighted linear regression line was calculated using the procedure "fitexy" by Press et al. (1992). This regression is invariant with respect to a permutation of independent and dependent variable and takes into account the errors of both coordinates. Thus, the statistical weight of each data point is calculated from the a priori precision of the data of both the respective instrument and NOAA-CRDS. In order to assess the statistical relevance of the linear regression parameters and their errors, the chi-square (χ^2) value of the linear fit to the measurements was calculated. A rule of thumb is that a "typical" value of χ^2 for a "good" fit is $\chi^2 \approx (n-2)$ (n...number of data pairs correlated) (cf. Press et al., 1992, Chapter 15). Furthermore a "goodness-of-fit" parameter q was calculated from the chi-square distribution for $(n-2)$ degrees of freedom. It denotes the statistical probability that the deviation of the χ^2 value (obtained for some particular data set) from the "expected" $\chi^2 = n-2$ value can be explained within the individual 1σ measurement errors of the data pairs correlated. If q is a very small probability, then the inherent variance of the data set is larger than the "confidence interval" defined by the individual error bars. Possible causes are that (1) the assumption of a linear model is wrong, (2) the errors are non-normally distributed, or (3) the measurement errors are really larger than stated. As an order of magnitude estimate the assumption of a linear dependency between the instruments within the range of their given measurement errors is believable if $q \geq 0.1$. For $q \geq 0.001$, the fit may be acceptable if the errors are non-normally distributed or have been moderately underestimated. If $q < 0.001$, a linear relationship within the specified errors can be called into question. However, q is a very sensitive quantity for underestimated measurement errors. Often truly wrong models will be rejected with vastly smaller values of q (10^{-18}). The opposite extreme, $q \approx 1$, is almost always caused by overestimation of the measurement errors by the experimenter (Press et al., 1992).

3.3.2 Correlations of combined data sets

It was already indicated in Sect. 3.2 that the performance of some NO_3 instruments could be affected by the presence of aerosol. A similar observation has been described by Fuchs et al. (2012) for the intercomparison of N_2O_5 measurements during NO3Comp. Therefore the scatter plots and the correlation and regression analysis of the NO_3 data will be presented in separate figures for aerosol-free (Fig. 5) and aerosol-containing experiments (Fig. 6). Each panel in Figs. 5 and 6 shows the entire campaign data set for the nominated instruments plotted as a scatter plot against the NOAA-CRDS reference instrument. The figures visualise the total variability of the instrumental performance relative to the NOAA instrument, and the regression results allow for a comparison of the "average response" of the instruments during NO3Comp. The individual days of the campaign are distinguished by colour-coded symbols, and the error bars denote the 1σ precision. The data range is limited to 420 pptv to avoid any bias by the high NO_3 mixing ratios on 13 June.

On average all instruments performed very well over the course of the intercomparison. The NO_3 mixing ratios of all instruments are exceptionally well linearly correlated with NOAA-CRDS. The coefficients of determination, r^2, are > 0.955 in all cases (Table 3), i.e. more than 95 % of the variance observed in the instruments' responses is explained by the variance of the reference instrument. Due to the large number of data points, n, all correlations are highly significant. However, the regression analysis resulted in χ^2 values which are significantly larger than the number of degrees of freedom $(n-2)$ (last column in Table 3). Accordingly q was $< 10^{-10}$ in all cases and is therefore not listed in Table 3. This finding shows that the variance in the NO_3 data set of each instrument, considered over the entire course of the campaign, was significantly larger than would be expected from the high precision of the measurements. Obviously the daily variability of the instrumental response was larger than the data variability during the single days. Consequently, the use of the data precision as weighting factor is not a suitable measure for the investigation of the "average" (linear) relationship between the instruments during NO3Comp. While the individual measurement errors during a specific chamber experiment can be assumed to be normally distributed with a mean zero and constant variance, the statistical distribution of the day-to-day variability of the "calibration factors" is not known. As a consequence, for the days where $\chi^2/(n-2) \gg 1$ (i.e. when q is not acceptable), the "fitexy" routine is not well suited to calculate correct values and errors of intercept a and slope b (Press et al., 1992). A more appropriate non-parametric line-fitting technique is to be used which makes no assumptions on the distribution function of the data and their errors. We applied the "least-normal-squares" (LNS) technique (Troutman and Williams, 1987), which minimises the sum of squared perpendicular distances between the data points and the regression line. LNS is invertible and a unique relation (slope and intercept) is obtained regardless which variable is chosen to be dependent. In order to determine the goodness of the procedure for fitting the straight line, i.e. the errors σ_a and σ_b, a bootstrap technique was used. Bootstrapping is a non-parametric approach to determine statistical properties of data sets that does not require distributional assumptions such as normally distributed errors (Efron and Tibshirani, 1993). An application of this method for the determination of measurement errors in high-resolution DOAS

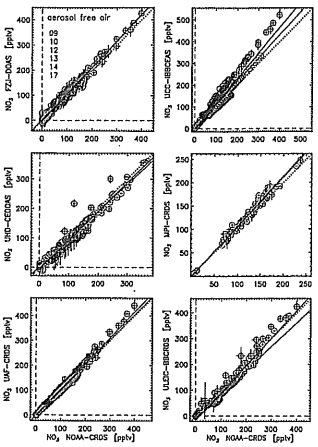

Fig. 5. Correlation of NO_3 measurements versus the reference instrument NOAA-CRDS for aerosol-free conditions. The data sets were averaged onto a common 3 min time grid, and the data range was limited to 420 pptv to exclude any bias by the high mixing ratios of 13 June. The colour code denotes the experiment days and error bars are 1σ. The "best-fit" line (dark-red solid line), calculated by a "least-normal-squares" regression method, represents the average instrumental response for the entire intercomparison and the dotted black line shows the ideal 1 : 1 line. The solid grey lines are the linear regression lines calculated by the "fitexy" algorithm. When the scatter of the data is significantly larger than expected from the measurement errors, the "fitexy" algorithm fails to determine the correct relation between the data pairs (cf. Sect. 3.3.2 and Table 3).

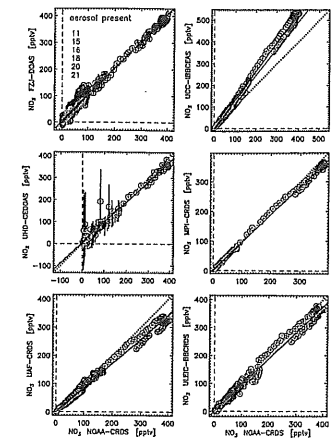

Fig. 6. Correlation of NO_3 measurements versus the reference instrument NOAA-CRDS in presence of aerosol. See Fig. 5 for details on the regression lines.

spectroscopy was described by Hausmann et al. (1999). The total bootstrap procedure comprises three steps: (1) a large number, m, (typically $m \approx 1000$) of independent replicas from the data set under investigation (selected NO_3 instrument vs reference instrument) are created by drawing with replacement a random sample of data pairs of the original data set. (2) The linear regression parameters intercept, a', and slope, b', for each replica are calculated. (3) The standard deviations of the m values of a' and b', $\sigma_{a'}$ and $\sigma_{b'}$, finally represent the errors of the intercept, a, and the slope, b, of the LNS correlation line. The LNS line fit parameters (the "best-fit" linear regression) are highlighted in Table 3 and shown as dark-red solid lines in Figs. 5 and 6. Significant deviations of slope and intercept between fitexy (solid grey lines in the figures) and LNS mainly result for large chi-squared test values ($\gtrapprox 15$). The "best-fit" linear regression line represents the average instrumental response for the entire intercomparison.

The LNS regression analysis reveals small intercepts close to the specified precision of the instruments. The slopes of the linear regression lines vary less than 15 % around unity for the whole-campaign correlations with the known exception of UCC-IBBCEAS (problem of recording zero air background spectra). Between the experiments with and without aerosol a tendency to underestimate the NO_3 mixing ratios in the presence of aerosol can be found for all instruments except FZJ-DOAS, which correlates very well with NOAA-CRDS, again demonstrating its insensitivity to broadband light extinction by aerosol. Overall we can state that the slopes of the regression lines are all within the combined 1σ-accuracies of the nominated test instruments and NOAA-CRDS. This demonstrates that the instrumental accuracy was very well determined by the experimentalists.

3.3.3 Day-to-day correlations

Day-to-day variations of the detection sensitivity or different responsivity of the instruments towards interferences become more apparent in scatter plots that compare data separated into individual days' experiments. Figures 7 and 8 show the correlations of NO_3 data of all instruments versus NOAA-CRDS for each experiment of the NO3Comp campaign (cf. Table 1). Error bars are omitted for clarity. In order to assess the effect of aerosol on the quality of the measurements on 11 and 15–21 June, only NO_3 data are compared which were recorded in the presence of aerosol.

The regression parameters are summarised in Table 4. Slopes and intercepts of the regression lines were calculated by the routine "fitexy" because the majority of the data sets showed reduced chi-square values < 15 (cf. Sect. 3.3.2). For every day the slopes of the linear regression lines fitted to the data were within the limits of the combined accuracies of the instrument pairs (as based on the a priori uncertainty estimates provided for each instrument by its operators). Only on four days (10, 11, 13, and 20 June) did the slopes of UCC-IBBCEAS slightly exceed these limits for reasons already stated.

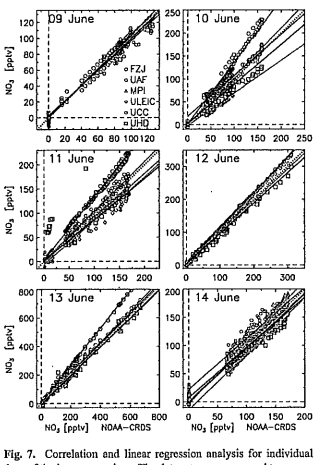

Fig. 7. Correlation and linear regression analysis for individual days of the intercomparison. The data sets were averaged to a common 3 min time grid. Linear regression lines calculated with the "fitexy" algorithm are shown colour coded for the particular instruments. The dotted black line is the ideal 1 : 1 line. Error bars were omitted for clarity.

9, 10 and 11 June: the experiments on 9 and 10 June will be discussed in detail in Sects. 4.2 and 4.3. On 11 June data correlated very well during the measurements in ambient air ($r^2 > 0.963$). The UAF-CRDS data are very well linearly correlated with NOAA-CRDS ($q = 0.85$). The apparent linear correlation of UHD-CEDOAS was caused by the very large errors of the instrument on 11 June (see Sect. 3.2 and green symbols in Fig. 6).

12 and 13 June: NO_3 was completely photolysed several times during the clean air/photolysis days (12 and 13 June). The large dynamic range of ≈ 700 pptv allowed for tests of the linearity of the instruments. The measurements correlated extremely well; r^2 varied between 0.975 and 0.999. The linear regression analysis revealed very good linearity over the full dynamic range of NO_3 mixing ratios on 13 June and insignificant intercepts.

Table 3. Results of the correlation and linear regression analysis of NO_3 measurements from all instruments versus NOAA-CRDS as reference on the basis of 3 min averages. (a) Measurements in the absence of aerosol (cf. Fig. 5), (b) in the presence of aerosol (cf. Fig. 6). n... number of data pairs, r^2... Pearson linear correlation coefficient, $\chi^2/(n-2)$... reduced chi-squared. A value of ≈ 1 indicates that the scatter of the data around the regression line is well covered by the individual 1σ measurement errors (precision) of both instruments. When the scatter of the data is larger, "fitexy" fails to calculate the correct regression parameters and their errors. The italic numbers indicate the slope and intercept for an appropriate regression model ("least normal squares", LNS). For details see text in Sect. 3.3.2.

	Instrument	n	r^2	Intercept/pptv	Slope	$\frac{\chi^2}{(n-2)}$
(a)	FZJ	542	0.978	2.9 ± 0.5	1.05 ± 0.005	2.7
				1.0 ± 0.5	*1.05 ± 0.006*	
	UAF	654	0.992	-0.4 ± 0.3	1.01 ± 0.002	2.2
				-1.8 ± 0.4	*1.04 ± 0.006*	
	MPI	154	0.984	-2.1 ± 0.6	1.08 ± 0.004	4.1
				-0.3 ± 1.3	*1.06 ± 0.011*	
	ULEIC	250	0.964	-3.3 ± 0.4	0.91 ± 0.002	12.6
				-17.7 ± 2.5	*1.07 ± 0.021*	
	UCC	698	0.956	1.6 ± 0.3	1.08 ± 0.002	53.7
				-4.2 ± 0.9	*1.18 ± 0.015*	
	UHD	246	0.955	2.5 ± 0.5	0.93 ± 0.004	4.6
				-4.5 ± 1.6	*0.98 ± 0.016*	
(b)	FZJ	855	0.989	4.8 ± 0.3	1.00 ± 0.002	3.3
				5.2 ± 0.4	*1.00 ± 0.003*	
	UAF	856	0.994	-0.5 ± 0.1	0.87 ± 0.001	3.7
				0.6 ± 0.2	*0.85 ± 0.005*	
	MPI	242	0.991	1.1 ± 0.4	0.94 ± 0.001	7.5
				2.3 ± 0.3	*0.93 ± 0.002*	
	ULEIC	465	0.991	1.2 ± 0.2	0.92 ± 0.001	46.
				1.0 ± 0.4	*0.94 ± 0.005*	
	UCC	879	0.996	0.9 ± 0.1	1.23 ± 0.001	115.5
				-2.8 ± 0.3	*1.34 ± 0.005*	
	UHD	246	0.981	3.5 ± 0.5	0.93 ± 0.003	3.1
				6.1 ± 1.3	*0.92 ± 0.005*	

14 June: the correlation and regression results on 14 June are very similar to 13 June. The NO_3 data of the butanal oxidation experiment are well correlated (r^2 was between 0.908 and 0.993). Although FZJ-DOAS and ULEIC-BBCRDS data were significantly offset by +22 and −14 pptv, respectively, the slopes of the regression lines (which ranged from 0.89 to 1.09) were still within the combined errors of the instrument pairs. For unknown reasons, the UHD-CEDOAS measurements revealed a change in sensitivity at 10:00 UTC (see Fig. 3, open black squares).

15 June: addition of inorganic aerosol (ammonium sulphate) to the chamber air generally caused a larger variability in the NO_3 data. On 15 June the scatter plots of UAF-CRDS, UCC-IBBCEAS, and ULEIC-BBCRDS showed a common pattern (see, for example, blue and grey circles in Fig. 8). The first addition of aerosol began at the maximum of the NO_3 mixing ratio (10:45 UTC) which then decreased to about 50 pptv when the first particle injection ended (11:25 UTC, cf. Fig. 4). During the injection period the NO_3 values of all instruments correlated well with the NOAA-CRDS mixing ratios. The course of the NO_3 data pairs can be described by "trend lines" with a slope specific for each instrument. After the end of the aerosol injection, however, the pattern changed. The mixing ratios measured during the following 10 to 15 min decreased stronger than expected from the trend observed before. After this "transition period" all following NO_3 mixing ratios measured after 11:40 UTC and during the second aerosol injection (12:30–14:55 UTC) are grouped around different "trend lines" with significantly smaller slopes than in the beginning. Obviously the increasing concentration of aerosol led to the recording of larger inlet losses of NO_3 for some instruments. The UAF-CRDS instrument measured the lowest NO_3 mixing ratios of all instruments on this day. The slope of the linear regression line (comprising the full data set of this day) was 0.86, while the slopes of ULEIC-BBCRDS, UHD-CEDOAS, and FZJ-DOAS showed no large deviation from unity. The FZJ-DOAS instrument was affected by excessive fluctuations of the light source leading to a moderate correlation ($r^2 = 0.707$), an offset of +28 pptv, and a slope of 0.92 (Table 4).

16 and 17 June: the experiment on 16 June was the first to include the in situ production of aerosol inside the

Table 4. Results of the correlation and linear regression analysis of all instruments versus NOAA-CRDS for each experiment. Data are 3 min averages.

Date	Inst.	n	r^2	Intercept/pptv	Slope	$\frac{\chi^2}{(n-2)}$	q	Date	Inst.	n	r^2	Intercept/pptv	Slope	$\frac{\chi^2}{(n-2)}$	q
9 Jun	UCC	89	0.994	−0.4 ± 0.3	1.04 ± 0.003	3.3	a	15 Jun	UCC	113	0.981	−1.1 ± 0.4	1.17 ± 0.007	2.1	a
9 Jun	UAF	87	0.993	−0.5 ± 0.4	1.01 ± 0.004	2.4	a	15 Jun	UAF	108	0.900	−3.0 ± 0.7	0.86 ± 0.011	3.9	a
9 Jun	FZJ	79	0.967	3.1 ± 2.8	0.94 ± 0.034	0.7	0.9809	15 Jun	FZJ	111	0.707	28.0 ± 1.7	0.92 ± 0.028	3.7	a
9 Jun	UHD	17	0.977	1.5 ± 1.5	0.98 ± 0.020	3.1	0.0001	15 Jun	ULEIC	100	0.932	−4.2 ± 0.5	1.05 ± 0.009	7.7	a
10 Jun	UCC	78	0.974	1.5 ± 0.7	1.36 ± 0.007	12.7	a	15 Jun	UHD	55	0.934	−7.4 ± 1.5	1.06 ± 0.025	2.4	a
10 Jun	UAF	92	0.994	0.4 ± 0.8	1.05 ± 0.009	0.8	0.9044	16 Jun	UCC	275	0.959	1.4 ± 0.0	1.17 ± 0.002	253.8	a
10 Jun	FZJ	73	0.930	18.2 ± 1.5	0.90 ± 0.016	4.1	a	16 Jun	UAF	265	0.965	−1.1 ± 0.1	0.91 ± 0.007	2.1	a
10 Jun	ULEIC	29	0.937	−2.3 ± 0.6	0.72 ± 0.008	9.5	a	16 Jun	FZJ	280	0.750	3.6 ± 0.5	1.02 ± 0.029	1.4	a
10 Jun	UHD	57	0.953	1.9 ± 1.4	0.87 ± 0.014	1.7	0.0009	16 Jun	ULEIC	76	0.660	0.4 ± 0.1	0.73 ± 0.006	72.1	a
11 Jun	UCC	124	0.996	2.3 ± 0.5	1.32 ± 0.004	7.9	a	16 Jun	UHD	69	0.590	5.0 ± 0.4	1.02 ± 0.036	5.2	a
11 Jun	UAF	121	0.997	0.3 ± 0.6	0.91 ± 0.005	0.9	0.8531	16 Jun	MPI	51	0.945	−2.8 ± 0.3	1.03 ± 0.015	5.2	a
11 Jun	FZJ	98	0.966	1.2 ± 1.1	1.03 ± 0.010	3.9	a	17 Jun	UCC	329	0.993	1.2 ± 0.0	1.12 ± 0.001	15.7	a
11 Jun	ULEIC	81	0.963	−6.2 ± 0.6	0.90 ± 0.005	8.9	a	17 Jun	UAF	172	0.995	−1.2 ± 0.1	1.12 ± 0.008	0.5	1.0000
11 Jun	UHD	38	0.540	1.3 ± 14.8	0.85 ± 0.158	0.1	1.0000	17 Jun	FZJ	326	0.796	−0.7 ± 0.7	1.14 ± 0.028	1.5	a
12 Jun	UCC	131	0.999	−0.8 ± 0.5	1.10 ± 0.002	1.1	0.1566	18 Jun	UCC	284	0.999	1.8 ± 0.1	1.06 ± 0.003	9.3	a
12 Jun	UAF	107	0.998	−2.3 ± 1.1	1.09 ± 0.009	0.3	1.0000	18 Jun	UAF	275	0.998	−0.9 ± 0.1	0.95 ± 0.006	0.3	1.0000
12 Jun	ULEIC	44	0.994	0.7 ± 0.8	0.97 ± 0.006	5.5	a	18 Jun	FZJ	284	0.925	1.9 ± 0.5	0.98 ± 0.015	1.1	0.0571
12 Jun	UHD	65	0.986	3.8 ± 0.9	0.92 ± 0.006	4.8	a	18 Jun	ULEIC	88	0.997	1.8 ± 0.2	1.02 ± 0.006	39.4	a
13 Jun	UCC	65	0.999	3.6 ± 1.5	1.31 ± 0.004	0.2	1.0000	20 Jun	UCC	127	0.991	1.7 ± 0.7	1.32 ± 0.002	26.5	a
13 Jun	UAF	63	0.998	−1.2 ± 2.0	1.08 ± 0.006	0.6	0.9979	20 Jun	UAF	120	0.983	5.4 ± 0.9	0.84 ± 0.003	9.9	a
13 Jun	FZJ	65	0.997	2.5 ± 1.8	1.05 ± 0.006	1.4	0.0178	20 Jun	FZJ	127	0.994	1.0 ± 1.3	1.01 ± 0.004	1.8	a
13 Jun	ULEIC	62	0.987	2.7 ± 1.7	0.99 ± 0.005	7.4	a	20 Jun	ULEIC	107	0.982	6.1 ± 0.5	0.91 ± 0.001	24.9	a
13 Jun	UHD	30	0.975	−7.7 ± 3.6	1.01 ± 0.011	6.2	a	20 Jun	UHD	66	0.994	4.6 ± 1.8	0.93 ± 0.006	1.6	0.0009
13 Jun	MPI	16	0.998	−0.8 ± 1.6	1.03 ± 0.011	0.2	0.9995	20 Jun	MPI	107	0.974	3.0 ± 0.6	0.93 ± 0.001	3.3	a
14 Jun	UCC	157	0.967	−0.5 ± 0.2	0.96 ± 0.001	17.3	a	21 Jun	UCC	92	0.998	0.1 ± 0.1	1.13 ± 0.002	7.6	a
14 Jun	UAF	145	0.993	1.4 ± 0.7	0.96 ± 0.005	1.0	0.6123	21 Jun	UAF	87	0.991	2.7 ± 0.5	0.86 ± 0.010	0.8	0.8849
14 Jun	FZJ	150	0.908	22.2 ± 1.5	0.90 ± 0.012	2.9	a	21 Jun	FZJ	91	0.966	−1.1 ± 1.0	1.09 ± 0.018	1.2	0.1528
14 Jun	ULEIC	128	0.987	−14.1 ± 0.7	0.99 ± 0.005	2.1	a	21 Jun	ULEIC	30	0.988	−0.8 ± 0.5	1.19 ± 0.013	4.2	a
14 Jun	UHD	85	0.954	7.3 ± 1.1	0.89 ± 0.009	5.1	a	21 Jun	UHD	30	0.914	−2.8 ± 1.7	1.15 ± 0.035	1.7	0.0131
14 Jun	MPI	138	0.979	−3.5 ± 0.8	1.09 ± 0.006	4.4	a	21 Jun	MPI	91	0.991	1.6 ± 0.2	0.97 ± 0.003	5.0	a

q: quality parameter – see text. [a] $q < 10^{-4}$

SAPHIR chamber, in this case secondary organic aerosol (SOA) formed by NO_3 oxidation of limonene (Fry et al., 2011). This experiment resulted in similar observations as made in the inorganic aerosol study on 15 June. During the first oxidation step, at low aerosol concentrations, the data could be described by a line with a different slope than the NO_3 mixing ratios measured after the second injection of limonene (see UCC-IBBCEAS (blue circles) and UAF-CRDS (grey circles) in Fig. 8). The data are still highly correlated ($r^2 = 0.959$ and 0.965, respectively) and the slopes of the regression lines (1.17 and 0.91, respectively) are within the combined uncertainties of the instruments. FZJ-DOAS and UHD-CEDOAS correlate moderately ($r^2 = 0.75$ and 0.59, slopes = 1.02 and 1.02, respectively) due to the low signal-to-noise ratio (relatively small NO_3 mixing ratios were produced by this experiment). ULEIC-BBCRDS and MPI-CRDS stopped measurements already shortly before and after the second limonene injection. Owing to the lack of data from these instruments for high aerosol load the comparison is not particularly meaningful. NOAA-CRDS, UCC-IBBCEAS and FZJ-DOAS continued to record data overnight until 17 June, 19:00 UTC. UAF-CRDS commenced measurements again at 08:00 UTC with a new aerosol filter. For the instruments that were recording on 17 June, the NO_3 mixing ratios correlated very well with NOAA-CRDS, slopes were all ≥ 1.1 and intercepts were negligible (< 1.2 pptv).

18 June: this experiment divides into two phases. As shown in Fig. 4, the NO_3 mixing ratio was smaller than 3 pptv in the morning and less than 12 pptv in the afternoon due reaction with isoprene. Only during a two-hour period, after the addition of extra NO_2 and O_3 at 14:25 UTC, the NO_3 mixing ratio increased to 150 pptv. The comparison of the UAF-CRDS, UCC-IBBCBAS, and ULEIC-BBCRDS instruments with NOAA-CRDS showed coefficients of correlation close to unity during the interval of high NO_3. A slope of 0.95 ($r^2 = 0.998$), 1.06 ($r^2 = 0.999$), and 1.02 ($r^2 = 0.997$) were determined, respectively. The scatter plot of the time intervals of very low NO_3 mixing ratios (08:00–14:00 UTC and 16:30–23:50 UTC) is shown in the inset in Fig. 8. A regression analysis was successfully performed for UCC-IBBCEAS and UAF-CRDS and revealed $r^2 = 0.948$, slope = 1.007, offset = 2.1 pptv and $r^2 = 0.934$, slope = 0.974, offset = −1.0 pptv, respectively. FZJ-DOAS and ULEIC-BBCRDS allowed no meaningful analysis for this time period because the NO_3 mixing ratios were below or close to the detection limit. ULEIC-BBCRDS measured only in the morning when NO_3 merely varied within ±2 pptv, so the regression line is not well defined.

20 and 21 June: the first oxidation experiment of β-pinene with NO_3 was performed in dry air on 20 June. After the

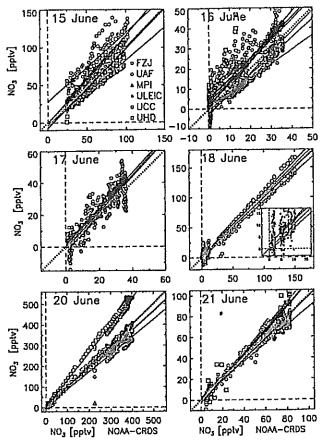

Fig. 8. Continued from Fig. 7. Inset on 18 June: NO_3 mixing ratios in the presence of isoprene (08:00–14:00 UTC (NO_3 < 3 pptv) and 16:10–24:00 UTC (NO_3 < 12 pptv)).

β-pinene injection (09:10 UTC) very rapid formation of SOA was observed (cf. Fig. 4). The excellent precision of the CRDS and CEAS instruments allowed us to visualise an increasing systematic difference in the NO_3 mixing ratios relative to the reference technique. The resulting "u-shaped" scatter plots are presented individually for each instrument by the blue circles in Fig. 6 and compared to each other in the corresponding panel of Fig. 8. This observation is very similar to the experiments on 15 and 16 June described above. The data sets were nevertheless very well ($r^2 = 0.974 \ldots 0.994$) correlated with the reference instrument and the slopes of regression close to unity (FZJ-DOAS) or slightly lower (1.01…0.84) except for UCC-IBBCEAS (see Sect. 3.2). Details are analysed in Sect. 4.4.2.

On 21 June, the previous experiment was repeated at high relative humidity. The correlation and regression results were fairly similar to 20 June. Coefficients of determination (r^2) were close to unity, the intercepts were negligible, and the slopes of FZJ-DOAS, MPI-CRDS, and UAF-CRDS were nearly identical for both days. The UHD-CEDOAS and ULEIC-BBCRDS instruments both slightly overestimated the NO_3 mixing ratio (slopes 1.15 and 1.19, respectively). Again data of FZJ-DOAS correlated linearly with the NOAA reference instrument ($r^2 = 0.966$, slope = 1.0, $q = 0.15$) as well as the data of UAF-CRDS ($r^2 = 0.991$, $q = 0.86$). However, the NO_3 mixing ratios measured by UAF-CRDS were the lowest ones of all instruments on both SOA days (slopes were 0.84 on 20 June, and 0.86 on 21 June).

Unfortunately the measurements stopped before the maximum NO_3 mixing ratio was reached. However, the comparison of the NO_3 mixing ratios above 70 pptv with the linear regression lines of the MPI-CRDS and UAF-CRDS instruments (violet diamonds and grey circles in the last panel of Fig. 8) clearly showed significantly smaller mixing ratios as would be expected from the regression (see also Sect. 4.4.2). This observation resembled the findings of the previous day. The UHD-CEDOAS instruments measured only few NO_3 data points on 21 June because of instrumental tests. ULEIC-BBCRDS stopped measurements on 13:30 UTC, resulting in an also limited data set during the time when the chamber was loaded with aerosol.

4 Discussion

4.1 Uncertainty of the inlet transmission efficiency of the NOAA-CRDS instrument

The transmission efficiency of NOAA-CRDS determined during NO3Comp was 10 % lower than measured in a post-campaign lab study. However, only few calibrations were made during the campaign due to technical difficulties with the calibration source used at the chamber (see Sect. 2.1.1); thus an additional 10 % uncertainty was added by the authors to account for the calibration problems during NO3Comp, resulting in a final accuracy of +0.17/−0.05.

The large data set of the day-to-day correlations of the instruments relative to NOAA-CRDS allows us to apply a statistical test to determine the most likely calibration accuracy of the instrument. The slopes of the linear regressions for clean air and aerosol-containing air are close to unity. A chi-square statistic to the 95 % confidence level (NIST/SEMATECH, 20 May 2012) was used to test the null hypothesis that the true standard deviation of the slopes is less than the specified value of 0.17. From the table of the critical values of the chi-square distribution, the value of $\chi^2_{0.95} = 36.42$ had to be compared to the observed value of $\chi^2_{exp} = 14.25$, and consequently the hypothesis has to be accepted. Equality of both χ^2 values was obtained for a "true" standard deviation of 0.11. Hence, the analysis indicates that the conservatively estimated upper limit of the accuracy of the NOAA-CRDS instrument (0.17) is very likely overestimated by 35 %.

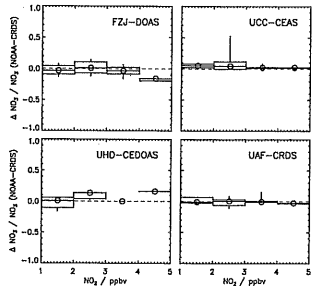

Fig. 9. Box-and-whisker plot of the relative difference of NO_3 measurements between various instruments and the reference NOAA-CRDS as function of the NO_2 mixing ratio during the chamber experiment on 9 June. Dots are medians, boxes give the first and third quartile and whiskers denote the 10th and 90th percentiles.

4.2 Cross sensitivity to NO_2 – experiment on 9 June

Generally, the potential interference of NO_2 on the detection of NO_3 is expected to be minor. The optical absorption coefficient of NO_2 in the spectral range of the NO_3 absorption band is small ($1.27 \times 10^{-4} \times \sigma(NO_3)$). Hence, the resulting interference signal from NO_2 ought to be of minor relevance, unless the NO_2 mixing ratio greatly exceeds that of NO_3. Figure 9 compares the observed differences in NO_3 measurements relative to NOAA-CRDS as a function of NO_2 mixing ratios. NO_3 values below 5 pptv were excluded from this and all following investigations. Circles denote the median, boxes stand for 25 and 75 % percentiles, and vertical lines are the 10th and 90th percentiles of the distribution in the particular interval. A trend could not be identified for any of the data sets. Regression slopes listed in Table 4 are close to unity (0.94 … 1.04) and intercepts are negligible. MPI-CRDS and ULEIC-BBCRDS did not measure on 9 June.

4.3 Cross sensitivity to H_2O – experiment on 10 June

All instruments made use of the strong NO_3 $B \leftarrow X$ absorption transition centred at 662 nm, which partly overlaps with the spectrally much sharper overtone bands of H_2O within the $4\nu + \delta$ polyad centred at 652 nm. The impact of the water absorption on the retrieval of NO_3 mixing ratios was therefore investigated in a clean-air experiment on 10 June. NO_3 was formed in the flushed dry chamber (water mixing ratio < 100 ppmv) and the water mixing ratio was increased in several steps to 1.1 % (Fig. 3). For instruments using the cavity ring-down principle the effect of water vapour absorption on the detection of NO_3 radicals is small, because the contribution of the water vapour absorption is subtracted from the signal by the selective removal of NO_3 in the sample by titration with NO (cf. Eq. 1). The precondition is, however, that the time interval between zero ring-down measurements is smaller than the time it takes for significant changes of water vapour concentration to occur in the sample, which was the case for NO3Comp. Broadband CEAS and CRDS instruments as well as DOAS are potentially more severely affected by water vapour absorption (Aliwell and Jones, 1996; Platt and Stutz, 2008). Usually the spectral resolution of the instruments used for the measurement of atmospheric NO_3 is not sufficiently high to fully resolve the narrow atmospheric absorption lines of water vapour. This can give rise to apparent non-linearity between the optical density measured and the real atmospheric water concentration if not corrected for by appropriate means (see, for instance, Ball and Jones, 2003; Bitter et al., 2005).

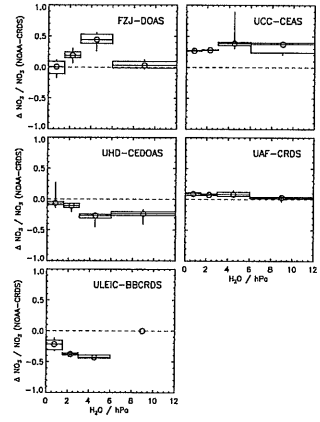

Fig. 10. Box-and-whisker plot of the relative difference of NO_3 measurements between various instruments and the reference NOAA-CRDS as function of the H_2O partial pressure during the chamber experiment on 10 June. Dots are medians, boxes give the first and third quartile and whiskers denote the 10th and 90th percentiles.

In Fig. 10 the relative differences between the instruments and NOAA-CRDS are plotted in intervals of the water vapour partial pressure in the chamber. Only the UHD-CEDOAS instrument was affected by higher water vapour mixing ratios. As can be seen in Fig. 3 (black squares) UHD-CEDOAS and NOAA-CRDS data agreed as long as the chamber air was dry. With the addition of water vapour an increasing difference between the UHD-CEDOAS data and NOAA-CRDS is observed which levels off at higher partial pressures of water. Simultaneously the size of the error bars (not shown) increased from 10 pptv in dry air to some 30 pptv at the final partial pressure of water, which indicates a notable influence of water vapour, at least for this experiment. The deviation of the UHD-CEDOAS instrument can be explained partly by non-linear saturation effects of some water vapour absorption lines which were not treated properly in the retrieval process and partly by insufficient temperature stabilisation of the LED on this day.

FZJ-DOAS, UCC-IBBCEAS, and UAF-CRDS showed no dependency on water vapour. The observed scatter of the FZJ-DOAS ratio in Fig. 10 is attributable to instabilities of the Xe arc lamps causing "jumps" of the DOAS data relative to the very precise NOAA-CRDS instrument. The offset in the UCC-IBBCEAS data resulted from the missing update of the zero air reference spectrum as discussed in Sect. 3.2. The apparent increase of the relative difference of the ULEIC-BBCRDS instrument shown in Fig. 10 is not due to a cross interference by water vapour, but to inhomogeneities in the sample flow (see Sect. 3.2). We want to point out that the NO_2 and water vapour tests were done early in the campaign, so not all the instruments were yet performing optimally.

4.4 Cross sensitivity to aerosol

The comparison of N_2O_5 measurements during NO3Comp by Fuchs et al. (2012) showed that the inlet transmission efficiency for N_2O_5 of some instruments can degrade in the presence of aerosol on which N_2O_5 is taken up. The same observations were described above for NO_3. The aerosol experiments during NO3Comp were divided into three groups: ambient aerosol on 11 June, inorganic (ammonium sulphate, $(NH_4)_2SO_4$) aerosol on 15 and 18 June, and secondary organic aerosol (SOA) on 16, 20, and 21 June. The potential cross sensitivity to aerosol particles was assessed by investigating the changes of the differences of NO_3 mixing ratios measured by the instruments relative to NOAA-CRDS as a function of the aerosol surface concentration. We expected the NOAA-CRDS instrument to be the least affected by wall/inlet losses because of the frequent automatic changing of the inlet filter (versus filter change only once per day for other instruments), and because of the low operating pressure and fast flow rate and therefore minimum residence time of the air inside the instrument. For three experiments the analysis did not lead to statistically significant results.

11 June: on this day ambient air was pumped into the chamber using a filter on the chamber's inlet that removed only coarse-mode particles. The peak aerosol surface concentration, S, in the chamber was very low ($S_{max} = 1.3 \times 10^7$ nm^2 cm^{-3}) and the dynamic range was fairly small ($S_{min} = 0.3 \times 10^7$ nm^2 cm^{-3}). For comparison, during the inorganic aerosol experiment on 15 June S was a factor of 30 larger. An analysis of the relative differences of NO_3 mixing ratios as a function of the aerosol surface concentration showed no discernible dependency of the NO_3 measurements for any instrument.

16 June: the correlation and regression analysis of the limonene oxidation experiment on 16 June already identified (varying) losses of NO_3 inside different instruments and their inlets due to SOA. A corresponding box-and-whisker plot, however, gave no conclusive results because of the small dynamic range of the aerosol surface concentration and the limited SMPS data set.

18 June: a similar result to that on 11 June was obtained for the isoprene/ammonium sulphate seed aerosol experiment on 18 June. During the short time period of high NO_3 mixing ratios, the aerosol surface concentration was relatively low (only about twice the level of the ambient air day) and changed only marginally ($0.3–0.4 \times 10^8$ nm^2 cm^{-3}). Also the regression analysis did not show any evidence of a significant effect of aerosol.

4.4.1 Ammonium sulphate aerosol experiment

On 15 June ammonium sulphate aerosol was added twice to the chamber. The data analysis is presented as a box-and-whisker plot in Fig. 11. NO_3 mixing ratios from FZJ-DOAS were offset relative to NOAA-CRDS by +28 pptv and highly variable, so no trend in FZJ-NOAA difference with aerosol surface area could be quantified. Also for UCC-IBBCEAS and ULEIC-BBCRDS (reduced performance due to variable ingress of ambient air) no clear influence of the increasing aerosol concentration on the detection of NO_3 could be inferred. UHD-CEDOAS showed a slight tendency to an increasing NO_3 deficit at the highest aerosol concentrations, but a clear trend could not be identified. The most pronounced NO_3 loss was found in the UAF-CRDS instrument. This instrument used one single filter per day. NO_3 losses increased with increasing aerosol load on the filter. The loss of NO_3 is illustrated in the box-and-whisker plots in Fig. 11 and in the regression plot of Fig. 8 (grey circles, slope 0.86). Fuchs et al. (2012) reported similar observations for the measurements of N_2O_5 in the presence of ammonium sulphate aerosol during NO3Comp. They showed that N_2O_5 mixing ratios recorded by UAF-CRDS were generally much smaller than those by NOAA-CRDS and concluded that an unaccounted-for NO_3 loss in the inlet of the UAF-CRDS instrument might have been the reason. This hypothesis is consistent with the NO_3 measurements.

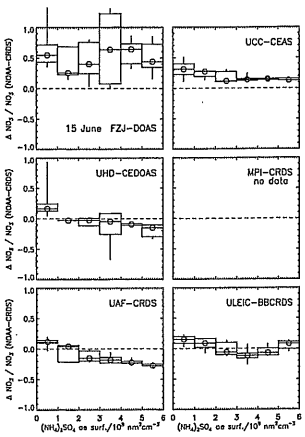

Fig. 11. Box-and-whisker plot of the relative difference of NO_3 measurements between various instruments and the reference NOAA-CRDS as function of the surface of ammonium sulphate aerosol during the "inorganic aerosol" experiment on 15 June. Dots are medians, boxes give the first and third quartile and whiskers denote the 10th and 90th percentiles.

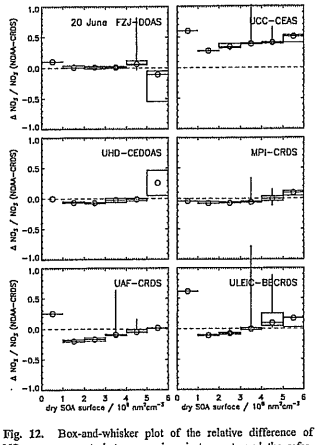

Fig. 12. Box-and-whisker plot of the relative difference of NO_3 measurements between various instruments and the reference NOAA-CRDS as function of the surface of dry secondary organic aerosol (SOA) during the "β-pinene oxidation" experiment on 20 June. Dots are medians, boxes give the first and third quartile and whiskers denote the 10th and 90th percentiles.

4.4.2 Secondary organic aerosol experiments

As shown in Sect. 3.3.3 several instruments clearly detected lower NO_3 mixing ratios than the NOAA-CRDS instrument after secondary organic aerosol was formed in the reaction of β-pinene with NO_3 in dry air on 20 June (cf. Figs. 8 and 6 – blue circles). The box-and-whisker plots in Fig. 12 present the difference of NO_3 mixing ratios relative to NOAA-CRDS as a function of the measured dry SOA surface concentration. Note that in contrast to the experiment on 15 June the aerosol concentration was highest in the beginning of the experiment and decreased towards the end, so that the integrated "aerosol exposure" increases from right to left in Fig. 12. As discussed in Sect. 3.3.3 the DOAS-based techniques FZJ-DOAS and UHD-CEDOAS were mostly unaffected by aerosol. For the remaining instruments (using no or just a single filter per day) a clear trend to lower NO_3 mixing ratios relative to NOAA was evident, which is consistent with the hypothesis that NO_3 is partially removed from sample air as it is drawn through the inlet and filters which are covered with reactive organic aerosol. Fry et al. (2009) investigated the chemistry and the SOA yield for this chamber experiment using a gas-phase kinetics/aerosol partitioning model. They found an unexplained high yield of 6 ppbv of HNO_3 at the end of the dry β-pinene experiment which they attributed to heterogeneous reaction of NO_3 on organic aerosol surfaces, abstracting H from an alkane. This type of reaction could also be responsible for the partial loss of NO_3 in the inlet systems of the instruments. In this context we note that Tang et al. (2010) have shown that filter losses of NO_3 and N_2O_5 can be very variable, with contamination by ambient-aerosol-containing organic compounds strongly favouring NO_3 loss.

A corresponding box-and-whisker analysis could not be performed for the experiment on 21 June which repeated the measurements of the previous day at high relative humidity. Shortly after the maximum aerosol surface concentration was reached, a technical issue caused the SMPS to stop measuring, leaving too few data per bin for a convincing analysis. Fry et al. (2009) showed that both experiments did not significantly differ in terms of reaction mechanism and aerosol yields. However, due to the five-fold higher wall losses of NO_3 (and N_2O_5) at 60 % RH (Fry et al., 2009) but comparable NO_3 production rates for both experiments, the NO_3 (and N_2O_5) mixing ratios were significantly lower on 21 June. Consequently the maximum of the aerosol surface concentration was reached about 45 min later than the dry experiment, and also the formation of HNO_3 was limited to only 2.5 ppbv. However, the temporal profiles of the NO_3 mixing ratios on both days were very similar, showing increasing differences of NO_3 between the instruments towards the end of the measurements (Sect. 3.3.3 and Fig. 4).

So far, it is not understood why the UCC-IBBCEAS instrument, which detected NO_3 in situ in the chamber, showed behaviour on 20 June identical to that of the instruments using inlet lines and aerosol filters. Contrary to UCC-IBBCEAS, both other in situ techniques, FZJ-DOAS and UHD-CEDOAS, were unaffected by aerosol as can be seen in the corresponding panels in Fig. 6 (blue circles). Their NO_3 data scatter uniformly around the regression lines. It is unlikely that the observed effects resulted from a feature of the NOAA-CRDS reference instrument. Filters were exchanged frequently at short time intervals during the aerosol experiments. The fact that the temporal profiles of the NO_3 mixing ratios did not show any discontinuities between filter changes was convincingly verified. This is in contrast to the MPI-CRDS instrument which changed the filter rarely and therefore is more vulnerable to losses of NO_3. An example of NO_3 losses on the surface of a filter is shown in the temporal profile of the NO_3 mixing ratios on 20 June (solid violet diamonds in Fig. 4). At 13:30 UTC, close to the maximum of the NO_3 mixing ratio, the aerosol filter of the MPI-CRDS instrument was exchanged. After restarting the measurements the difference in the NO_3 mixing ratio relative to NOAA-CRDS was considerably smaller than before the filter change.

5 Summary and conclusions

Instruments developed for the detection of tropospheric NO_3 radicals were compared during the "NO3Comp" campaign. Simultaneous measurements of NO_3 radical mixing ratios were conducted by seven instruments under well controlled experimental conditions at the atmosphere simulation chamber SAPHIR in Jülich. All NO_3 instruments assembled at the chamber were based on absorption spectroscopy. Four instruments made use of the principle of cavity ring-down spectroscopy, two utilised cavity-enhanced absorption spectroscopy, and one applied "classical" differential optical absorption spectroscopy. The latter three instruments detected NO_3 in situ in open-path configuration inside the chamber, while the CRDS instruments extracted air from the well-mixed chamber volume. On twelve days in June 2007 chamber studies were performed under a wide variety of chemical conditions. The experiments were designed to compare the instruments under variable concentrations of NO_3, N_2O_5, NO_2, and water vapour, in the presence of inorganic aerosol injected into the chamber or during complex experiments investigating the oxidation of terpenes with NO_3 accompanied by formation of secondary organic aerosol, but also for mixing ratio conditions representative of ambient atmosphere.

Zero air measurements in the clean chamber were used to study the precision of the NO_3 detection. The overall precision of the IBBCEAS and the CRDS instruments varied within 0.5 and 2 pptv; that of the CEDOAS and the DOAS instrument was 5 pptv and 9 pptv, respectively. The instrumental "zero" was also very well defined. The maximum deviation was ±0.2 pptv for the IBBCEAS and the CRDS instruments and +3 pptv and +2 pptv for the CEDOAS and the DOAS instrument, respectively. The sensitivity of the cavity-assisted techniques was very high and permitted the detection of NO_3 radicals with the precision stated above with a time resolution of 1 s (NOAA-CRDS and UAF-CRDS), 5 s (UCC-CEAS), 10 s (MPI-CRDS), 1 min (ULEIC-BBCRDS and FZJ-DOAS), and 5 min (UHD-CEDOAS).

Overall, in situ instruments (FZJ-DOAS, UCC-IBBCEAS, and UHD-CEDOAS) are in very good agreement with instruments sampling air from the chamber volume. The NO_3 data of all instruments are very well linearly correlated with the NOAA-CRDS instrument, which was selected as the common reference to compare the instruments. The median of the coefficient of determination, r^2, for all experiment days (60 correlations) is $r^2 = 0.981$ (1./3. quartile: 0.949/0.994; min/max: 0.540/0.999, cf. Table 4). The linear regression analysis of the corresponding data set yielded very small intercepts (median: 1.1 pptv; Q1/Q3: −1.1/2.6 pptv; min/max: −14.1/22.2 pptv) and the slopes of the regression lines were close to unity (median: 1.01; Q1/Q3: 0.92/1.10; min/max: 0.72/1.36). In any case the deviation of the individual regression slopes from unity was within the combined accuracies of the instrument pairs compared. The variety of NO_3 instruments, their exceptionally high precision and accuracy, the large dynamic range of the NO_3 measurements, and the comprehensive set of NO_3 data acquired under the well controlled homogeneous measurement conditions in the atmosphere simulation chamber allowed the performance of a rigorous statistical data analysis which would not have been possible under less-controlled conditions as, e.g., encountered in field campaigns.

No hint of a cross interference of NO_2 was found for the instruments. The effect of non-Lambert–Beer behaviour of water vapour absorption lines on the accuracy of the NO_3 detection by broadband CEAS and DOAS was found to be small and well accounted for in the data products supplied by the instrument operators.

The loss of NO_3 in the air sampling inlet systems of the instruments which sampled air from the chamber had to be accurately measured. Correction factors under very different chemical conditions were experimentally determined by the participants during NO3Comp and applied for their

respective data retrieval. The very good correspondence between the time-dependent NO_3 mixing ratios measured by all instruments for all aerosol-free experiments indicated that the inlet losses were generally quantified reliably. For experiments with aerosol loading on the inlet systems, however, a marked difference in the loss of NO_3 was noted between instruments using no or just a single aerosol filter per day, and the NOAA-CRDS reference instrument in which the filter was replaced regularly. Differences between NO_3 data were detectable in experiments with added inorganic aerosol or SOA formed during the experiment. The discrepancies increased with time, pointing to accumulating losses due to high aerosol loadings. No difference was found for losses of NO_3 on inorganic or organic aerosol particles. Instruments using DOAS-type analysis showed no significant effect of aerosol on the detection of NO_3.

The NO3Comp campaign demonstrated the high quality, reliability, and robustness of performance of current state-of-the-art instrumentation for NO_3 detection. It was shown that the most significant influence on the performance of instruments was generally caused by the presence of aerosol. Consequently instruments deployed to field measurements concerning NO_3 (and N_2O_5) need to filter the sample air from aerosol particles by Teflon filters close to the head of the sampling line.

The filters should be exchanged frequently; however, there is no general recommendation for the maximum filter "age" because the filter "lifetime" may vary with the aerosol composition and the aerosol mass load in ambient air. The inlet and filter losses are specific for each instrument and hence need to be characterised rigorously and individually for the individual instruments under the different operating conditions in the field.

The NO_3 transmission efficiency due to losses on the filter, in the inlet system, and inside the cavity have to be precisely determined for each instrument. Generally losses to the walls can be minimized by reduction of the residence time of the sample air in the instrument. Fuchs et al. (2008) used sampling lines with 6.4 mm i.d. and reduced the pressure to 350 hPa to establish a residence time of 100 ms between the filter and the centre of the detection cavity. The resulting wall losses of NO_3 were 3 ± 1 %. Together with NO_3 loss on the filter, an overall NO_3 transmission of 92 ± 2 % was achieved.

Due to the strong temperature dependence of the N_2O_5 equilibrium constant (Reaction R5), the difference between the temperature of the ambient air and the (usually higher) temperature inside the NO_3 detection cell should be minimised in order to avoid decomposition to NO_3 especially when the N_2O_5 / NO_3 ratio is large.

The informal NO3Comp intercomparison stimulated the exchange of ideas and methodologies for tropospheric NO_3 and N_2O_5 detection and was very helpful for the further development of these instruments. Their employment on different platforms in the field is ongoing.

Supplementary material related to this article is available online at: http://www.atmos-meas-tech.net/6/1111/2013/amt-6-1111-2013-supplement.pdf.

Acknowledgements. The authors thank Robert Wegener for measurement of butanal concentrations shown in Fig. 3. The NO3Comp campaign was supported by the European-Community-funded Network of Excellence *ACCENT – Atmospheric Composition Change: the European Network* (Grant GOCE-CT-2004-505337) and the FP-6 programme *Support for Research Infrastructures: Integrated Infrastructure Initiative: EUROCHAMP* (Grant RII3-CT-2004-505968). Authors associated with the University of Alaska Fairbanks were supported by the National Science Foundation (Grants CHE- 0094038 and ATM-0624448), as well as by the United States Department of Energy (Grant DE-FG02-03ER83695). The UCC team acknowledges support from the Irish Environmental Protection Agency (Project: TRACES 2005-ET-MS-28-M3). The University of Leicester authors acknowledge support from the Natural Environment Research Council via a PhD studentship for Alex Shillings and a grant (NER/T/S/2002/00036) to develop the BBCRDS instrument.

The service charges for this open access publication have been covered by a Research Centre of the Helmholtz Association.

Edited by: D. Heard

References

Aldener, M., Brown, S. S., Stark, H., Williams, E. J., Lerner, B. M., Kuster, W. C., Goldan, P. D., Quinn, P. K., Bates, T. S., Fehsenfeld, F. C., and Ravishankara, A. R.: Reactivity and loss mechanisms of NO_3 and N_2O_5 in a polluted marine environment: results from in situ measurements during New England Air Quality Study 2002, J. Geophys. Res., 111, D23s73, doi:10.1029/2006jd007252, 2006.

Aliwell, S. R. and Jones, R. L.: Measurement of atmospheric NO_3. 1. Improved removal of water vapour absorption features in the analysis for NO_3, Geophys. Res. Lett., 23, 2585–2588, 1996.

Allan, B. J., McFiggans, G., Plane, J. M. C., Coe, H., and McFadyen, G. G.: The nitrate radical in the remote marine boundary layer, J. Geophys. Res., 105, 24191–24204, 2000.

Ayers, J. D., Apodaca, R. L., Simpson, W. R., and Baer, D. S.: Off-axis cavity ringdown spectroscopy: application to atmospheric nitrate radical detection, Appl. Optics, 44, 7239–7242, 2005.

Ball, S. M. and Jones, R. L.: Broad-band cavity ring-down spectroscopy, Chem. Rev., 103, 5239–5262, 2003.

Ball, S. M. and Jones, A. E.: Broadband cavity ring-down spectroscopy, chap. 3, in: Cavity Ring-Down Spectroscopy: Techniques and Applications, edited by: Berden, G. and Engeln, R., John Wiley & Sons Ltd, Chichester, UK, 57–88, 2009.

Bitter, M., Ball, S. M., Povey, I. M., and Jones, R. L.: A broadband cavity ringdown spectrometer for in-situ measurements of atmospheric trace gases, Atmos. Chem. Phys., 5, 2547–2560, doi:10.5194/acp-5-2547-2005, 2005.

Bossmeyer, J., Brauers, T., Richter, C., Rohrer, F., Wegener, R., and Wahner, A.: Simulation chamber studies on the NO_3 chemistry of atmospheric aldehydes, Geophys. Res. Lett., 33, L18810, doi:10.1029/2006gl026778, 2006.

Brauers, T., Bossmeyer, J., Dorn, H.-P., Schlosser, E., Tillmann, R., Wegener, R., and Wahner, A.: Investigation of the formaldehyde differential absorption cross section at high and low spectral resolution in the simulation chamber SAPHIR, Atmos. Chem. Phys., 7, 3579–3586, doi:10.5194/acp-7-3579-2007, 2007.

Brown, S. S.: Absorption spectroscopy in high-finesse cavities for atmospheric studies, Chem. Rev., 103, 5219–5238, doi:10.1021/cr020645c, 2003.

Brown, S. S. and Stutz, J.: Nighttime radical observations and chemistry, Chem. Soc. Rev., 41, 6405–6447, doi:10.1039/c2cs35181a, 2012.

Brown, S. S., Stark, H., Ciciora, S. J., and Ravishankara, A. R.: In-situ measurement of atmospheric NO_3 and N_2O_5 via cavity ring-down spectroscopy, Geophys. Res. Lett., 28, 3227–3230, 2001.

Brown, S. S., Stark, H., Ciciora, S. J., McLaughlin, R. J., and Ravishankara, A. R.: Simultaneous in situ detection of atmospheric NO_3 and N_2O_5 via cavity ring-down spectroscopy, Rev. Sci. Instrum., 73, 3291–3301, doi:10.1063/1.1499214, 2002a.

Brown, S. S., Stark, H., and Ravishankara, A. R.: Cavity ring-down spectroscopy for atmospheric trace gas detection: application to the nitrate radical (NO_3), Appl. Phys. B, 75, 173–182, doi:10.1007/s00340-002-0980-y, 2002b.

Brown, S. S., Stark, H., Ryerson, T. B., Williams, E. J., Nicks, D. K., Trainer, M., Fehsenfeld, F. C., and Ravishankara, A. R.: Nitrogen oxides in the nocturnal boundary layer: Simultaneous in situ measurements of NO_3, N_2O_5, NO_2, NO, and O_3, J. Geophys. Res., 108, 4299, doi:10.1029/2002jd002917, 2003.

Brown, S. S., Dibb, J. E., Stark, H., Aldener, M., Vozella, M., Whitlow, S., Williams, E. J., Lerner, B. M., Jakoubek, R., Middlebrook, A. M., DeGouw, J. A., Warneke, C., Goldan, P. D., Kuster, W. C., Angevine, W. M., Sueper, D. T., Quinn, P. K., Bates, T. S., Meagher, J. F., Fehsenfeld, F. C., and Ravishankara, A. R.: Nighttime removal of NO_x in the summer marine boundary layer, Geophys. Res. Lett., 31, L07108, doi:10.1029/2004gl019412, 2004.

Brown, S. S., Osthoff, H. D., Stark, H., Dubé, W. P., Ryerson, T. B., Warneke, C., de Gouw, J. A., Wollny, A. G., Parrish, D. D., Fehsenfeld, F. C., and Ravishankara, A. R.: Aircraft observations of daytime NO_3 and N_2O_5 and their implications for tropospheric chemistry, J. Photoch. Photobio. A, 176, 270–278, doi:10.1016/j.jphotochem.2005.10.004, 2005.

Brown, S. S., Neuman, J. A., Ryerson, T. B., Trainer, M., Dubé, W. P., Holloway, J. S., Warneke, C., de Gouw, J. A., Donnelly, S. G., Atlas, E., Matthew, B., Middlebrook, A. M., Peltier, R., Weber, R. J., Stohl, A., Meagher, J. F., Fehsenfeld, F. C., and Ravishankara, A. R.: Nocturnal odd-oxygen budget and its implications for ozone loss in the lower troposphere, Geophys. Res. Lett., 33, L08801, doi:10.1029/2006GL025900, 2006.

Brown, S. S., Dubé, W. P., Osthoff, H. D., Wolfe, D. E., Angevine, W. M., and Ravishankara, A. R.: High resolution vertical distributions of NO_3 and N_2O_5 through the nocturnal boundary layer, Atmos. Chem. Phys., 7, 139–149, doi:10.5194/acp-7-139-2007, 2007.

Canagaratna, M. R., Jayne, J. T., Jimenez, J. L., Allan, J. D., Alfarra, M. R., Zhang, Q., Onasch, T. B., Drewnick, F., Coe, H., Middlebrook, A., Delia, A., Williams, L. R., Trimborn, A. M., Northway, M. J., DeCarlo, P. F., Kolb, C. E., Davidovits, P., and Worsnop, D. R.: Chemical and microphysical characterization of ambient aerosols with the aerodyne aerosol mass spectrometer, Mass Spectrom. Rev., 26, 185–222, doi:10.1002/Mas.20115, 2007.

Chang, W. L., Bhave, P. V., Brown, S. S., Riemer, N., Stutz, J., and Dabdub, D.: Heterogeneous atmospheric chemistry, ambient measurements, and model calculations of N_2O_5: a review, Aerosol Sci. Tech., 45, 665–695, doi:10.1080/02786826.2010.551672, 2011.

Doussin, J.-F., Dominique, R., and Patrick, C.: Multiple-pass cell for very-long-path infrared spectrometry, Appl. Optics, 38, 4145–4150, doi:10.1364/AO.38.004145, 1999.

Dubé, W. P., Brown, S. S., Osthoff, H. D., Nunley, M. R., Ciciora, S. J., Paris, M. W., McLaughlin, R. J., and Ravishankara, A. R.: Aircraft instrument for simultaneous, in situ measurement of NO_3 and N_2O_5 via pulsed cavity ring-down spectroscopy, Rev. Sci. Instrum., 77, 034101, doi:10.1063/1.2176058, 2006.

Efron, B. and Tibshirani, R. J.: An Introduction to the Bootstrap, Chapman and Hall, New York, 1993.

Fiedler, S. E., Hese, A., and Ruth, A. A.: Incoherent broad-band cavity-enhanced absorption spectroscopy, Chem. Phys. Lett., 371, 284–294, doi:10.1016/j.cplett.2003.10.075, 2003.

Fiedler, S. E., Hese, A., and Ruth, A. A.: Incoherent broad-band cavity-enhanced absorption spectroscopy of liquids, Rev. Sci. Instrum., 76, 023107, doi:10.1063/1.1841872, 2005.

Fiedler, S. E., Hese, A., and Heitmann, U.: Influence of the cavity parameters on the output intensity in incoherent broadband cavity-enhanced absorption spectroscopy, Rev. Sci. Instrum., 78, 073104, doi:10.1063/1.2752608, 2007.

Freedman, D. and Diaconis, P.: On the histogram as a density estimator: L_2 theory, Probab. Theory Rel., 57, 453–476, doi:10.1007/bf01025868, 1981.

Fry, J. L., Kiendler-Scharr, A., Rollins, A. W., Wooldridge, P. J., Brown, S. S., Fuchs, H., Dubé, W., Mensah, A., dal Maso, M., Tillmann, R., Dorn, H.-P., Brauers, T., and Cohen, R. C.: Organic nitrate and secondary organic aerosol yield from NO_3 oxidation of β-pinene evaluated using a gas-phase kinetics/aerosol partitioning model, Atmos. Chem. Phys., 9, 1431–1449, doi:10.5194/acp-9-1431-2009, 2009.

Fry, J. L., Kiendler-Scharr, A., Rollins, A. W., Brauers, T., Brown, S. S., Dorn, H.-P., Dubé, W. P., Fuchs, H., Mensah, A., Rohrer, F., Tillmann, R., Wahner, A., Wooldridge, P. J., and Cohen, R. C.: SOA from limonene: role of NO_3 in its generation and degradation, Atmos. Chem. Phys., 11, 3879–3894, doi:10.5194/acp-11-3879-2011, 2011.

Fuchs, H., Dubé, W. P., Ciciora, S. J., and Brown, S. S.: Determination of inlet transmission and conversion efficiencies for in situ measurements of the nocturnal nitrogen oxides, NO_3, N_2O_5 and NO_2, via pulsed cavity ring-down spectroscopy, Anal. Chem., 80, 6010–6017, doi:10.1021/ac8007253, 2008.

Fuchs, H., Ball, S. M., Bohn, B., Brauers, T., Cohen, R. C., Dorn, H.-P., Dubé, W. P., Fry, J. L., Häseler, R., Heitmann, U., Jones, R. L., Kleffmann, J., Mentel, T. F., Mösgen, P., Rohrer, F., Rollins, A. W., Ruth, A. A., Kiendler-Scharr, A., Schlosser, E., Shillings, A. J. L., Tillmann, R., Varma, R. M., Venables, D. S., Villena Tapia, G., Wahner, A., Wegener, R., Wooldridge, P. J., and Brown, S. S.: Intercomparison of measurements of NO_2 concentrations in the atmosphere simulation chamber SAPHIR during the NO3Comp campaign, Atmos. Meas. Tech., 3, 21–37, doi:10.5194/amt-3-21-2010, 2010a.

Fuchs, H., Brauers, T., Dorn, H.-P., Harder, H., Häseler, R., Hofzumahaus, A., Holland, F., Kanaya, Y., Kajii, Y., Kubistin, D., Lou, S., Martinez, M., Miyamoto, K., Nishida, S., Rudolf, M., Schlosser, E., Wahner, A., Yoshino, A., and Schurath, U.: Technical Note: Formal blind intercomparison of HO_2 measurements in the atmosphere simulation chamber SAPHIR during the HOxComp campaign, Atmos. Chem. Phys., 10, 12233–12250, doi:10.5194/acp-10-12233-2010, 2010b.

Fuchs, H., Simpson, W. R., Apodaca, R. L., Brauers, T., Cohen, R. C., Crowley, J. N., Dorn, H.-P., Dubé, W. P., Fry, J. L., Häseler, R., Kajii, Y., Kiendler-Scharr, A., Labazan, I., Matsumoto, J., Mentel, T. F., Nakashima, Y., Rohrer, F., Rollins, A. W., Schuster, G., Tillmann, R., Wahner, A., Wooldridge, P. J., and Brown, S. S.: Comparison of N_2O_5 mixing ratios during NO3Comp 2007 in SAPHIR, Atmos. Meas. Tech., 5, 2763–2777, doi:10.5194/amt-5-2763-2012, 2012.

Geyer, A., Alicke, B., Mihelcic, D., Stutz, J., and Platt, U.: Comparison of tropospheric NO_3 radical measurements by differential optical absorption spectroscopy and matrix isolation electron spin resonance, J. Geophys. Res., 104, 26097–26105, 1999.

Geyer, A., Ackermann, R., Dubois, R., Lohrmann, B., Muller, T., and Platt, U.: Long-term observation of nitrate radicals in the continental boundary layer near Berlin, Atmos. Environ., 35, 3619–3631, doi:10.1016/S1352-2310(00)00549-5, 2001.

Geyer, A., Alicke, B., Ackermann, R., Martinez, M., Harder, H., Brune, W., di Carlo, P., Williams, E., Jobson, T., Hall, S., Shetter, R., and Stutz, J.: Direct observations of daytime NO_3: implications for urban boundary layer chemistry, J. Geophys. Res., 108, 4368, doi:10.1029/2002jd002967, 2003.

Gherman, T., Venables, D. S., Vaughan, S., Orphal, J., and Ruth, A. A.: Incoherent broadband cavity-enhanced absorption spectroscopy in the near-ultraviolet: application to HONO and NO_2, Environ. Sci. Technol., 42, 890–895, doi:10.1021/es0716913, 2008.

Hausmann, M., Brandenburger, U., Brauers, T., and Dorn, H.-P.: Simple Monte Carlo methods to estimate the spectra evaluation error in differential-optical-absorption spectroscopy, Appl. Optics, 38, 462–475, doi:10.1364/AO.38.000462, 1999.

Kasyutich, V. L., Canosa-Mas, C. E., Pfrang, C., Vaughan, S., and Wayne, R. P.: Off-axis continuous-wave cavity-enhanced absorption spectroscopy of narrow-band and broadband absorbers using red diode lasers, Appl. Phys. B, 75, 755–761, 2002.

King, M. D., Dick, B. M., and Simpson, W. R.: A new method for the atmospheric detection of the nitrate radical (NO_3), Atmos. Environ., 34, 685–688, doi:10.1016/S1352-2310(99)00418-5, 2000.

Kraus, S. G.: DOASIS, A Framework Design for DOAS, Dissertation, Institut of Physics, University of Mannheim, Germany, 2006.

Langridge, J. M., Ball, S. M., Shillings, A. J. L., and Jones, R. L.: A broadband absorption spectrometer using light emitting diodes for ultrasensitive, in situ trace gas detection, Rev. Sci. Instrum., 79, 123110, doi:10.1063/1.3046282, 2008a.

Lindinger, W., Hansel, A., and Jordan, A.: On-line monitoring of volatile organic compounds at pptv levels by means of proton-transfer-reaction mass spectrometry (PTR-MS) – medical applications, food control and environmental research, Int. J. Mass Spectrom., 173, 191–241, doi:10.1016/S0168-1176(97)00281-4, 1998.

Matsumoto, J., Kosugi, N., Imai, H., and Kajii, Y.: Development of a measurement system for nitrate radical and dinitrogen pentoxide using a thermal conversion/laser-induced fluorescence technique, Rev. Sci. Instrum., 76, 064101, doi:10.1063/1.1927098, 2005.

McLaren, R., Salmon, R. A., Liggio, J., Hayden, K. L., Anlauf, K. G., and Leaitch, W. R.: Nighttime chemistry at a rural site in the Lower Fraser Valley, Atmos. Environ., 38, 5837–5848, doi:10.1016/j.atmosenv.2004.03.074, 2004.

Meinen, J., Thieser, J., Platt, U., and Leisner, T.: Technical Note: Using a high finesse optical resonator to provide a long light path for differential optical absorption spectroscopy: CE-DOAS, Atmos. Chem. Phys., 10, 3901–3914, doi:10.5194/acp-10-3901-2010, 2010.

Mihelcic, D., Klemp, D., Musgen, P., Patz, H. W., and Volzthomas, A.: Simultaneous measurements of peroxy and nitrate radicals at Schauinsland, J. Atmos. Chem., 16, 313–335, doi:10.1007/BF01032628, 1993.

NIST/SEMATECH: e-Handbook of Statistical Methods, available at: http://www.itl.nist.gov/div898/handbook/, last access: 30 December, 2012.

Orphal, J., Fellows, C. E., and Flaud, P. M.: The visible absorption spectrum of NO_3 measured by high-resolution Fourier transform spectroscopy, J. Geophys. Res., 108, D002489, doi:10.1029/2002JD002489, 2003.

Osthoff, H. D., Brown, S. S., Ryerson, T. B., Fortin, T. J., Lerner, B. M., Williams, E. J., Pettersson, A., Baynard, T., Dubé, W. P., Ciciora, S. J., and Ravishankara, A. R.: Measurement of atmospheric NO_2 by pulsed cavity ring-down spectroscopy, J. Geophys. Res., 111, D12305, doi:10.1029/2005jd006942, 2006.

Osthoff, H. D., Pilling, M. J., Ravishankara, A. R., and Brown, S. S.: Temperature dependence of the NO_3 absorption cross-section above 298 K and determination of the equilibrium constant for $NO_3 + NO_2 \leftrightarrow N_2O_5$ at atmospherically relevant conditions, Phys. Chem. Chem. Phys., 9, 5785–5793, doi:10.1039/B709193a, 2007.

Paul, J. B., Lapson, L., and Anderson, J. G.: Ultrasensitive absorption spectroscopy with a high-finesse optical cavity and off-axis alignment, Appl. Optics, 40, 4904–4910, 2001.

Platt, U. and Perner, D.: Direct measurements of atmospheric CH_2O, HNO_2, O_3, NO_2, and SO_2 by differential optical absorption in the near UV, J. Geophys. Res., 85, 7453–7458, 1980.

Platt, U. and Stutz, J.: Differential Optical Absorption Spectroscopy – Principles and Applications, Physics of Earth and Space Environments, Springer Verlag, Berlin, Heidelberg, 2008.

Platt, U., Perner, D., Winer, A. M., Harris, G. W., and Pitts, J. N.: Detection of NO_3 in the polluted troposphere by differential optical-absorption, Geophys. Res. Lett., 7, 89–92, 1980.

Platt, U., Perner, D., Schroder, J., Kessler, C., and Toennissen, A.: The diurnal-variation of NO_3, J. Geophys. Res., 86, 1965–1970, 1981.

Platt, U., Meinen, J., Pöhler, D., and Leisner, T.: Broadband Cavity Enhanced Differential Optical Absorption Spectroscopy (CE-DOAS) – applicability and corrections, Atmos. Meas. Tech., 2, 713–723, doi:10.5194/amt-2-713-2009, 2009.

Press, W. H., Teukolsky, S. A., Vetterling, W. T., and Flannery, B. P.: Numerical recipies in C. The Art of Scientific Computing, 2nd Edn., Cambridge University Press, Cambridge, UK, 1992.

Rohrer, F., Bohn, B., Brauers, T., Brüning, D., Johnen, F.-J., Wahner, A., and Kleffmann, J.: Characterisation of the photolytic HONO-source in the atmosphere simulation chamber SAPHIR, Atmos. Chem. Phys., 5, 2189–2201, doi:10.5194/acp-5-2189-2005, 2005.

Rollins, A. W., Kiendler-Scharr, A., Fry, J. L., Brauers, T., Brown, S. S., Dorn, H.-P., Dubé, W. P., Fuchs, H., Mensah, A., Mentel, T. F., Rohrer, F., Tillmann, R., Wegener, R., Wooldridge, P. J., and Cohen, R. C.: Isoprene oxidation by nitrate radical: alkyl nitrate and secondary organic aerosol yields, Atmos. Chem. Phys., 9, 6685–6703, doi:10.5194/acp-9-6685-2009, 2009.

Sander, S. P., Abbat, J., Barker, R., Burkholder, J. B., Friedl, R. R., Golden, D. M., Huie, R. E., Kolb, C. E., Kurylo, M. J., Moortgat, G. K., Orkin, V. L., and Wine, P.: Chemical Kinetics and Photochemical Data for Use in Atmospheric Studies, Evaluation Number 17, JPL Publication 10-6, Jet Propulsion Laboratory, Pasadena, 2011.

Schlosser, E., Bohn, B., Brauers, T., Dorn, H.-P., Fuchs, H., Häseler, R., Hofzumahaus, A., Holland, F., Rohrer, F., Rupp, L., Siese, M., Tillmann, R., and Wahner, A.: Intercomparison of two hydroxyl radical measurement techniques at the Atmosphere Simulation Chamber SAPHIR, J. Atmos. Chem., 56, 187–205, doi:10.1007/s10874-006-9049-3, 2007.

Schlosser, E., Brauers, T., Dorn, H.-P., Fuchs, H., Häseler, R., Hofzumahaus, A., Holland, F., Wahner, A., Kanaya, Y., Kajii, Y., Miyamoto, K., Nishida, S., Watanabe, K., Yoshino, A., Kubistin, D., Martinez, M., Rudolf, M., Harder, H., Berresheim, H., Elste, T., Plass-Dülmer, C., Stange, G., and Schurath, U.: Technical Note: Formal blind intercomparison of OH measurements: results from the international campaign HOxComp, Atmos. Chem. Phys., 9, 7923–7948, doi:10.5194/acp-9-7923-2009, 2009.

Schuster, G., Labazan, I., and Crowley, J. N.: A cavity ring down/cavity enhanced absorption device for measurement of ambient NO_3 and N_2O_5, Atmos. Meas. Tech., 2, 1–13, doi:10.5194/amt-2-1-2009, 2009.

Shillings, A. J. L., Ball, S. M., Barber, M. J., Tennyson, J., and Jones, R. L.: An upper limit for water dimer absorption in the 750 nm spectral region and a revised water line list, Atmos. Chem. Phys., 11, 4273–4287, doi:10.5194/acp-11-4273-2011, 2011.

Simpson, W. R.: Continuous wave cavity ring-down spectroscopy applied to in situ detection of dinitrogen pentoxide (N_2O_5), Rev. Sci. Instrum., 74, 3442–3452, 2003.

Sommariva, R., Pilling, M. J., Bloss, W. J., Heard, D. E., Lee, J. D., Fleming, Z. L., Monks, P. S., Plane, J. M. C., Saiz-Lopez, A., Ball, S. M., Bitter, M., Jones, R. L., Brough, N., Penkett, S. A., Hopkins, J. R., Lewis, A. C., and Read, K. A.: Night-time radical chemistry during the NAMBLEX campaign, Atmos. Chem. Phys., 7, 587–598, doi:10.5194/acp-7-587-2007, 2007.

Stutz, J., Alicke, B., Ackermann, R., Geyer, A., White, A., and Williams, E.: Vertical profiles of NO_3, N_2O_5, O_3, and NO_x in the nocturnal boundary layer: 1. Observations during the Texas Air Quality Study 2000, J. Geophys. Res., 109, D12306, doi:10.1029/2003jd004209, 2004.

Tang, M. J., Thieser, J., Schuster, G., and Crowley, J. N.: Uptake of NO_3 and N_2O_5 to Saharan dust, ambient urban aerosol and soot: a relative rate study, Atmos. Chem. Phys., 10, 2965–2974, doi:10.5194/acp-10-2965-2010, 2010.

Triki, M., Cermak, P., Mejean, G., and Romanini, D.: Cavity-enhanced absorption spectroscopy with a red LED source for NO_x trace analysis, Appl. Phys. B, 91, 195–201, doi:10.1007/s00340-008-2958-x, 2008.

Troutman, B. M. and Williams, G. P.: Fitting Straight Lines in the Earth Sciences, Vol. 1, in: Use and Abuse of Statistical Methods in Earth Sciences, edited by: Size, W. B., Oxford University Press, Oxford, 107–128, 1987.

Varma, R. M., Venables, D. S., Ruth, A. A., Heitmann, U., Schlosser, E., and Dixneuf, S.: Long optical cavities for open-path monitoring of atmospheric trace gases and aerosol extinction, Appl. Optics, 48, B159–B171, doi:10.1364/AO.48.00B159, 2009.

Varma, R. M., Ball, S. M., Brauers, T., Dorn, H.-P., Heitmann, U., Jones, R. L., Meinen, J., Platt, U., Pöhler, D., Ruth, A. A., Shillings, J. E., Thieser, J., Wahner, A., and Venables, D. S.: Secondary organic aerosol extinction: an intercomparison of three broadband optical cavity spectrometers, Atmos. Meas. Tech., in preparation, 2013.

Venables, D. S., Gherman, T., Orphal, J., Wenger, J. C., and Ruth, A. A.: High sensitivity in situ monitoring of NO_3 in an atmospheric simulation chamber using incoherent broadband cavity-enhanced absorption spectroscopy, Environ. Sci. Technol., 40, 6758–6763, doi:10.1021/Es061076j, 2006.

Vrekoussis, M., Kanakidou, M., Mihalopoulos, N., Crutzen, P. J., Lelieveld, J., Perner, D., Berresheim, H., and Baboukas, E.: Role of the NO_3 radicals in oxidation processes in the eastern Mediterranean troposphere during the MINOS campaign, Atmos. Chem. Phys., 4, 169–182, doi:10.5194/acp-4-169-2004, 2004.

Vrekoussis, M., Mihalopoulos, N., Gerasopoulos, E., Kanakidou, M., Crutzen, P. J., and Lelieveld, J.: Two-years of NO_3 radical observations in the boundary layer over the Eastern Mediterranean, Atmos. Chem. Phys., 7, 315–327, doi:10.5194/acp-7-315-2007, 2007.

Wängberg, I., Barnes, I., and Becker, K. H.: Product and mechanistic study of the reaction of NO_3 radicals with alpha-pinene, Environ. Sci. Technol., 31, 2130–2135, 1997.

Wayne, R. P., Barnes, I., Biggs, P., Burrows, J. P., Canosamas, C. E., Hjorth, J., Lebras, G., Moortgat, G. K., Perner, D., Poulet, G., Restelli, G., and Sidebottom, H.: The nitrate radical – physics, chemistry, and the atmosphere, Atmos. Environ., 25, 1–203, 1991.

Wegener, R., Brauers, T., Koppmann, R., Rodriguez Bares, S., Rohrer, F., Tillmann, R., Wahner, A., Hansel, A., and Wisthaler, A.: Simulation chamber investigation of the reactions of ozone with short-chained alkenes, J. Geophys. Res., 112, 1–17, doi:10.1029/2006JD007531, 2007.

Wood, E. C., Wooldridge, P. J., Freese, J. H., Albrecht, T., and Cohen, R. C.: Prototype for in situ detection of atmospheric NO_3 and N_2O_5 via laser-induced fluorescence, Environ. Sci. Technol., 37, 5732–5738, doi:10.1021/es034507w, 2003.

Yokelson, R. J., Burkholder, J. B., Fox, R. W., Talukdar, R. K., and Ravishankara, A. R.: Temperature-dependence of the NO_3 absorption-spectrum, J. Phys. Chem., 98, 13144–13150, doi:10.1021/j100101a009, 1994.

CUMULATIVE EXAMINATION IN BIOCHEMISTRY

DEC. 2013

The exam is based on review article by Iain McEwan "Intrinsic disorder in the androgen receptor: identification, characterisation and drugability" [Mol. BioSyst., 2012, 8, 82–90]. The article has been distributed to you prior to the exam and is also part of this exam booklet. Each question requires only brief answer (several sentences).

1. McEwan, p.82: Steroid receptors, such as the AR, are thought to bind to DNA as homodimers and a 15 bp **palindromic** hormone response element (HRE) has been described: 5′-GGAACAnnnTGTTCT-3′. Note that I have slightly modified the original quote for the sake of simplicity. Generally, palindrome is a word or sentence that reads forward the same way as it reads backward (the example of palindrome is the word "radar").

Please deduce what is the meaning of the description "palindromic" in the above quote from McEwan.

2. McEwan, p.82: Steroid receptors, such as the AR, are thought to bind to DNA as **homodimers** and a 15 bp palindromic hormone response element (HRE) has been described: 5′-GGAACAnnnTGTTCT-3′. This is the same simplified quote as in the previous question. The focus is on the fact that AR receptor binds to DNA as a homodimer. There is a cause-effect relationship between the following two facts:

(cause) the DNA response element is palindromic

and

(effect) AR binds to DNA as homodimer.

Please, explain this cause-effect relationship.

3. McEwan p. 84 The AR-NTD is characterized by the presence of several amino acid repeats including two large polymorphic glutamine and glycine stretches of 20 to 23 residues and 16 to 23 residues respectively;

Large content of glycine residue is, in fact, conducive to disorder (such as observed in AR-NTD). Please, explain why.

4. McEwan, p. 85: The AR-NTD/AF1 is proposed to exist as an ensemble of conformations having limited stable structure…

The AR-AF1 domain has 13% helical secondary structure as determined by circular dichroism, FTIR-spectroscopy and secondary structure.

To recapitulate, the AF1 region of AR-NTD exists in a form of dynamic equilibrium where ca. 87% of species are "random" and ca. 13% are "helical" (the two species rapidly interconvert with each other). Please estimate the free energy difference, ΔG, between the "random" and the "helical" form.

To answer this question you will need the value of the ideal gas constant, R=2 cal K^{-1} mol^{-1}.

5. Considering the previous question, please, speculate on what are the major contributions into ΔG.

6. Fig. 2B in McEwan's paper shows a number of phosphorylation sites (indicated by the circles with letter P – see the panel on the right). Most of these phosphorylation sites are found in the disordered regions (blue P circles). This is indeed typical that phosphorylation sites occur in disordered regions. Please explain this observation.

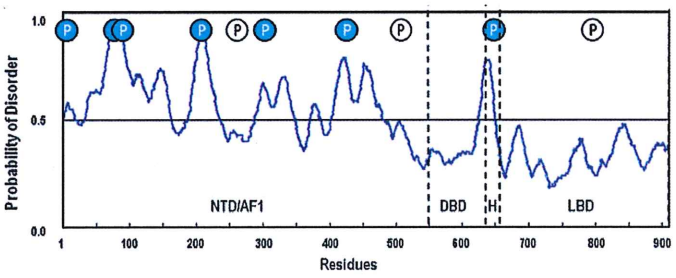

7. McEwan, p. 86 Non-steroidal antiandrogens such as flutamide and bicalutamide bind to the ligand binding pocket in the LBD and prevent agonist binding and impair AR action (Table 1). However, these antagonists can exhibit partial agonist activity as a result of overexpression of the AR protein[64] or point mutations in the LBD that broaden hormone specificity (see[65]).

How do you interpret the last statement (underlined)? Please explain.

8. McEwan p. 88: However, despite the progress made, a number of questions remain unanswered: What is the structure of the full-length or a two-domain AR polypeptide, bound to different DNA response elements?

Why so far no one has been able to obtain such structures at atomic level resolution?

9. McEwan, p. 86: There are three regions within the AR-NTD that show high homology between the receptor from different species, these are amino acids 1 to 25, 224 to 258 and 500 to 541.

What is "high homology"? How to quantitate "high" homology vs. "low" homology vs. the absence of homology?

10. McEwan, p. 87 (Tab 1). The compound TRIAC mechanism of inhibition is Allosteric disruption of AF2 surface. What does this mean (specifically, what is the significance of allosteric mode in this context)? What can be the mechanism of allostery?

View Article Online / Journal Homepage / Table of Contents for this issue
Dynamic Article Links

Molecular BioSystems

Cite this: *Mol. BioSyst.*, 2012, **8**, 82–90

www.rsc.org/molecularbiosystems

REVIEW

Intrinsic disorder in the androgen receptor: identification, characterisation and drugability†

Iain J. McEwan

Received 20th June 2011, Accepted 16th July 2011
DOI: 10.1039/c1mb05249g

Published on 05 August 2011. Downloaded on 01/12/2013 11:28:56.

The androgen receptor (AR) regulates networks of genes in response to the steroid hormones testosterone and dihydrotestosterone. The receptor protein is made up of both stably folded globular domains, involved in hormone and DNA binding, and regions of intrinsic disorder, including the N-terminal domain (NTD). The AR-NTD has a modular activation function (termed AF1) and is important for gene regulation, participating in multiple protein-protein interactions. Biophysical studies have revealed that AR-NTD/AF1 has limited stable secondary structure and conforms to a 'collapsed disordered' conformation. The AR-NTD/AF1 has the propensity to adopt an α-helical conformation in response to a natural osmolyte or a co-regulatory binding partner. The AR is a key drug target in the management of advanced prostate cancer and recently a small molecule inhibitor was identified that interacts with the NTD/AF1 and impairs protein-protein interactions and recruitment of the receptor to target genes. In this review the role of intrinsic disorder in AR function is discussed along with the potential to develop new drugs that will target the structurally plastic NTD.

1. Introduction

"Confusion heard his voice, and wild uproar Stood ruled, stood vast infinitude confined; Till at his second bidding darkness fled, Light shone, and order from disorder sprung."

John Milton, Poet

"However, it required some years before the scientific community in general accepted that flexibility and disorder are very relevant molecular properties also in other systems."

Robert Huber, Biochemist and Nobel Laureate

School of Medical Sciences, University of Aberdeen, IMS Building, Foresterhill, Aberdeen AB25 2ZD, Scotland, UK.
E-mail: iain.mcewan@abden.ac.uk; Tel: + 44 (0)1224 437328
† Published as part of a Molecular BioSystems themed issue on Intrinsically Disordered Proteins: Guest Editor M Madan Babu.

Iain J. McEwan

The steroid hormones testosterone and dihyrdotestosterone are small, four ringed planar molecules that exert profound affects important for the development of the male phenotype during embryogenesis and at puberty.[1] Androgen signalling is also important for reproductive health in both male and females as well as anabolic actions in bone and muscle tissue (see ref. 2, 3 and references therein). The actions of these potent signalling molecules are mediated by the product of a single gene that codes for a protein of 110 kDa: the androgen receptor (AR; NR3C4) is an intracellular protein that functions as a ligand-activated transcription factor (Fig. 1).[4] The AR is a member of the nuclear receptor superfamily, which in addition to steroid receptors includes receptors for vitamins, bile acids and fatty acid derivatives.[5,6] These proteins are highly modular and contain a ligand binding domain (LBD) in the C-terminus, a flexible hinge region linking to the DNA binding domain (DBD) and then a highly variable N-terminal domain (NTD) (Fig. 2A).[6]

2. Androgen receptor organisation

2.1 Ligand binding domain (LBD)

The LBD is built-up of approximately 12 α-helices arranged in three layers forming a sandwiched like structure, with the ligand binding pocket (LBP) buried in the interior.[7–9] The binding of steroid leads to a rearrangement of helix 12 at the C-terminal end of the protein forming a lid over the LBP. The conformational change also creates a surface on the LBD, termed activation function[2] (AF2) that is important for protein-protein interactions with co-regulatory proteins. The AF2 is

This journal is © The Royal Society of Chemistry 2012

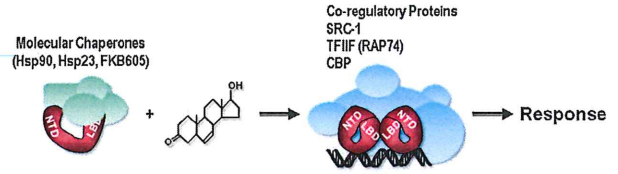

Fig. 1 Androgen Receptor mechanism of Action. In the absence of the hormone the AR is in a complex with molecular chaperones and immunophilin proteins.[79] Binding of testosterone causes a conformational change in the receptor protein, nuclear translocation and binding to target genes. Interactions with the transcriptional machinery and histone modifying enzymes (TFIIF, CBP, SRC1) results in activation of networks of target genes and the cellular response to hormone.

made up of residues from helices 3, 4, 5 and 12 which form a hydrophobic pocket that interacts with FxxLF or the related LxxLL peptide motifs.[7,10] The AF2 surface on the AR-LBD is unique in preferring to interact with the more bulky hydrophobic residues and significantly a FxxLF sequence in the receptor NTD. This N/C-terminal interaction has been shown to be functionally important for selective AR-dependent gene expression. However, interestingly, this N/C terminal interaction may be disrupted by DNA binding, which in turn would expose surfaces within the NTD and the AF2 pocket for interactions with co-regulatory proteins.[11] A second surface on the AR-LBD, termed BF3, has also been described which can bind small molecules (see below) and allosterically regulate protein-protein interactions at AF2.[9]

In other nuclear receptors, for example oestrogen (ER; NR3A1) and retinoid X (RXR; NR2B1) receptors, sequences

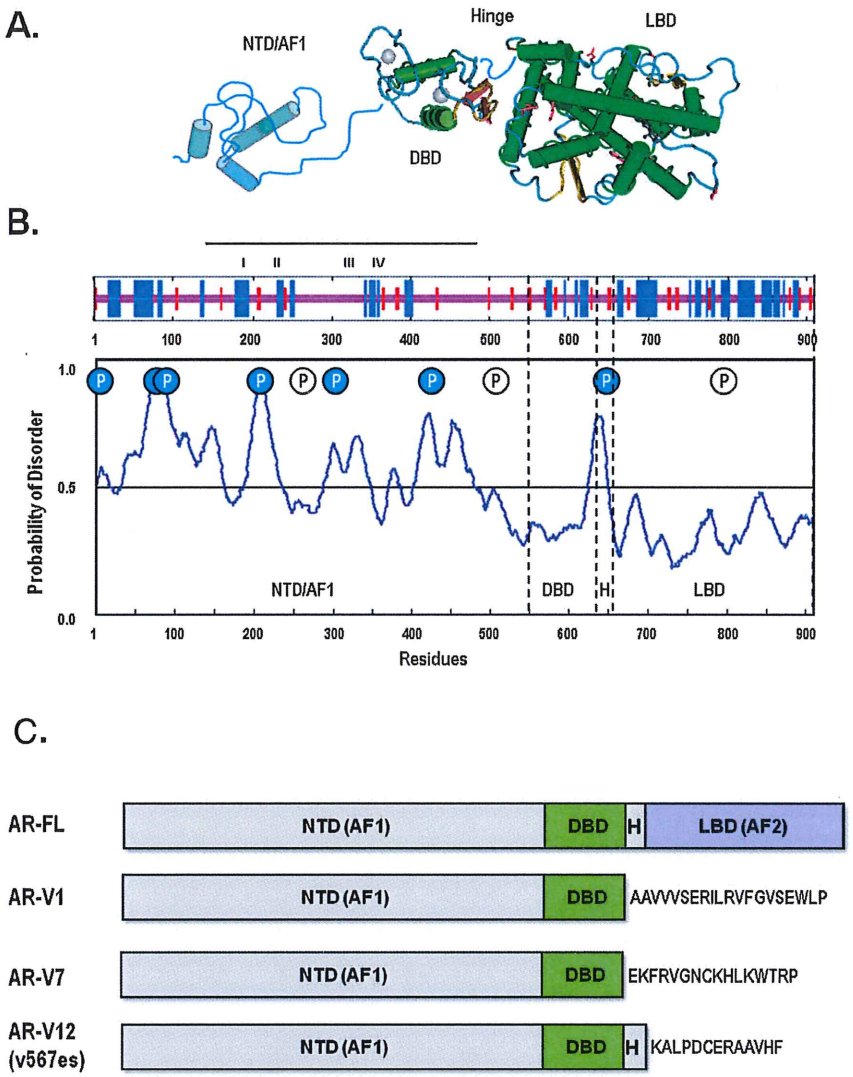

Fig. 2 Domain Organisation and Structure of the Androgen Receptor and Splice Variants. (A) Schematic representation of the AR protein showing the 3-D structure for the isolated ligand (LBD) and DND (DBD) binding domains, together with representation of the structurally flexible hinge and N-terminal domain (NTD). (B) Prediction of secondary structure content in the human AR (upper panel) and regions of intrinsic disorder (RONN plot; lower panel). The Blue and red bars represent α-helix and β-strand structure respectively and the location of four putative helices in AR-AF1 (line, I–IV) are indicated. In the RONN plot peaks represent high probability (> 0.5) of intrinsic disorder. Also shown on this plot is the occurrence of known phosphorylated serine residues: filled circles indicate those residues that are found in regions of intrinsic disorder. (C) Schematic drawing of the full-length AR and representative N-terminal splice variants.

Published on 05 August 2011. Downloaded on 01/12/2013 11:28:56.

Published on 05 August 2011. Downloaded on 01/12/2013 11:28:56.

in helix 10/11 have been shown to represent a dimerization surface. However, whither this is true for the AR is a subject of debate and it is noteworthy that in the crystal structures of the AR-LBD only monomers were observed. A recent comparison of the AR-LBD with the glucocorticoid receptor (GR; NR3C1) sequence and structure identified residues in helices 1, 3 and 5 as a potential dimerization interface.[12] Additional experiments attempting to disrupt potential dimerization interfaces will be required to resolve this question.

2.2 DNA binding domain (DBD)

The DBD consists of approximately 66 amino acids arranged as two Zn-finger-like structures, where the Zn ions are co-ordinated by four cysteine residues. The domain folds into a compact globular structure characterised by two perpendicular α-helices, one of which forms the recognition helix which sits in the major groove of the DNA.[13] Three residues that make up the P-box, Gly^{577}, Ser^{578} and Val^{581}, have been shown to form both direct and water mediate hydrogen bonds with the nucleotides in the DNA binding site.[13] Steroid receptors, such as the AR, are thought to bind to DNA as homodimers and a 15 bp palindromic hormone response element (HRE) has been described: 5′-GGA/TACAnnnTGTTCT-3′. This canonical HRE is also recognised by the GR, progesterone (PR; NR3C3) and mineralocorticoid (MR; NR3C2) receptors.[14] DNA sequences selective for the AR, termed androgen response elements (ARE), have been described, which can be read as a partial palindromic or direct repeat of the 6 bp half site.[15] Recent genome-wide ChIP-chip or ChIP-seq analysis of AR regulated genes in cultured cells or tissues has revealed that receptor binding sites show considerable variation in response element architecture, including imperfect palindromic sequences and half-sites in addition to clearly recognizable AREs.[16–19] From several of these studies the following consensus response element can be determined: 5′-A/GGAACAnnnTGT/GCC/T-3′ (The size of the letter is an approximate representation of the occurrence of each nucleotide at that position; McEwan unpublished). Another feature to emerge from these studies is that hormone binding sites occur within 50 kb of the start site of the target gene and are composite sites with binding sites for other transcription factors, for example FoxA1, GATA2, Oct1, AP1, HNF4α and ETS1.[16–19] However, a number of outstanding questions remain: what roles do other transcription factors and co-regulatory proteins play in the tissue specific expression of AR-regulated genes; and what are the mechanisms that underlie changes in the pattern of AR regulated genes in diseases, such as prostate cancer?

In the second Zn-finger a sequence of five amino acids (Ala^{596}-Ser-Arg-Asn-Asp^{600}) makes up the D-box and represent a dimerization interface between the two receptor monomers.[13] Evidence from work with other steroid receptors suggests that dimerization occurs on the DNA and initial binding involves a receptor monomer. Work with the glucocorticoid receptor also suggests that DNA can act as an allosteric regulator of receptor function, such that binding to different DNA sequences causes changes in surfaces of the DBD that serve as binding sites for co-regulator proteins.[20] Furthermore, binding of the co-regulatory protein JPD2 to the PR-DBD leads to increased helical secondary structure in the receptor NTD.[21] Collectively the evidence suggest that the DBD can have a more active role in regulating receptor function than simply tethering the receptor dimer to DNA.

2.3 N-terminal domain (NTD)

In contrast to the LBD and DBD there is little or no sequence homology between the AR-NTD and the NTD of other steroid, or indeed nuclear, receptor.[4,22,25] The length of the NTD is also highly variable between different family members, with the AR, PR and MR having the largest NTDs. The AR-NTD is characterized by the presence of several amino acid repeats including two large polymorphic glutamine and glycine stretches of 20 to 23 residues and 16 to 23 residues respectively; two shorter glutamine repeats of 5 and 6 residues; and short repeats of 5 alanine and 8 proline residues; and a repeat of the sequence PSTLTL.[22–25] Expansion of the large poly-glutamine repeat is associated with Kennedy's disease or spinal bulbar muscular atrophy a neuromuscular degenerative disease affecting the motor neurones in the brain stem and spinal column (ref. 23 and references therein). There are three regions within the AR-NTD that show high homology between the receptor from different species, these are amino acids 1 to 25, 224 to 258 and 500 to 541, directly adjacent to the DBD.[25]

Earlier work has shown that deletion of the NTD resulted in a transcriptional weak or silent receptor protein.[26,27] And sequences within the NTD have been delineated that are important for receptor-dependent gene regulation and these have been termed collectively activation function 1 (AF1). Brinkmann and co-workers highlighted two regions they termed TAU1 (amino acids 101 to 370) and TAU5 (amino acids 360 to 485), which overlapped with the region identified by Wilson and co-workers (amino acids 141 to 338).[26,27] Significantly, He *et al.*[7] demonstrated using Gal4 fusion constructs, that the length of the NTD correlated with the importance of AF1 for nuclear receptor function.

The first co-regulatory protein identified binding directly to the AF1 region of the AR was the large subunit, RAP74, of the general transcription factor TFIIF.[28] TFIIF is important in the recruitment of RNA polymerase II to the start site of transcription and in regulating the elongation activity of the polymerase. Further work identified receptor binding sites within the globular N- and C-terminal domains of RAP74, which bound AR-AF1 with relative binding affinities of 0.29 μM and 0.69 μM respectively.[24,29] Subsequently an ever growing list of binding partners has been described, including the co-activators SRC-1, CBP and ART27 (reviewed in ref. 30). Collectively, these studies emphasise the importance of regions in the AR-NTD for communicating with the cell's transcriptional machinery. An intriguing question now is whether different surfaces in the AF1 or the AF2 pocket in the LBD mediate differential gene expression. Yamamoto and co-workers[31] identified a number of glucocorticoid-regulated genes that depended selectively on either GR- AF1 or -AF2 surfaces for induction, but this remains to be comprehensively studied for the AR and other steroid receptors.

3. Intrinsic disorder in the AR

3.1 Hinge region

The hinge region is a flexible link between the DBD and the LBD and spans amino acids 624 to 693. The hinge region contains the C-terminal extension (CTE) of the DBD, NLS

This journal is © The Royal Society of Chemistry 2012

Published on 05 August 2011. Downloaded on 01/12/2013 11:28:56.

and sites for post-translational modifications. The CTE has been shown to be important for AR selective response element recognition and binding and appears disordered in structural analysis of the isolated DBD of the AR, glucocorticoid receptor and oestrogen receptors (ref. 13 and references therein). Structural and functional analysis of the NLS showed that the AR NLS interacted with α-importin similar to a monopartite NLS with residues 629 to 634 binding to the armadillo repeats 2, 3 and 4.[32] However, the structure the extended peptide (amino acids 617 to 634) adopted was β-turn-like and unique to the AR NLS.[32]

Interestingly in recent structural studies of full-length nuclear receptors or two-domain receptor constructs different arrangements of the hinge region were observed. In the crystal structure of a complex of PPARγ and RXR bound to a DR1 DNA response element the PPAR monomer adopted a 'closed' conformation with extensive interactions between the LBD and the PPAR-DBD and the RXR-LBD, Hinge and DBD.[33] In contrast the RXR monomer had an 'open' conformation with the hinge region extended and creating a surface for the PPAR binding. The hinge region of the PPAR also made contact with the DNA and contained 2 α-helices, while the RXR hinge region was more flexible and lacked secondary structure.[33] However, these different conformations were not observed in recent solution structure studies of a number of class II receptors, which form heterodimers with RXR, bound to different response elements; although inter domain interactions between the DBD and LBD were observed.[34,35] While these studies lack atomic resolution they generally all show the hinge regions in extended conformations permitting the ordering of the LBDs over the 5′ half-site of the DNA element.[34]

To-date a structure for a full-length, or two domain, steroid receptor complex has not been reported and it will be interesting to see how homodimerisation on palindromic-like response elements affects the architecture of the LBD and hinge region for this class of receptor.

3.2 Structural properties of the NTD

While both the isolated LBD and DBD of the AR exhibit compact α-helical globular structures the NTD lacks stable secondary structure and conforms to the concept of an intrinsically disordered protein domain (Fig. 2B). The AR- AF1 domain has 13% helical secondary structure as determined by circular dichroism, FTIR-spectroscopy and secondary structure prediction analysis.[36,37] Significantly, the AR-AF1 domain has the propensity to form helical structures in the presence of a natural osmolyte, trimethylamine N-oxide (TMAO), or a hydrophobic organic solvent, trifluoroethanol (TFE), or the binding partner TFIIF (RAP74)[36,37] (Fig. 3). In the presence of TMAO or RAP74-CTD there was a 3-fold increase in α-helix secondary structure.[37] TMAO also reduces limited proteolysis of the polypeptide and results in the two tryptophan residues within AF1 becoming less solvent exposed, which is consistent with folding or increased conformational stability of the receptor domain.[38] Four predicted α-helices within AF1 (Fig. 2B, upper panel) were disrupted by introducing helix breaking proline residues.[36] More recently, we could show that AR-AF1 had structural properties

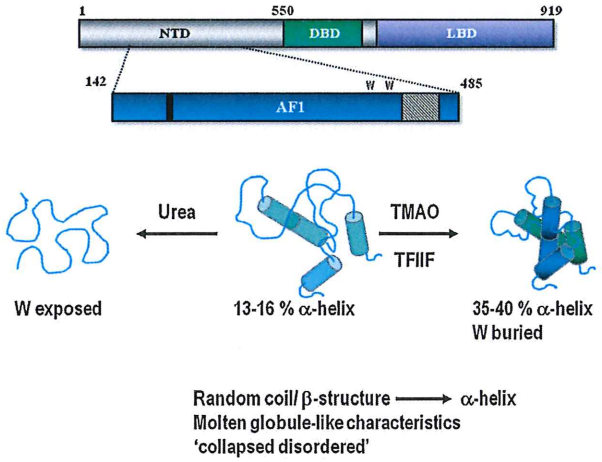

Fig. 3 Regulation of AR-NTD Folding. The AR-NTD/AF1 is proposed to exist as an ensemble of conformations having limited stable structure, described as a 'collapsed disordered' conformation. However, this domain will adopt a more helical conformation in the presence of the natural osmolyte TMAO or a co-regulatory binding protein (*i.e.* TFIIF). Folding or stabilization of the AR-AF1/NTD conformation may also be regulated by DNA binding and post-translational modifications (see text for full discussion).

consistent with a molten-globule like conformation that has been referred to as 'collapsed disorder'.[38] Current models for the AR-AF1 domain suggest that it exists as an ensemble of conformations with limited secondary and tertiary structure, which are primed to bind co-regulatory proteins. Binding of co-regluatory partner proteins, and possibly DNA response elements, stabilises a particular conformation from this ensemble or involves induced folding of the ensemble to a more helical conformation (Fig. 3).

Interestingly the NTD has been found to modulate the DNA binding affinity of the AR-DBD, which was dependent upon the two domains being covalently bound, suggesting intradomain communication.[39] The NTD reduced the binding affinity for a general HRE to a greater degree than AREs and so may act to minimise non-specific interactions of the receptor with DNA.[39] Alternatively, the affect of the NTD on DNA-binding was a consequence of the absence of the LBD and resulted in steric effects that would be countered by the AR-LBD. Further experiments will be needed to resolve these possibilities.

Analysis of the full-length AR-NTD reveals similar structural flexibility and propensity to form helical conformations, suggesting the results for AF1 are not a consequence of using a fragment of the NTD. Deleting the large poly-glutamine repeat within the AR-NTD resulted in a polypeptide with less helical content and more β-structure, which showed a marked reduction in forming α-helical structure in a hydrophobic environment.[23] In contrast the expanded poly-Q repeat from a patient with Kennedy's disease (Q45) showed a modest increase in α-helix and non-ordered structure, but retained the propensity to adopt significant helical conformation at the expense of β-structure and non-ordered structure in the presence of TFE.[23] Collectively these findings suggest that the poly-Q repeat is important for modulating the structural plasticity of the AR-NTD/AF1 domain.

Published on 05 August 2011. Downloaded on 01/12/2013 11:28:56.

It was striking in the recent crystal structure of the PPARγ-RXR complex that the electron density for the receptor NTDs was missing and in hydrogen exchange experiments the highly dynamic nature of these regions was demonstrated.[33] It seems certain therefore that the structural plasticity observed for the AR-AF1/NTD is not simply a consequence of removing the domain from the context of the full-length receptor. However, it is reasonable to expect that other regions of the AR may modulate the folding and/or stability of the AR-AF1/NTD, given the documented intradomain communications of the AR-NTD/LBD and NTD/DBD.

3.3 Post-translational modifications and intrinsically disordered regions of the androgen receptor

The prevalence of intrinsically disordered regions and protein domains in eukayotic signalling proteins and transcription factors has been attributed to the advantages of coupling induced folding with functional interactions[40–42] and allosteric regulation.[43] It has previously been proposed that one advantage of intrinsic disorder is permitting access for post-translational modifying enzymes.[40,42] The AR is the target for a plethora of post-translational modifications, including phosphorylation, acetylation, and sumoylation (see ref. 5 and references therein). A significant number of the residues targeted for different modifications occur in regions of intrinsic disorder: namely the hinge and NTD.

The AR is a phosphoprotein with up to ten phosphorylated serine residues being identified in cell culture systems[44,45]or more recently *in vivo*[2,46,47] Strikingly, 70% of these serine residues are found in regions strongly predicted to be intrinsically disordered (Fig. 2B). One of these residues, serine 650, is found in the hinge domain and has been implicated in cytoplasmic/nuclear shuttling of the AR. In this same region of the receptor lysine residues that make up the NLS have been found to be acetylated[48–51] and more recently methylated.[52,53] These modifications have a complex effect on AR signalling. Acetylation of the lysines in the $K^{630}LKK^{633}$ sequences is important for receptor-dependent gene regulation[48–50] and mutating these residues impirs activation, enhances recruitment of co-repressors,[49] impairs phosphorylation of serine 94 in the NTD[54]and impairs nuclear translocation.[55] Methylation of lysines in this sequence also enhanced receptor-dependent transactivation by increasing N/C-terminal interactions and recruitment of the receptor to target genes.[52,53]

In the case of the ERβ[56] and the GR[57,58] phosphophorylation was associated with conformational changes in the regions of the AF1. Preliminary analysis of the AR-AF1 suggests that phosphorylation may also modulate folding of this domain such that the polypeptide becomes more sensitive to proteolytic challenge when phosphorylated (McEwan and co-workers unpublished data). In this regard it is interesting that inhibition of signalling cascades, impaired kinase activity or mutating phosphorylated residues results in stabilization of the receptor protein (ref. 59; McGuinness and McEwan unpublished observations). The challenge now is to identify specific modifications with domain folding/unfolding and to also indentify the potential signalling cross-talk between different post-translational modifications.

In addition to phosphorylation there are two lysine residues in the AR-NTD, at positions 385 in AF1 and 511, that are modified by sumolyation.[60,61] These lysine residues fall within a sequence that has been termed a 'synergy control' motif, which is found in other steroid receptors (*e g.* GR) and transcriptional factors (*e g.* ETS-1).[62] Mutating the lysines, in particular lysine 385, resulted in increased AR-dependent transcription at multiple HREs,[61,62] but not AREs.[61] The conclusion from such studies is that sumoylation of the AR-NTD mediates control of receptor cooperativity and that the architecture of the DNA binding sites can fine tune this control. The impact if any, of sumoylation on AR-NTD/AF1 folding and conformation remains to be investigated.

4. The androgen receptor as a drug target

Given the prominence of steroid hormones in normal development and physiology the receptor proteins have long been recognised as important and validated drug targets. Hirsutism and acne are conditions resulting from androgen excess and common indicators of polycystic ovarian syndrome (PCOS) while the normal androgen regulation of the prostate gland is hijacked in the growth and progression of prostate cancer. Treatment of these conditions can involve inhibiting production of androgenic steroids by the testis, or ovaries in the case of PCOS, and in the case of advanced prostate cancer using antiandrogens to block AR function.[63]

4.1 LBD

Non-steroidal antiandrogens such as flutamide and bicalutamide bind to the ligand binding pocket in the LBD and prevent agonist binding and impair AR action (Table 1). However, these antagonists can exhibit partial agonist activity as a result of over expression of the AR protein[64] or point mutations in the LBD that broaden hormone specificity (see[65]). More recently, 'second-generation' AR antagonists, such as MDV3100 (Table 1), have been development, which have proved more effective at blocking AR translocation into the nucleus and thereby inhibiting receptor-dependent gene expression.[66,67]

Intriguingly there are an increasing number of compounds, including natural products, which have been described as inhibiting receptor function, such as atraic acid,[68] polyphenols from Green Tea[69] and ligands for thyroid hormone receptor, TRIAC[9] (Table 1). Interestingly, the later along with flufenamic acid (Table 1) was found not to bind in the LBP, but to a discrete surface of the LBD, that was termed BF3. These small molecules were found to inhibit protein-protein interactions at the AF2 surface suggesting allosteric regulation between the two surfaces on the LBD.[9]

4.2 DBD

Although no small molecule inhibitors for the DBD have been described to date Dervan and co-workers[35] demonstrated that polyamide molecules designed to the DNA response element half-site were able to inhibit AR activity and change the pattern of gene expression in prostate cancer cells in culture (Table 1). The polyamide is thought to work by binding to the DNA target sequence and inhibiting protein-DNA interactions.

This journal is © The Royal Society of Chemistry 2012

Published on 05 August 2011. Downloaded on 01/12/2013 11:28:56.

Table 1 Small molecule inhibitors of AR function

Compound	Site of binding	Mechanism of inhibition	Ref.
Hydroxyflutamide 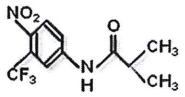	LBD/LBP	Conformational change in hinge region; recruitment of co-repressors.	80
Bicalutamide 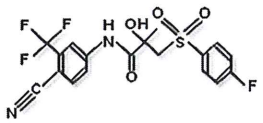	LBD/B-Site	Disruption of AF2 surface; recruitment of co-repressors?	67,81
MDV3100 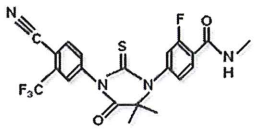	LBD/LBP	Blocks receptor translocation to the nucleus.	66
Atraric Acid 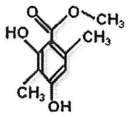	LBD	Blocks receptor translocation to the nucleus.	82
TRIAC 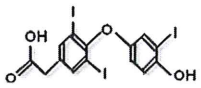	LBD/BF3	Allosteric disruption of AF2 surface.	9
Flufenamic Acid 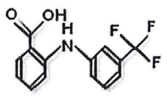	LBD/BF3	Allosteric disruption of AF2 surface.	9
EGCG	LBD/LBP	Disrupts N/C-interaction, increases receptor turnover.	69
Sintokamide A 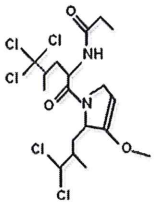	NTD	?	72
EPI-001 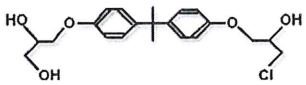	NTD/AF1	Reduces recruitment of the AR to target genes and disrupts protein-protein interactions.	73
Polyamide	—	Binds to androgen response element half-site and inhibition of DNA binding.	83
Pyrvinium (pamoate) 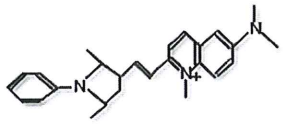	?	Inhibition of protein-protein interactions.	84

Table 1 *(continued)*

Compound	Site of binding	Mechanism of inhibition	Ref.
Harmol (hydrochloride) 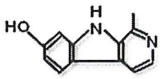	?	Inhibition of DNA binding.	84

EGCG = epigallocatechin-3-gallate (polyphenol found in Green Tea); LBD, DBD and NTD = ligand binding, DNA binding and N-terminal domains of the AR respectively; LBP = ligand binding pocket.; TRIAC = 3,3′,5-triodothyroacetic acid; ? = binding site or mechanism remains to be determined.

Diamond and co-workers[70] have identified several compounds from libraries of compounds and natural products which disrupted the AR-NTD/LBD (CTD) interaction in a ligand screen. The two compounds (Table 1) with highest potency appeared to act at different steps in the receptor signalling pathway: one of the compounds, harmol hydrochloride, acted to inhibit binding of the AR to DNA response elements.[70] However, the binding site for this molecule has not been identified.

4.3 NTD

Until recently the structural plasticity of the NTD may have appeared to be a rather unattractive target for small molecule inhibitors of AR function. However, it is important to remember that this region of the receptor is crucial for function (see above) and using the intact NTD as a 'decoy' molecule Sadar and co-workers could demonstrate it was possible to modulate AR activity by sequestering co-regulatory proteins.[71] This group has also shown that compounds isolated from a marine sponge, sintokamides A to E, which are chlorinated peptides (Table 1), targeted the NTD and inhibited receptor-dependent gene expression.[72] It is therefore of particular significance that a bisphenol A ester derivative (BADGE), isolated from another species of sponge, was identified as a small molecule inhibitor of AR signalling.[73] This molecule, called EPI-001 (Table 1), selectively inhibited the AR-dependent gene regulation in cell culture studies and an impressive ability to shrink tumour volume in two animal models of prostate cancer.[73]

EPI-001 interacted with the NTD/AF1 and altered the steady state fluorescence emission spectrum for AF1 in the tyrosine region and selectively inhibited protein-protein interaction, between the AR and TFIIF (RAP74 subunit) and the coactivator CBP, *in vitro*.[73] Overall this study provides 'proof-of-principle' that small molecule inhibitors can be identified which target the AR-NTD.

Recently a number of splice variants of the AR have been described lacking the LBD, LBD-Hinge or LBD-Hinge-DBD, and the most prevalent ones found in prostate cancer cells have the NTD and DBD (Fig. 2C) and these have the potential to act as constitutive transcriptional activators.[74–78] In particular V7 and V12 appear to be over represented in metastatic clinical samples.[75,77] While most splice variants have been observed as putative transcripts, by RT-PCR, the V1 and V7 have been identified at the protein level.[74–77] It remains to be determined the exact role of these splice variants: do they act as constitutive activators of a subset of androgen regulated genes and/or as modulators of the activity of the full-length receptor? For example V7 and V12 have been shown to be nuclear and have constitutive activity,[74,76] in the receptor negative cell lines PC3 and/or DU145, while V1 was found to be cytoplasmic and had conditional activity[76] in the LNCaP cell line.

The advantages for targeting the NTD therapeutically is that such drugs would complement existing antiandrogens as combined therapies and critically should be effective in castrate resistant prostate cancer (CRPC) where the efficacy of antiandrogens has been compromised through amplification of the AR gene or point mutations in the protein or as result of AR splice variants, which lack the LBD.

5. Conclusions and future perspectives

The cDNA for the human AR was cloned over 20 years ago and the intervening period has seen considerable progress in our understanding of the structure-function relationships of this important ligand-regulated transcription factor and its action in different cell types of the reproductive system. This has included the functional analysis of the isolated receptor domains (NTD, DBD and LBD), the solving at atomic resolution of the structure of the DBD and LBD, the identification of binding partners and a clearer appreciation of the role of intrinsic disorder in receptor-dependent gene regulation. Also recent years has seen a significant increase in the identification of androgen regulated genes and the genomic elements that bind the receptor and the cellular functions of the receptor through targeted knock-out studies. However, despite the progress made, a number of questions remain unanswered:

What is the structure of the full-length or a two-domain AR polypeptide, bound to different DNA response elements?

What conformation(s) does the AR-NTD adopt in response to different binding partners or intracellular conditions?

How are allosteric signals transmitted within or between the different receptor domains; and what role does intrinsic disorder play in this regulation?

How are different post-translational modifications integrated in a cell-specific manner?

How is the AR gene regulated in a temporally and spatially during development and in adult tissues?

In conclusion, it is assured there will be further dramatic developments as researchers strive to understand the biology and physiological actions of the androgen receptor, the structural and biochemical basis for receptor function and the impact genetic alterations have on receptor-dependent diseases such as prostate cancer.

Published on 05 August 2011. Downloaded on 01/12/2013 11:28:56.

 This journal is © The Royal Society of Chemistry 2012

View Article Online

Acknowledgements

Research in the author's laboratory is currently supported by the Chief Scientists Office, Scottish Government; The Kosterlizt centre, University of Aberdeen; and the Prostate Cancer Charity.

References

1 M. T. Patrao, E. J. Silva and M. C. Avellar, *Arq. Bras. Endocrinol. Metabol.*, 2009, **53**, 934–945.
2 I. J. McEwan, D. McGuinness, C. W. Hay, R. P. Millar, P. T. Saunders and H. M. Fraser, *Reproduction*, 2010, **140**, 93–104.
3 S. C. Manolagas, S. Kousteni and R. L. Jilka, *Recent Prog. Horm. Res.*, 2002, **57**, 385–409.
4 J. McEwan, *Endocr. Relat. Cancer*, 2004, **11**, 281–293.
5 I. J. McEwan, *Essays Biochem.*, 2004, **40**, 1–10.
6 I. J. McEwan, *Methods Mol. Biol.*, 2009, **505**, 3–18.
7 B. He, R. T. Gampe Jr, A. J. Kole, A. T. Hnat, T. B. Stanley, G. An, E. L. Stewart, R. I. Kalman, J. T. Minges and E. M. Wilson, *Mol. Cell*, 2004, **16**, 425–438.
8 P. M. Matias, P. Donner, R. Coelho, M. Thomaz, C. Peixoto, S. Macedo, N. Otto, S. Joschko, P. Scholz, A. Wegg, S. Basler, M. Schafer, U. Egner and M. A. Carrondo, *J. Biol. Chem.*, 2000, **275**, 26164–26171.
9 E. Estebanez-Perpina, L. A. Arnold, P. Nguyen, E. D. Rodrigues, E. Mar, R. Bateman, P. Pallai, K. M. Shokat, J. D. Baxter, R. K. Guy, P. Webb and R. J. Fletterick, *Proc. Natl. Acad. Sci. U. S. A.*, 2007, **104**, 16074–16079.
10 H. J. Dubbink, R. Hersmus, C. S. Verma, H. A. van der Korput, C. A. Berrevoets, J. van Tol, A. C. Ziel-van der Made, A. O. Brinkmann, A. C. Pike and J. Trapman, *Mol. Endocrinol.*, 2004, **18**, 2132–2150.
11 M. E. van Royen, S. M. Cunha, M. C. Brink, K. A. Mattern, A. L. Nigg, H. J. Dubbink, P. J. Verschure, J. Trapman and A. B. Houtsmuller, *J. Cell Biol.*, 2007, **177**, 63–72.
12 M. M. Centenera, J. M. Harris, W. D. Tilley and L. M. Butler, *Mol. Endocrinol.*, 2008, **22**, 2373–2382.
13 P. L. Shaffer, A. Jivan, D. E. Dollins, F. Claessens and D. T. Gewirth, *Proc. Natl. Acad. Sci. U. S. A.*, 2004, **101**, 4758–4763.
14 F. Claessens and D. T. Gewirth, *Essays Biochem.*, 2004, **40**, 59–72.
15 E. Schoenmakers, G. Verrijdt, B. Peeters, G. Verhoeven, W. Rombauts and F. Claessens, *J. Biol. Chem.*, 2000, **275**, 12290–12297.
16 E. C. Bolton, A. Y. So, C. Chaivorapol, C. M. Haqq, H. Li and K. R. Yamamoto, *Genes Dev.*, 2007, **21**, 2005–2017.
17 S. M. Eacker, J. E. Shima, C. M. Connolly, M. Sharma, R. W. Holdcraft, M. D. Griswold and R. E. Braun, *Mol. Endocrinol.*, 2007, **21**, 895–907.
18 C. E. Massie, B. Adryan, N. L. Barbosa-Morais, A. G. Lynch, M. G. Tran, D. E. Neal and I. G. Mills, *EMBO Rep.*, 2007, **8**, 871–878.
19 Q. Wang, W. Li, X. S. Liu, J. S. Carroll, O. A. Janne, E. K. Keeton, A. M. Chinnaiyan, K. J. Pienta and M. Brown, *Mol. Cell*, 2007, **27**, 380–392.
20 S. H. Meijsing, M. A. Pufall, A. Y. So, D. L. Bates, L. Chen and K. R. Yamamoto, *Science*, 2009, **324**, 407–410.
21 S. E. Wardell, S. C. Kwok, L. Sherman, R. S. Hodges and D. P. Edwards, *Mol. Cell. Biol.*, 2005, **25**, 8792–8808.
22 C. S. Choong, J. A. Kemppainen and E. M. Wilson, *J. Mol. Evol.*, 1998, **47**, 334–342.
23 P. Davies, K. Watt, S. M. Kelly, C. Clark, N. C. Price and I. J. McEwan, *J. Mol. Endocrinol.*, 2008, **41**, 301–314.
24 J. Reid, I. Murray, K. Watt, R. Betney and I. J. McEwan, *J. Biol. Chem.*, 2002, **277**, 41247–41253.
25 R. Betney and I. J. McEwan, *J. Mol. Endocrinol.*, 2003, **31**, 427–439.
26 J. A. Simental, M. Sar, M. V. Lane, F. S. French and E. M. Wilson, *J. Biol. Chem.*, 1991, **266**, 510–518.
27 G. Jenster, H. A. van der Korput, J. Trapman and A. O. Brinkmann, *J. Biol. Chem.*, 1995, **270**, 7341–7346.
28 I. J. McEwan and J. Gustafsson, *Proc. Natl. Acad. Sci. U. S. A.*, 1997, **94**, 8485–8490.
29 D. N. Lavery and I. J. McEwan, *Biochemistry*, 2008, **47**, 3352–3359.
30 D. N. Lavery and I. J. McEwan, *Biochem. J.*, 2005, **391**, 449–464.
31 I. Rogatsky, J. C. Wang, M. K. Derynck, D. F. Nonaka, D. B. Khodabakhsh, C. M. Haqq, B. D. Darimont, M. J. Garabedian and K. R. Yamamoto, *Proc. Natl. Acad. Sci. U. S. A.*, 2003, **100**, 13845–13850.
32 M. L. Cutress, H. C. Whitaker, I. G. Mills, M. Stewart and D. E. Neal, *J. Cell Sci.*, 2008, **121**, 957–968.
33 V. Chandra, P. Huang, Y. Hamuro, S. Raghuram, Y. Wang, T. P. Burris and F. Rastinejad, *Nature*, 2008, **456**, 350–356.
34 N. Rochel, F. Ciesielski, J. Godet, E. Moman, M. Roessle, C. Peluso-Iltis, M. Moulin, M. Haertlein, P. Callow, Y. Mely, D. I. Svergun and D. Moras, *Nat. Struct. Mol. Biol.*, 2011, **18**, 564–570.
35 J. Zhang, M. J. Chalmers, K. R. Stayrook, L. L. Burris, Y. Wang, S. A. Busby, B. D. Pascal, R. D. Garcia-Ordonez, J. B. Bruning, M. A. Istrate, D. J. Kojetin, J. A. Dodge, T. P. Burris and P. R. Griffin, *Nat. Struct. Mol. Biol.*, 2011, **18**, 556–563.
36 J. Reid, S. M. Kelly, K. Watt, N. C. Price and I. J. McEwan, *J. Biol. Chem.*, 2002, **277**, 20079–20086.
37 R. Kumar, R. Betney, J. Li, E. B. Thompson and I. J. McEwan, *Biochemistry*, 2004, **43**, 3008–3013.
38 D. N. Lavery and I. J. McEwan, *Biochemistry*, 2008, **47**, 3360–3369, DOI: 10.1021/bi702221e.
39 J. Brodie and I. J. McEwan, *J. Mol. Endocrinol.*, 2005, **34**, 603–615, DOI: 10.1677/jme.1.01723.
40 H. J. Dyson and P. E. Wright, *Nat. Rev. Mol. Cell Biol.*, 2005, **6**, 197–208, DOI: 10.1038/nrm1589.
41 P. Tompa, *FEBS Lett.*, 2005, **579**, 3346–3354, DOI: 10.1016/j.febslet.2005.03.072.
42 J. Liu, N. B. Perumal, C. J. Oldfield, E. W. Su, V. N. Uversky and A. K. Dunker, *Biochemistry*, 2006, **45**, 6873–6888, DOI: 10.1021/bi0602718.
43 V. J. Hilser and E. B. Thompson, *Proc. Natl. Acad. Sci. U. S. A.*, 2007, **104**, 8311–8315, DOI: 10.1073/pnas.0700329104.
44 D. Gioeli, S. B. Ficarro, J. J. Kwiek, D. Aaronson, M. Hancock, A. D. Catling, F. M. White, R. E. Christian, R. E. Settlage, J. Shabanowitz, D. F. Hunt and M. J. Weber, *J. Biol. Chem.*, 2002, **277**, 29304–29314.
45 L. A. Ponguta, C. W. Gregory, F. S. French and E. M. Wilson, *J. Biol. Chem.*, 2008, **283**, 20989–21001.
46 S. S. Taneja, S. Ha, N. K. Swenson, H. Y. Huang, P. Lee, J. Melamed, E. Shapiro, M. J. Garabedian and S. K. Logan, *J. Biol. Chem.*, 2005, **280**, 40916–40924.
47 P. McCall, L. K. Gemmell, R. Mukherjee, J. M. Bartlett and J. Edwards, *Br. J. Cancer*, 2008, **98**, 1094–1101.
48 M. Fu, C. Wang, A. T. Reutens, J. Wang, R. H. Angeletti, L. Siconolfi-Baez, V. Ogryzko, M. L. Avantaggiati and R. G. Pestell, *J. Biol. Chem.*, 2000, **275**, 20853–20860.
49 M. Fu, C. Wang, J. Wang, X. Zhang, T. Sakamaki, Y. G. Yeung, C. Chang, T. Hopp, S. A. Fuqua, E. Jaffray, R. T. Hay, J. J. Palvimo, O. A. Janne and R. G. Pestell, *Mol. Cell. Biol.*, 2002, **22**, 3373–3388.
50 L. Gaughan, I. R. Logan, S. Cook, D. E. Neal and C. N. Robson, *J. Biol. Chem.*, 2002, **277**, 25904–25913.
51 M. Fu, M. Rao, C. Wang, T. Sakamaki, J. Wang, D. Di Vizio, X. Zhang, C. Albanese, S. Balk, C. Chang, S. Fan, E. Rosen, J. J. Palvimo, O. A. Janne, S. Muratoglu, M. L. Avantaggiati and R. G. Pestell, *Mol. Cell. Biol.*, 2003, **23**, 8563–8575.
52 L. Gaughan, J. Stockley, N. Wang, S. R. McCracken, A. Treumann, K. Armstrong, F. Shaheen, K. Watt, I. J. McEwan, C. Wang, R. G. Pestell and C. N. Robson, *Nucleic Acids Res.*, 2011, **39**, 1266–1279.
53 S. Ko, J. Ahn, C. S. Song, S. Kim, K. Knapczyk-Stwora and B. Chatterjee, *Mol. Endocrinol.*, 2011, **25**, 433–444.
54 M. Fu, M. Rao, K. Wu, C. Wang, X. Zhang, M. Hessien, Y. G. Yeung, D. Gioeli, M. J. Weber and R. G. Pestell, *J. Biol. Chem.*, 2004, **279**, 29436–29449.
55 M. Thomas, N. Dadgar, A. Aphale, J. M. Harrell, R. Kunkel, W. B. Pratt and A. P. Lieberman, *J. Biol. Chem.*, 2004, **279**, 8389–8395.
56 Y. X. Chen, J. T. Du, L. X. Zhou, X. H. Liu, Y. F. Zhao, H. Nakanishi and Y. M. Li, *Chem. Biol.*, 2006, **13**, 937–944.

Published on 05 August 2011. Downloaded on 01/12/2013 11:28:56.

View Article Online

57 W. Chen, T. Dang, R. D. Blind, Z. Wang, C. N. Cavasotto, A. B. Hittelman, I. Rogatsky, S. K. Logan and M. J. Garabedian, *Mol. Endocrinol.*, 2008, **22**, 1754–1766.
58 A. M. Garza, S. H. Khan and R. Kumar, *Mol. Cell. Biol.*, 2010, **30**, 220–230.
59 P. Chymkowitch, N. Le May, P. Charneau, E. Compe and J. M. Egly, *EMBO J.*, 2011, **30**, 468–479.
60 H. Poukka, U. Karvonen, O. A. Janne and J. J. Palvimo, *Proc. Natl. Acad. Sci. U. S. A.*, 2000, **97**, 14145–14150.
61 L. Callewaert, G. Verrijdt, A. Haelens and F. Claessens, *Mol. Endocrinol.*, 2004, **18**, 1438–1449.
62 J. A. Iniguez-Lluhi and D. Pearce, *Mol. Cell. Biol.*, 2000, **20**, 6040–6050.
63 S. S. Dutt and A. C. Gao, *Future Oncol.*, 2009, **5**, 1403–1413.
64 C. D. Chen, D. S. Welsbie, C. Tran, S. H. Baek, R. Chen, R. Vessella, M. G. Rosenfeld and C. L. Sawyers, *Nat. Med.*, 2004, **10**, 33–39.
65 J. Duff and I. J. McEwan, *Mol. Endocrinol.*, 2005, **19**, 2943–2954.
66 C. Tran, S. Ouk, N. J. Clegg, Y. Chen, P. A. Watson, V. Arora, J. Wongvipat, P. M. Smith-Jones, D. Yoo, A. Kwon, T. Wasielewska, D. Welsbie, C. D. Chen, C. S. Higano, T. M. Beer, D. T. Hung, H. I. Scher, M. E. Jung and C. L. Sawyers, *Science*, 2009, **324**, 787–790.
67 H. C. Shen and S. P. Balk, *Cancer Cell*, 2009, **15**, 461–463.
68 D. Roell and A. Baniahmad, *Mol. Cell. Endocrinol.*, 2011, **332**, 1–8.
69 I. A. Siddiqui, M. Asim, B. B. Hafeez, V. M. Adhami, R. S. Tarapore and H. Mukhtar, *FASEB J.*, 2011, **25**, 1198–1207.
70 J. O. Jones and M. I. Diamond, *ACS Chem. Biol.*, 2008, **3**, 412–418.
71 S. N. Quayle, N. R. Mawji, J. Wang and M. D. Sadar, *Proc. Natl. Acad. Sci. U. S. A.*, 2007, **104**, 1331–1336.
72 M. D. Sadar, D. E. Williams, N. R. Mawji, B. O. Patrick, T. Wikanta, E. Chasanah, H. E. Irianto, R. V. Soest and R. J. Andersen, *Org. Lett.*, 2008, **10**, 4947–4950.
73 R. J. Andersen, N. R. Mawji, J. Wang, G. Wang, S. Haile, J. K. Myung, K. Watt, T. Tam, Y. C. Yang, C. A. Banuelos, D. E. Williams, I. J. McEwan, Y. Wang and M. D. Sadar, *Cancer Cell*, 2010, **17**, 535–546.
74 P. A. Watson, Y. F. Chen, M. D. Balbas, J. Wongvipat, N. D. Socci, A. Viale, K. Kim and C. L. Sawyers, *Proc. Natl. Acad. Sci. U. S. A.*, 2010, **107**, 16759–16765.
75 S. Sun, C. C. Sprenger, R. L. Vessella, K. Haugk, K. Soriano, E. A. Mostaghel, S. T. Page, I. M. Coleman, H. M. Nguyen, H. Sun, P. S. Nelson and S. R. Plymate, *J. Clin. Invest.*, 2010, **120**, 2715–2730.
76 R. Hu, W. B. Isaacs and J. Luo, *Prostate*, 2011, DOI: 10.1002/pros.21382; 10.1002/pros.21382.
77 E. Hornberg, E. B. Ylitalo, S. Crnalic, H. Antti, P. Stattin, A. Widmark, A. Bergh and P. Wikstrom, *PLoS One*, 2011, **6**, e19059.
78 S. M. Dehm, L. J. Schmidt, H. V. Heemers, R. L. Vessella and D. J. Tindall, *Cancer Res.*, 2008, **68**, 5469–5477.
79 L. Ni, C. S. Yang, D. Gioeli, H. Frierson, D. O. Toft and B. M. Paschal, *Mol. Cell. Biol.*, 2010, **30**, 1243–1253.
80 C. W. Kuil and E. Mulder, *Mol. Cell. Endocrinol.*, 1994, **102**, R1–5.
81 D. J. Osguthorpe and A. T. Hagler, *Biochemistry*, 2011, **50**, 4105–4113.
82 M. Papaioannou, S. Schleich, D. Roell, U. Schubert, T. Tanner, F. Claessens, R. Matusch and A. Baniahmad, *Invest. New Drugs*, 2010, **28**, 729–743.
83 N. G. Nickols and P. B. Dervan, *Proc. Natl. Acad. Sci. U. S. A.*, 2007, **104**, 10418–10423.
84 J. O. Jones, E. C. Bolton, Y. Huang, C. Feau, R. K. Guy, K. R. Yamamoto, B. Hann and M. I. Diamond, *Proc. Natl. Acad. Sci. U. S. A.*, 2009, **106**, 7233–7238.

Published on 05 August 2011. Downloaded on 01/12/2013 11:28:56.

This journal is © The Royal Society of Chemistry 2012

Cumulative Exam – Inorganic Chemistry

Organometallic Reaction Mechanism

1. Hartwig has studied the oxidative addition of haloarenes to a bisphosphine palladium complex and observed different kinetic dependences on the reaction components depending on the identity of the halide. **For each halide (X = Cl, Br, I), provide a succinct summary of what can be concluded from the experimental data and propose a mechanism that is consistent with all of the data.**

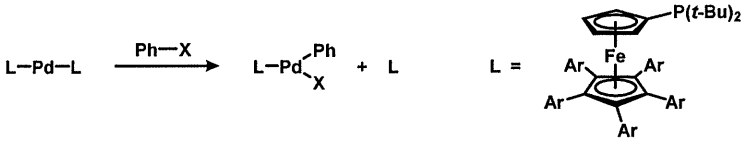

(a) For X = Cl, the following data were obtained:

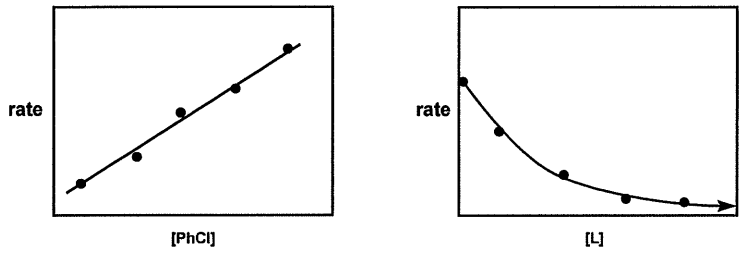

(b) For X = Br, the following data were obtained:

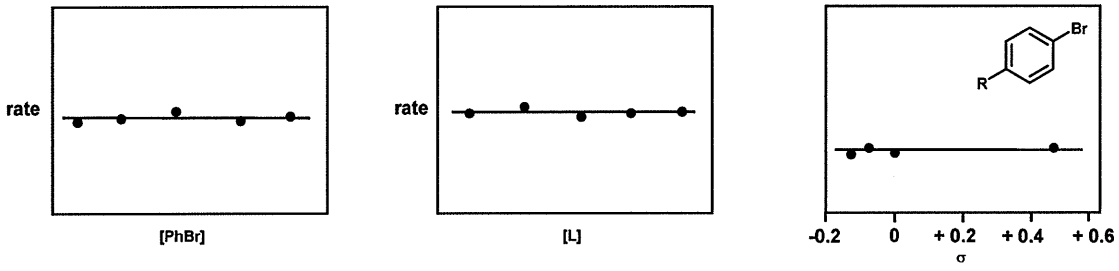

(c) For X = I, the following data were obtained:

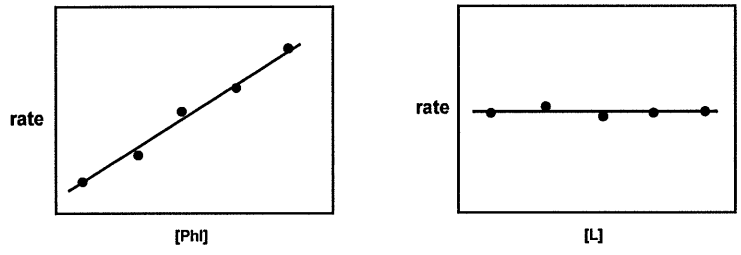

2. Echavarren has studied the palladium-catalyzed intramolecular arylation of **1** to form **2**. Two distinct mechanisms for the key aryl-Pd bond-forming step were proposed: (a) electrophilic aromatic substitution and (b) σ-bond metathesis.

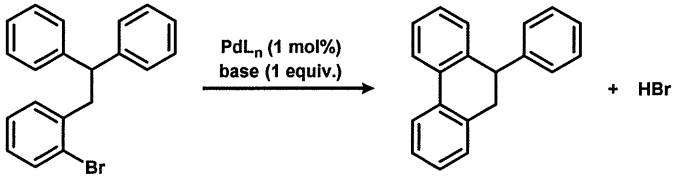

1 **2**

(a) Write out a complete catalytic cycle for the aromatic substitution pathway.

(b) Write out a complete catalytic cycle for the σ-bond metathesis pathway.

(c) Assuming that the key aryl-Pd bond-forming step is rate-limiting in each case, propose two fundamentally different experiments that would allow you to distinguish between mechanisms (a) and (b) above.

Organic Cumulative Examination – Heterocyclic Synthesis from Org. Lett. 2013 –Dec. 7, 2013

Propose stepwise mechanisms to explain **4** of the **7** following transformations. Use curved arrow formalism to show electron movement and show <u>all</u> likely intermediates.

1.

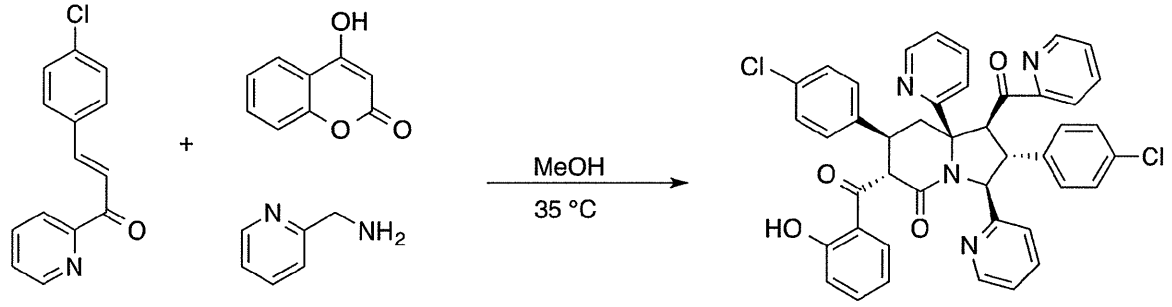

2.

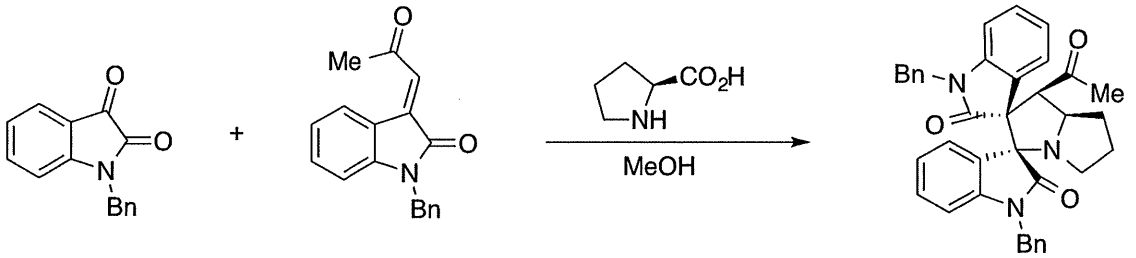

3.

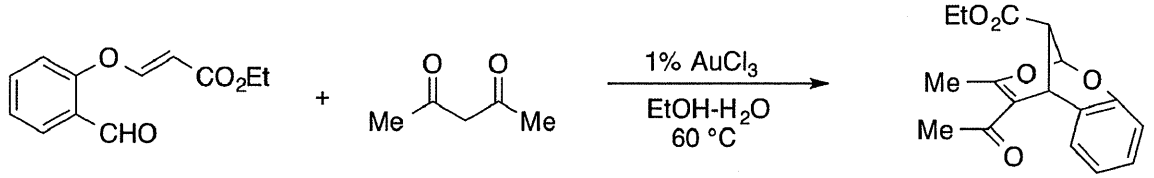

4.

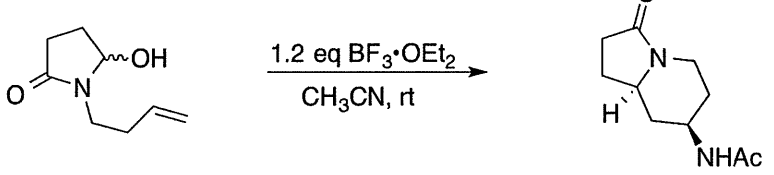

5.

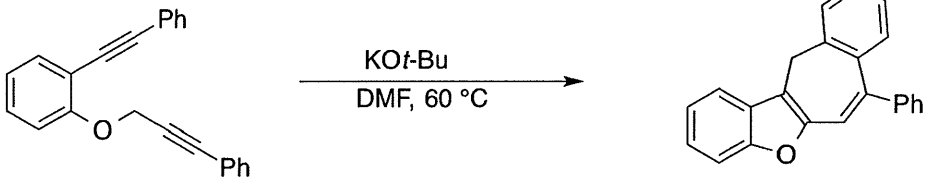

6.

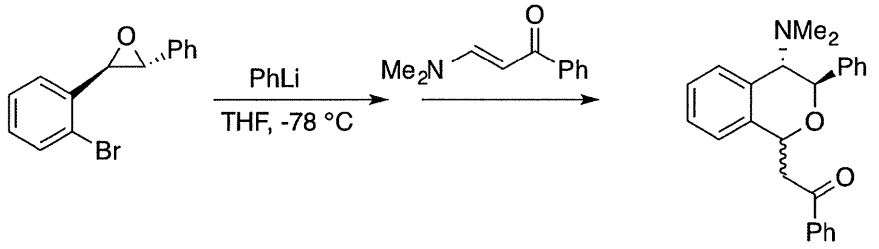

7.

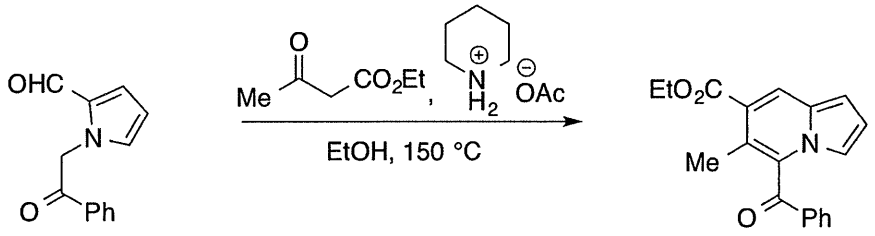

Physical Chemistry Cumulative Exam

1. Suppose the diatomic molecule IBr is excited to a dissociative excited state, first using the potential energy curves shown on the left-hand side of **Figure 1**, which plot the electronic energy E as a function of internuclear separation R in atomic units (1 a.u. of distance = 1 Bohr = 0.529 Å).

(a) If a 400 nm photon is used for the photoexcitation step, estimate the timescale for breaking the chemical bond. State explicitly any assumptions you use in making your estimation.

(b) What is the photodissociation quantum yield for this reaction at this excitation wavelength in the gas phase?

(c) How might the photodissociation quantum yield and timescale for this photodissociation change in solution, and why?

(d) Use your knowledge of general chemistry to argue why the dissociation asymptote has the iodine and bromine atoms both in a ^2P ground electronic state. Explain clearly what the superscript describes and what the 'P' describes about the electronic structure of the atoms.

2. Now consider the actual potential energy curves shown on the right of **Figure 1**.

(a) What effect is responsible for the formation of four different dissociation asymptotes? Explain why the allowed values of J = $^3/_2$ and ½.

(b) Why is it that the energy separation between I($^2P_{3/2}$) and I($^2P_{1/2}$) is larger than the energy separation between Br($^2P_{3/2}$) and Br($^2P_{1/2}$)?

(c) Most of the potential energy curves on the right-hand side diagram have E(R) curves that are smooth functions of R. However, a few curves show odd changes in shape when one potential energy curve with one dissociation asymptote comes into close proximity with a potential energy curve with a different dissociation asymptote. **Figure 2** on the next page shows two curves in this category, extracted from the full set of curves. This is an example of the non-crossing rule, the key elements of which you will now prove.

Label the two states in the absence of coupling, called diabatic states, as |1> and |2>. In the presence of coupling between the two states, the diabatic states will be mixed:

$\Psi_1(R) = c_{11}|1\rangle + c_{12}|2\rangle$ and $\Psi_2(R) = c_{21}|1\rangle + c_{22}|2\rangle$

Starting from $H\Psi = E\Psi$, use this diabatic basis set to show that:

$$\begin{pmatrix} H_{11} - E & H_{12} \\ H_{21} & H_{22} - E \end{pmatrix} \begin{pmatrix} c_{11} & c_{12} \\ c_{21} & c_{22} \end{pmatrix} = 0$$

Solve this matrix equation (or the 2X2 Secular determinant associated with it) to obtain an expression for the energy levels E(R).

(d) What are the conditions on the Hamiltonian matrix elements H_{ij} under which $E_1(R) = E_2(R)$; that is, when the two states cross and therefore are degenerate?

(e) What role can symmetry play in determining when $H_{12} = H_{21} = 0$? Put another way, what happens to H_{12} and H_{21} when the two diabatic states are of the same symmetry? Different symmetry?

(f) What is the effect on the energies of having $H_{12} = H_{21} > 0$? Use your answer to explain why the actual adiabatic states (that is, the states in the presence of coupling) are said to undergo an avoided crossing? What is the splitting between the two states at the value of R for which $H_{11}=H_{22}$?

$h=6.626X10^{-34}$ J·sec $c=3.00X10^{8}$ m/s m(Br) = 79.90 amu m(I)=126.9 amu
1 amu = $1.660X10^{-27}$ kg
Photodissociation quantum yield = $\frac{\#\ molecules\ that\ dissociate}{\#\ photons\ absorbed}$

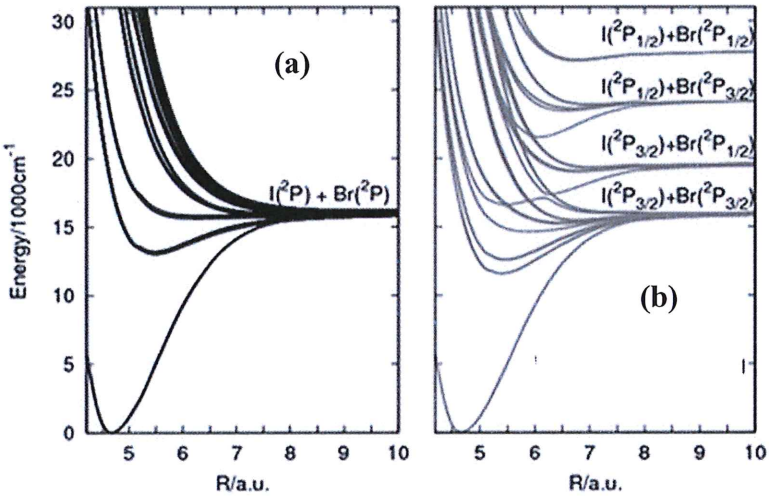

Figure 1: Potential energy curves for IBr.

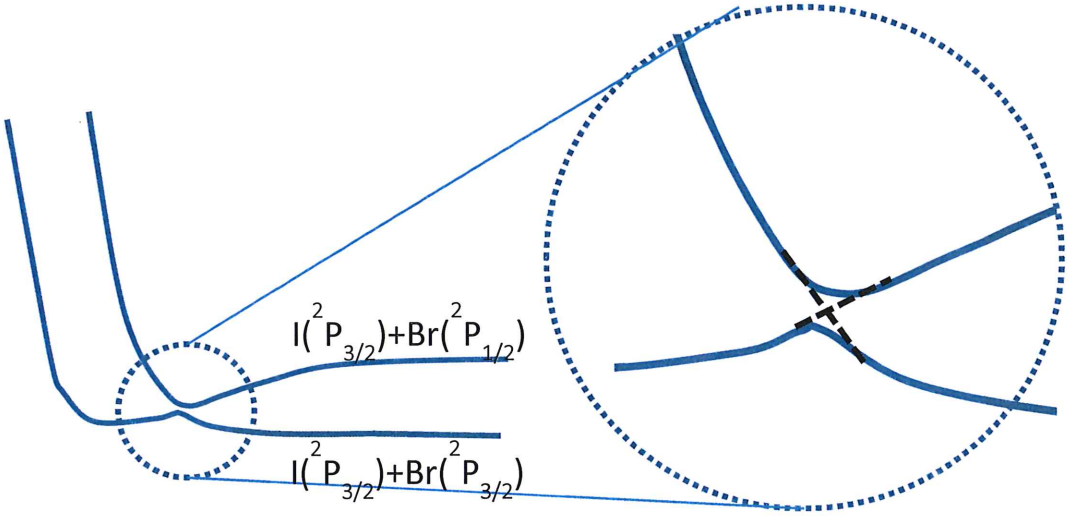

Figure 2: Two potential energy curves selected out of Figure 1(b) that show unusual shapes.

Periodic Classification of the Elements

I A	II A	III B	IV B	V B	VI B	VII B	VIII			I B	II B	III A	IV A	V A	VI A	VII A	O
1 H 1.00797																	2 He 4.0026
3 Li 6.939	4 Be 9.0122											5 B 10.811	6 C 12.01115	7 N 14.0067	8 O 15.9994	9 F 18.9984	10 Ne 20.183
11 Na 22.9898	12 Mg 24.312											13 Al 26.9815	14 Si 28.086	15 P 30.9738	16 S 32.064	17 Cl 35.453	18 Ar 39.948
19 K 39.102	20 Ca 40.08	21 Sc 44.956	22 Ti 47.90	23 V 50.942	24 Cr 51.996	25 Mn 54.9380	26 Fe 55.847	27 Co 58.9332	28 Ni 58.71	29 Cu 63.54	30 Zn 65.37	31 Ga 69.72	32 Ge 72.59	33 As 74.9216	34 Se 78.96	35 Br 79.909	36 Kr 83.80
37 Rb 85.47	38 Sr 87.62	39 Y 88.905	40 Zr 91.22	41 Nb 92.906	42 Mo 95.94	43 Tc (99)	44 Ru 101.07	45 Rh 102.903	46 Pd 106.4	47 Ag 107.870	48 Cd 112.40	49 In 114.82	50 Sn 118.69	51 Sb 121.75	52 Te 127.60	53 I 126.9044	54 Xe 131.30
55 Cs 132.905	56 Ba 137.34	57 La* 138.91	72 Hf 178.49	73 Ta 180.948	74 W 183.85	75 Re 186.2	76 Os 190.2	77 Ir 192.2	78 Pt 195.09	79 Au 196.967	80 Hg 200.59	81 Tl 204.37	82 Pb 207.19	83 Bi 208.980	84 Po (210)	85 At (210)	86 Rn (222)
87 Fr (223)	88 Ra (226)	89 Ac† (227)															

*Lanthanides	58 Ce 140.12	59 Pr 140.907	60 Nd 144.24	61 Pm (147)	62 Sm 150.35	63 Eu 151.96	64 Gd 157.25	65 Tb 158.924	66 Dy 162.50	67 Ho 164.930	68 Er 167.26	69 Tm 168.934	70 Yb 173.04	71 Lu 174.97
†Actinides	90 Th 232.038	91 Pa (231)	92 U 238.03	93 Np (237)	94 Pu (242)	95 Am (243)	96 Cm (247)	97 Bk (247)	98 Cf (249)	99 Es (254)	100 Fm (253)	101 Md (256)	102 No (256)	103 Lw (257)

(Numbers in parentheses are the mass numbers of the most stable isotopes.)